Ultra Wideband Radar Technology and Signal Processing Methods for the Multiphase Flow Monitoring and Tunnel Boring Operations

by

Fatemeh Modares Sabzevari

A thesis submitted in partial fulfillment of the requirements for the degree of Doctor of Philosophy

in

Electromagnetics and Microwaves

Department of Electrical and Computer Engineering

University of Alberta

Abstract

Ultra-wideband (UWB) radar technology can provide solutions for many existing challenges in the industry. In this research, we tackle three existing problems in the oil industry and tunnel construction operations. First, microwave imaging and associated signal processing techniques are proposed for multiphase flow monitoring and metering in oil and gas pipes. A high-resolution image of the pipe cross-section has been generated using UWB synthetic aperture radar (SAR) technique. The image is then used to estimate the area of each phase by identifying and extracting its edges. Individual phase volume is estimated based on the corresponding area and the flow speed. Additionally, a generalized impulsization technique is presented and applied to reconstruct a sharp image and to reduce the error in flow area estimation. Furthermore, a novel technique to enhance the detectability of weak targets is proposed. Finally, a sectional image reconstruction technique is also applied to improve the stratified flow's imaging and metering. All the proposed techniques are evaluated through experiments.

Secondly, the feasibility of applying the UWB radar technology to probe the tunnel face for buried objects or hidden man-made obstacles is investigated. In this study, different buried objects extracted from tunnel construction projects in Edmonton area are considered and characterized by radar techniques. The electrical properties of buried objects, which include the dielectric constant and loss tangent, are measured and compared to the vector network analyzer

dielectric probe measurements. Then, based on its dielectric constant, the buried object is determined. By using a low-power UWB radar, the depth of the buried object from the surface of the tunnel face and its thickness are extracted. In addition, three different pipes containing various fluids are buried in the sand, and the fluids' relative permittivity and loss tangents are estimated. These measurements distinguish the sewer pipes from oil pipes. This study demonstrates the capability of UWB radar technology for acquiring online geological conditions in tunnel construction operations.

Then, with the motivation of automating the future ground-penetrating radars (GPR) or tunnel boring machines (TBM), the reconstructed images of the buried objects are classified into three categories, i.e., boulder, cutter head tooth, and wrench by a deep convolutional neural network. When the model is trained, the effect of the SAR system polarization on the image feature extraction is studied. Moreover, the speed of model training and the classification accuracy across different SAR system polarizations are investigated, and it is shown that the classification accuracy improves by 13.3% due to the inclusive feature of the quad-pol images.

In a real tunnel construction site, large boulders, metal objects, or hidden pipes can hamper the TBM during the excavation operation. In this research, the feasibility of microwave radial imaging by UWB SAR technique is studied through finite difference time domain (FDTD) simulations. In this modeling, a sensor array is placed along the spokes of a wheel that mimics a TBM, and the data is collected at different angles. Then, the image reconstruction process is proposed based on the time domain global back projection. In this study, the effect of the sensor arrangement, the range and cross-range resolution, and the proposed method's effectiveness for imaging the hidden object at the wheel's margin are investigated and presented. These results confirm

the proof of concept and lead us to the next stage of this research.

Lastly, a modified Kirchhoff's migration technique for near-field imaging using the UWB radar transceiver is presented. In the near-field region, the velocity of the pulse propagation is a function of the distance and angle. The proposed technique compensates for this non-uniform propagation velocity. It is shown that the conventional Kirchhoff technique is not successful in focusing the target's image in the near-field; however, the modified Kirchhoff technique results in the focused image of the target with the correct position.

Preface

This thesis is an original work by Fatemeh Modares Sabzevari

Chapter 2 is published as: F. M. Sabzevari, R. S. C. Winter, D. Oloumi and K. Rambabu, "A Microwave Sensing and Imaging Method for Multiphase Flow Metering of Crude Oil Pipes," in IEEE Journal of Selected Topics in Applied Earth Observations and Remote Sensing, vol. 13, pp. 1286-1297, 2020,

Chapter 3 is published as: F. M. Sabzevari, A.E.-C. Tan and K. Rambabu, "Real-time Permittivity Extraction Based on Ultra-Wideband Impulse Radar and Genetic Algorithm for Tunnel Construction Operations", in IEEE Sensors Journal, Accepted, vol. 23, no. 22, pp. 27169-27178, 2023.

Chapter 4 is published as: F. M. Sabzevari, M. Dashti Ardakani, M. Nosrati and K. Rambabu, "Polarization Effect on Feature Extraction and Object Classification by Deep Learning," 2022 IEEE International Symposium on Antennas and Propagation and USNC-URSI Radio Science Meeting (AP-S/URSI), Denver, CO, USA, 2022, pp. 89-90.

Chapter 6 is published as: F. M. Sabzevari, R. S. C. Winter, and K. Rambabu, "A Modified Kirchhoff Migration for Microwave Imaging in Superluminal Propagation Region", submitted to IEEE Transactions on Radar Systems.

To My Beloved Family

For supporting me at every moment and in every way.

Acknowledgements

I would like to express my deepest gratitude to my supervisor, Prof. Rambabu Karumudi, for his support, invaluable guidance, and immense dedication throughout the course of this research. His expertise, constructive feedback, and encouragement have been contributed in shaping this thesis. I am truly fortunate to have had the opportunity to work under his mentorship, and I am immensely thankful for the inspiration he provided.

I extend my heartfelt appreciation to my loving husband, Alireza, for his unwavering support, understanding, and encouragement throughout the challenging yet rewarding process of completing this thesis. His patience and comforting presence have been invaluable. I also would like to express gratitude to my beloved mother, whose unwavering support and encouragement have been the guiding lights throughout this academic journey. Her boundless love, patience, and belief in my abilities have been a constant source of inspiration. Her sacrifices and enduring commitment to my education have shaped me into the person I am today.

I would like to thank my Ph.D. committee members and examiners, Prof. Vien Van, Prof. Mrinal Mandal, Prof. Amina Hussein, and Prof. H. Andy Li for insightful comments and encouragement.

Contents

List of Tables

List of Figures

Chapter 1

Introduction

Ultra wideband (UWB) radar operates by transmitting and receiving a series of electromagnetic (EM) pulses with a relatively large fractional bandwidth, i.e., equal to or greater than 0.20 or an absolute bandwidth equal to or greater than 500 MHz [1], [2]. One of the remarkable advantages of EM pulses is the ability to penetrate into opaque or inaccessible objects and/or media. Typically, UWB radar systems employ short electromagnetic pulses for sensing and imaging applications. Finer range resolution and higher accuracy for imaging and sensing applications require a narrow pulse width. A UWB Gaussian transmitter with a pulse width in the order of 100 ps can achieve a 1.5-cm range resolution in air. Synthetic aperture radar (SAR) creates a large artificial aperture to improve the cross-range resolution [3]. Hence, UWB SAR exploits high-resolution properties in both range and cross-range directions [4].

UWB SAR data acquisition can be approached from either the time domain or frequency domain, each offering distinct benefits and limitations. One of the advantages of UWB SAR data acquisition in the time domain is exceptional range resolution due to its short pulse duration, enabling the differentiation of closely spaced objects. Moreover, UWB signals inherently incorporate range compression, which makes data processing simpler [5]. Additionally, UWB sig-

nals can distinguish various target types based on their unique signatures, enhancing target identification capabilities [6]. One of its disadvantages is added complexity in Doppler processing, particularly for scenarios involving stationary platforms. Doppler processing in SAR is mainly utilized to correct for the Doppler frequency shifts caused by the relative motion between the radar system and the targets on the ground [7]. When the radar system is on a moving platform like an aircraft or satellite, the Doppler information is essential to compensate for the effects of this motion and achieve accurate imagery. However, in scenarios where the platform is stationary or nearly stationary (not moving significantly), the complexity of Doppler processing will be increased because there is little to no motion-induced Doppler shift to correct. On the other hand, UWB SAR data acquisition in the frequency domain is flexible to employ diverse antenna designs and configurations, enhancing adaptability to various imaging scenarios. Furthermore, frequency-domain UWB SAR can extract more accurate Doppler information through coherent processing, enhancing motion compensation and velocity estimation accuracy. Conversely, UWB SAR in the frequency domain has disadvantages, such as diminished range resolution due to longer pulse durations, impacting the ability to resolve closely spaced objects. The frequency-domain UWB SAR data processing is more complex, including separate range compression and Doppler processing, which can be more demanding and time-consuming [8], [9]. In this thesis, we tackled the stationary or quasi-stationary challenges. Hence, we adopted time-domain data acquisition and processing to use the advantage of simple data processing and high-resolution imaging.

1.1 Motivation

UWB radars have attracted attention to be used in different applications [10], such as steam-flow monitoring [11], ice-road monitoring [12], material characterization [13], nondestructive evaluation (NDE) [14], [15], heart-rate estimation [16], biomedical detection and imaging [17], [18], navigation [19], localization, and tracking of targets [20], [21]. For example, in [11], near real-time monitoring of steam-assisted gravity drainage (SAGD) is performed by UWB radar. The UWB system is employed as a buried sensor to monitor oil-sand reservoirs. The collected data is used for steam chamber detection and imaging. The acquired dynamic data can provide feedback to the automated machines and/or field engineers and increase the production rate. Ground-penetrating radars (GPR) are also effective for NDE and material characterization. For instance, [13] exploits the SAR data to extract the complex permittivity map of the target scene. Also, W. B. Muller has developed an automated and reliable technique to retrieve the layer depth, permittivity, and moisture content from 3D GPR array data [22]. The presented data are used for road pavement profiling. The moisture content of the pavement is needed to evaluate the pavement's performance. Furthermore, UWB radar has been proven to provide a high-resolution, relatively cheap, and safe modal to detect and monitor the damaged tissues [23]–[25]. A. T. Mobashsher et al. proposed and investigated a UWB system to detect and localize brain strokes in a realistic 3D human head phantom [23]. In addition, UWB impulse radar is exploited to image the internal tissues of the breast and detect tumors [24]. Moreover, in [26], directional UWB sensors are used for lung tumor detection.

This thesis addresses some of the existing industrial problems in the oil and gas industry and tunnel excavation operations by employing UWB technology.

The UWB SAR technology is adopted for creating high-resolution images from the crude oil pipe, and associated novel signal processing algorithms are presented to estimate each phase flow rate. Secondly, a UWB GPR and the related signal processing are presented as a solution to characterize, image, and classify the object at the tunnel forehead. Finally, Kirchhoff's migration technique is corrected in the near-field of the UWB antenna to improve the image quality acquired by the UWB SAR technique.

1.2 UWB Radar Systems and SAR Processing

This section introduces UWB radar, its applications, and the SAR technique. It also discussed different migration techniques and the advantages and disadvantages of each migration technique.

1.2.1 Radar

Radar, which is short for "Radio Detection and Ranging," is a technology that plays a crucial role in various fields such as aviation, navigation, and military applications. It operates by transmitting electromagnetic signals and then detecting their reflections from targets in the surrounding region. By analyzing the properties of the backscattered signals, radar systems can determine the distance, direction, speed, and even certain characteristics of objects, ranging from aircraft and ships to weather phenomena.

The fundamental principle of radar is based on the propagation of radio waves, which travel at the speed of light. Radar systems consist of a transmitter, i.e., an antenna that radiates EM pulses into space, and a receiver that captures the echoes of these pulses after they bounce off objects. By measuring the time delay between transmission and reception, radar calculates the distance to the target.

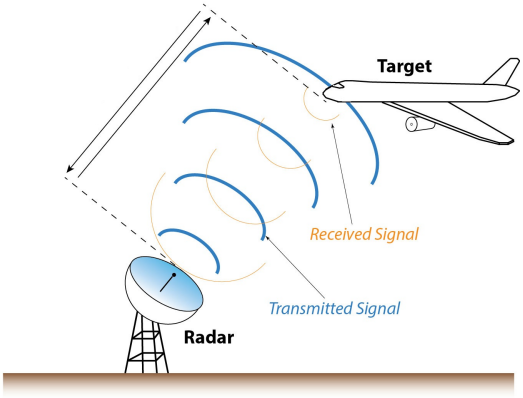

Figure 1.1: Simple radar scenario.

1.2.2 Specifications and Characteristics of UWB Radar

- Pulse Duration: UWB radar pulses have very short durations, often in the picosecond to nanosecond range. This ultra-short pulse duration enables high-range resolution, allowing the radar to distinguish between objects that are close together.

- Frequency Range: UWB radar pulses cover an extensive frequency range, typically from five hundred megahertz to several gigahertz [2]. This broad frequency coverage provides the radar with excellent resolution in the frequency domain, enabling it to detect fine spectral features.

- Range Resolution: The short duration of UWB pulses translates to high range resolution, making UWB radar well-suited for applications requiring accurate distance measurements and the ability to distinguish between objects with small separations.

- Penetration and Obstacle Detection: UWB radar can penetrate various materials, including walls, clothing, and foliage, which makes it suitable for applications such as through-wall sensing, ground-penetrating radar,

and detecting objects hidden under clutter.

- Material Characterization: The wide frequency range of UWB pulses allows for unique material discrimination capabilities. Different materials have distinct frequency-dependent absorption and scattering properties, enabling UWB radar to differentiate between materials based on their responses to the radar pulses [27].

- Low Probability of Intercept (LPI): The low-energy, short-duration pulses of UWB radar result in a low radar cross-section, making it difficult for adversaries to detect and intercept UWB radar signals. This feature is particularly advantageous in military and security applications.

- Resolution in Multiple Domains: UWB radar offers not only high range resolution but also high resolution in other domains, such as time, frequency, and angular resolution. This makes it an adaptable tool for various sensing and imaging tasks.

1.2.3 UWB Radar Transceiver

Every UWB system needs a UWB antenna, a critical component that transmits and receives extremely short-duration pulses across a wide spectrum. Different UWB antennas are developed and designed by researchers, including 3D monopole antennas, 2D monopole antennas, printed slot antennas, printed dipole antennas, and metamaterial antennas [28]. Vivaldi antenna, which is a printed dipole antenna, is a well-known example of a UWB antenna and is capable of operating efficiently across a wide frequency range. Vivaldi antenna features a tapered geometry that allows it to radiate or receive electromagnetic waves over an extended bandwidth. This unique design enables the Vivaldi antenna to achieve excellent impedance matching, low side lobes, and reduced

dispersion, making it well-suited for UWB applications [29]. In this thesis, the Vivaldi antenna is used as the radar transmitter and receiver.

In this research thesis, in all the experiments, the Vivaldi antenna is fed with a DC-free pulse, i.e., monopulse or first derivative Gaussian pulse. Vivaldi antenna has demonstrated a time derivative operation on the input signal. Hence, the propagated pulse is a second derivative Gaussian pulse [30]. An example of a second derivative Gaussian pulse and its frequency component is shown in Fig. 1.2.

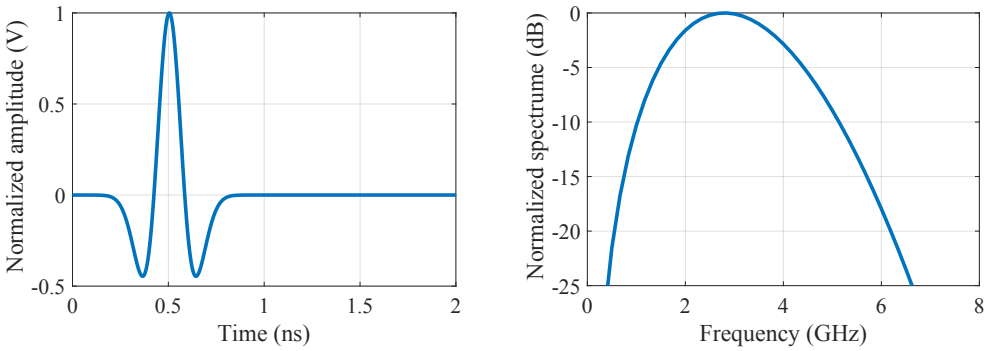

Figure 1.2: a) Second derivative Gaussian pulse. b) Spectrum of the second derivative Gaussian pulse.

1.2.4 Applications of UWB Radar

1) Through-Wall Imaging: UWB radar can be used to image objects and people behind walls, offering potential applications in search and rescue operations such as finding a child in a burning building or locating hostages and their captors by law enforcement officers [31].

2) Ground-Penetrating Radar: UWB radar can detect buried objects, underground utilities, and archaeological features by analyzing how radar waves interact with different subsurface materials [32].

3) Microwave Imaging and Medical Imaging: UWB radar can be employed

for non-invasive imaging of the human body, offering potential applications in medical diagnostics and monitoring [4], [33].

4) Object Detection and Tracking: UWB radar is used for detecting and tracking moving objects, such as vehicles, pedestrians, and wildlife, even in challenging environments [34].

5) Automotive Radar: UWB radar technology is also utilized in advanced driver assistance systems (ADAS) and autonomous vehicles for collision avoidance and object detection [35].

In summary, UWB radar's distinctive features, including its ultra-short pulses and wide frequency coverage, enable it to excel in applications requiring high-resolution imaging, accurate distance measurements, and the ability to distinguish materials. Its versatility and unique capabilities make it a valuable tool across a wide range of fields, from defense and security to medical imaging and automotive technology.

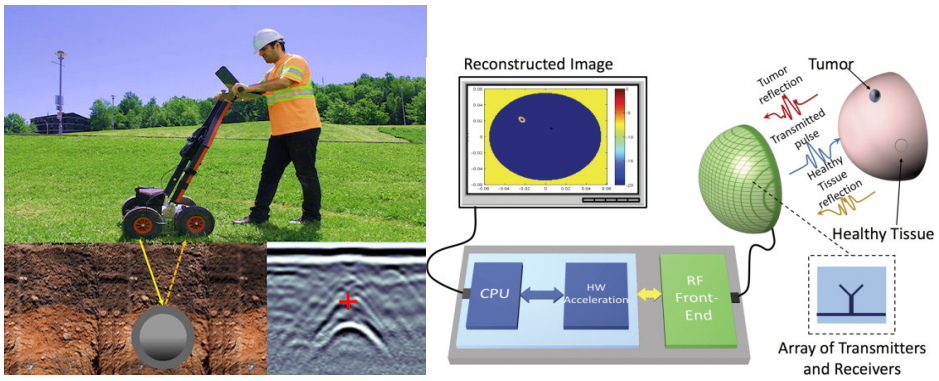

(a) (b)

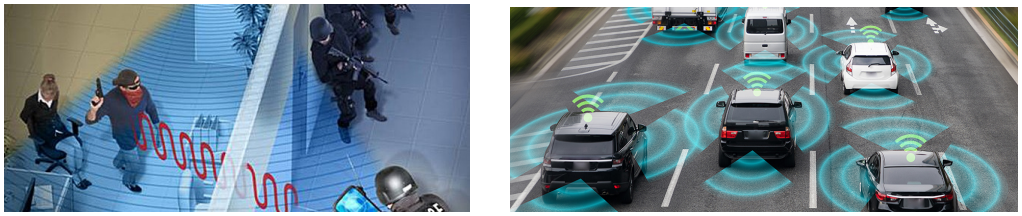

(c) (d)

Figure 1.3: UWB radar applications; a) ground penetrating radar, b) microwave medical imaging, c) through-wall imaging, d) automotive industry.

1.2.5 SAR

Synthetic Aperture Radar (SAR) is a sophisticated remote sensing technology that employs radar signals to create high-resolution images. SAR operates on the principle of coherent radar imaging [36]. It involves transmitting microwave pulses toward the region of interest and then receiving the echoes reflected by objects at different physical locations. These radar echoes are processed to create detailed images, revealing various physical properties of the imaged area. One of the key concepts of SAR is the creation of a synthetic aperture, which effectively extends the physical antenna length using computational techniques.

SAR realization can be performed in Linear SAR (L-SAR) and Circular SAR (C-SAR). In the case of L-SAR, the radar transceiver moves on a line, as illustrated in Fig. 1.4(a). In the case of C-SAR, the radar moves in a circular fashion and collects the back-scattered signal from the image region, as shown in Fig. 1.4(b).

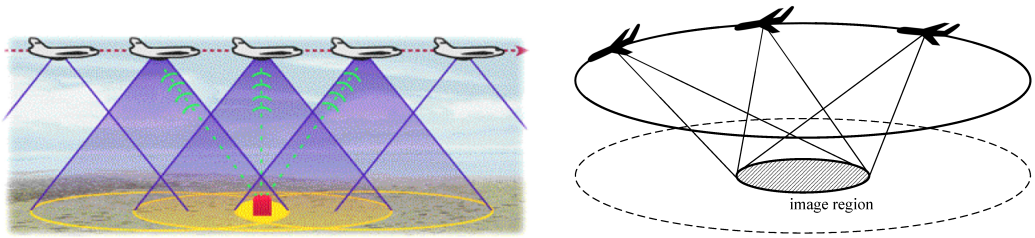

(a) (b)

Figure 1.4: Different SAR configuration, a) Linear SAR. b) Circular SAR.

1.2.6 SAR Migration Techniques

The raw SAR data needs to be processed and converted to the spatial domain to form a focused image of the image region. The process of converting the raw time-space or frequency-space data to a 2D or 3D image is called migration [37].

In SAR processing, migration techniques are crucial for correcting geometric distortions introduced during data acquisition and generating accurate images of the Earth's surface. These techniques are employed to account for factors like the radar platform's motion, topography, and imaging geometry. Here's an introduction to some common migration techniques and comparing their characteristics.

1. Back Projection (BP): Back Projection is a basic SAR imaging technique where radar echoes are directly projected onto an image grid. It's simple and computationally efficient, but it may result in distorted images, especially in the presence of non-linear platform motion and complex region of interest [37].

2. Range Migration Algorithm (RMA): RMA is used to correct range walk effects caused by non-linear radar platform motion. It shifts radar echoes to their proper range positions, improving image accuracy. However, RMA doesn't fully address azimuth scaling effects [38].

3. Omega-k ($\omega - k$) Algorithm: The $\omega - k$ algorithm is effective for spotlight-mode SAR imaging. It transforms data from the time domain to the frequency-wavenumber domain, correcting both range migration and azimuth scaling effects. This technique offers high-resolution images and is suitable for narrow-beam SAR systems.

4. Polar Format Algorithm (PFA): PFA operates in two steps: first, correcting range migration and then azimuth scaling. It transforms raw data to polar coordinates, eliminating azimuth scalloping and simplifying azimuth processing. PFA is advantageous for wide-beam and wide-swath imaging modes.

5. Kirchhoff Migration: The Kirchhoff Migration technique considers the physical properties of the radar system and terrain scattering. It calculates the contributions of radar echoes to each image pixel, leading to improved image quality. Kirchhoff Migration is flexible, but computationally intensive [39].

6. Stolt Migration: Stolt Migration utilizes the Fast Fourier Transform (FFT) to shift data from time to frequency domain. It corrects for both range migration and azimuth scaling effects, yielding geometrically accurate images. Stolt Migration strikes a balance between accuracy and computational efficiency [40].

Comparison of the migration techniques:

- Accuracy: Techniques like Kirchhoff migration, Stolt migration, and $\omega - k$ algorithm offer higher accuracy due to their consideration of system geometry and scattering properties [41].
- Computational Complexity: Back Projection is computationally efficient but might compromise accuracy, while Kirchhoff and Stolt migration require more computation.
- Motion Correction: Techniques like Kirchhoff migration and Stolt migration consider both range migration and azimuth scaling effects, providing a comprehensive correction.
- Image Quality: Kirchhoff migration and Stolt migration often produce higher-quality images, but the choice depends on trade-offs between accuracy and processing time.

In summary, the choice of migration technique depends on factors like imaging mode, system complexity, desired image accuracy, and computational resources available. Different techniques offer varying levels of accuracy, efficiency, and applicability, providing different SAR processing requirements [42].

1.3 The Contributions of this Thesis

In this research study, we addressed some of the industry's existing challenges and proposed UWB radar solutions. First, the monitoring and metering of the multiphase flows in the oil industry are addressed [43]. Real-time multiphase flow metering (MFM) is recognized as one of the best methods for optimizing field operations in oil and gas fields. The cost of MFM in 2009 was estimated to be in the range of hundreds of thousands of dollars [4]. Hence, there is a significant demand from the oil and gas industry for a reliable and inexpensive technique for MFM. The existing MFM techniques are either destructive, pricey, or computationally expensive. In this research thesis, UWB Circular SAR is adopted to monitor, and post-processing techniques are presented and applied for metering each phase flow rate.

Secondly, we investigated the existing challenge of tunnel boring (TB) operations. In many TB excavations, the TBMs may face unexpected geological ground conditions or ram into unknown man-made obstructions, such as existing pipes or piles with inaccurate as-built information, boulders, abandoned metallic objects, or any hidden objects with archaeological or paleontological value. Tunneling engineers rely on either excavating a limited quantity of vertical boreholes during site investigation or taking core samples at the tunnel face to acquire geotechnical data and probe for obstacles. This process is time-consuming and expensive. It also fails to provide accurate and timely information that is needed to detect the boulders or man-made obstructions lying immediately ahead of the tunnel face. UWB radar techniques are exploited to analyze the geological conditions present in the tunnel face using material characterization. The buried object's material is determined by comparing the measured dielectric constant with the priory-developed material

electrical properties catalog.

In chapter four, a convolutional neural network is designed to classify three types of objects from reconstructed images acquired by the UWB-GPR. Both single-polarized and quad-polarized SAR systems are widely used in many applications. Three categories of buried objects are classified, including asymmetrical objects. All the reconstructed images have shown different features resulting from single-pole and quad-pole SAR data. The study investigated how the choice between single-pole and quad-pole SAR influences feature extraction, model training speed, and classification accuracy. Furthermore, it was observed that the model's training is faster when both training and test images belong to the same polarization groups. Additionally, a higher prediction accuracy is achieved when both training and test datasets share the same polarization characteristics. This investigation highlights that for accurate classification of quad-pole SAR images, it is essential to train the model using quad-pole SAR data rather than relying on single-pole SAR images.

Moreover, chapter five presents an exploration of UWB GPR for the detection and analysis of small practical objects located at the tunnel face. Various sensor arrangements, including equally and non-equally spaced sensors, are investigated. The analysis focuses on achievable range and cross-range resolutions, demonstrating the potential to achieve a range resolution of 1.74 cm and a cross-range resolution of 4.6 cm using a pulse width of 282 ps. Furthermore, the study extends to a more complex scenario involving four distinct small objects: two boulders, a metal nail, and a water patch. By employing Finite-Difference Time-Domain (FDTD) simulations and SAR processing, accurate 3D images are reconstructed. These images capture the precise positions and

dimensions of the objects. This proof of concept suggests that UWB sensors can be integrated into the tunnel boring machine and automate the process of acquiring geological conditions of the tunnel face in real-time.

In Chapter Six, a novel Kirchhoff's migration technique is proposed, simulated, and experimentally validated within the near-field region of the antenna. The conventional Kirchhoff's migration assumes a uniform propagation velocity in the far-field region of the radar transceiver, i.e., antenna. In the near-field region of the antenna, the pulse propagates at a significantly greater speed compared to the far-field region. The propagation speed can vary as a function of the distance and angle in a non-linear manner. This non-linearity causes non-focused images. In chapter six, a modified Kirchhoff's migration method is proposed to take into account the non-uniformity of the propagation speed. It is shown that the proposed method results in focused images in the near-field region.

Chapter 2

Crude Oil Flow Monitoring and Imaging

2.1 Introduction

Real-time, accurate, and non-destructive flow monitoring and measuring multiphase flows are widely needed in many industries, such as food, aerospace, geothermal, and oil and gas industries [44]–[46]. As mentioned earlier, real-time multiphase flow metering (MFM) is recognized as one of the best methods for optimizing field operations in oil and gas fields. The cost of MFM in 2009 was estimated to be in the range of hundreds of thousands of dollars [47]. Hence, there is a large demand from the oil and gas industry for a reliable and inexpensive technique for MFM.

The most popular available techniques for MFM can be categorized into seven classes based on their technology: conventional method or separation [48], impedance techniques [49], Radio Frequency (RF) sensor [50], resonant cavity sensors [51], [52], gamma-ray [53], x-ray [54], and Coriolis-microwave flow meter [55].

However, none of the aforementioned techniques are appealing enough to be widely used in the industry. The conventional method is invasive and expensive [48]. Impedance techniques, which include electrical capacitance tomogra-

phy (ECT), electrical resistance tomography (ERT), and magnetic induction tomography (MIT), need to identify the flow pattern before measurements. The low image quality makes it more complicated to distinguish different phases [56]. The accuracy of the RF sensor technique is dependent on the water percentage, and a look-up table is required [50]. The resonant cavity method cannot be used in situations with continually flowing fluids [51]. Gamma-ray and x-ray methods are costly to implement and not very popular due to safety aspects [50]. The combined microwave and Coriolis technique is bulky and hard to install [55].

In this chapter, a non-invasive microwave sensing and imaging (MSI) method based on UWB SAR imaging is presented for MFM in crude oil pipelines. UWB SAR imaging provides a high-resolution and low-cost solution for the imaging of different components (phases) in a multiphase flow. Then, by applying an edge detection algorithm, the reconstructed image is used to find different phases. Finally, each phase flow rate is estimated based on its area and the flow speed. Moreover, to increase the accuracy of the flow rate estimation, a generalized impulsization technique and a novel weak scatterer enhancement technique are presented. Both techniques are then validated through simulation and experimental measurements. Also, the sectional image reconstruction for stratified flows is proposed to improve the image accuracy and flow rate estimation.

2.1.1 Problem Statement

In general, the flow in a crude oil pipe is a mixture of three main components (phases): water, oil, and gas [see Fig. 2.1(a)]. Petroleum operators need to monitor and measure the volume or flow rate of each phase before making

Table 2.1: Comparison table for the existing multiphase flow measurement.

Reference	Technology	Frequency	Complexity	Error Criteria	Error	Flow Monitoring	Cost	Limitations
[50]	RF Sensor	250 Hz	low	permittivity	30	No	low	non-metallic pipe
[53]	Gamma-ray	order 10^{19} Hz	high	root mean square error (RMSEP)	39	No	very high	safety aspects, limited to high water concentration
[57]	ECT/ERT Dual modality	200 kHz (for ECT)	high	-	-	Yes	high	oil continues flow needed for ECT, flow phase dependent
[58]	Resonant Cavity Sensor	100-350 Hz	high	-	-	No	high	only used for limited fraction of water, sensitive to water
[59]	CT and Cross-Entropy	order 10^{19} Hz	high	Relative Error (RE)	10	Yes	high	safety aspects, non-metallic pipe
[60]	X-Ray	order 10^{16} Hz	very high	-	-	No	very high	health risks, low accuracy
Proposed	UWB	2-10 GHz	low	Crude Flow Error	3.8	Yes	low	non-metallic pipe

decisions for possible further processing [47]. Since the final goal of MFM is the flow metering of each phase, the flow rate error is considered as the metric in this study. A detailed explanation of the flow rate and flow rate error calculation is presented in the next section.

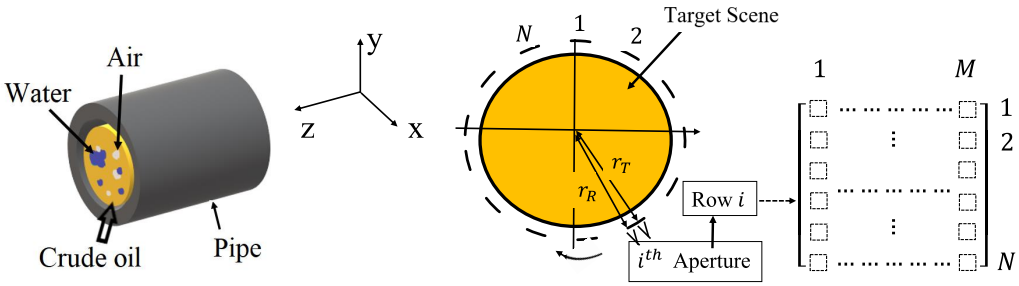

(a) (b)

Figure 2.1: a) General crude oil pipe. b) CSAR data acquisition.

This chapter uses MSI technology to create a 2D image of any arbitrary pipe cross-section. The image is then used to estimate the area of each component i.e., phase in a specific cross-section, $S(z)$, where z is used to differentiate between different cross-sections. It is assumed that for a small-enough Δz: $S(z_1) \simeq S(z_1 + \Delta z)$, which implies the cross-sectional area of each component (phase) is constant over Δz. Hence, the total volume of each component can be represented as:

$$V = S(z)\Delta z. \tag{2.1}$$

Consequently, the flow rate Q of each component or phase can be calculated as:

$$Q = \frac{V}{\Delta t} = \frac{S(z)\Delta z}{\Delta t} = S(z) \times \bar{v}, \tag{2.2}$$

where $\bar{v}$ is the average velocity of the flow, which can be extracted using Doppler techniques [61]. Therefore, estimating $S(z)$ leads to flow metering for

each component or phase. Then, the flow rate error of each flow component or phase is calculated using the following formula:

$$err = |\frac{Q_{cal} - Q_{true}}{Q_{true}}| \times 100 \tag{2.3}$$

where Q_{cal} and Q_{true} are the estimated flow rate and the true flow rate, respectively. It should be noted that the maximum average velocity of a multiphase flow in industrial oil-gas pipes is reported at 50 km/h or 13.8 meters per second [62]. Since data acquisition of the proposed method is completed in 10 ms, the target scene can be modeled as a stationary problem in each cross-section of the pipe.

2.2 Individual Phase Flow Velocity

In the context of the crude oil industry, multi-phase flow involves the simultaneous movement of various phases, including crude oil, water, and natural gas. Typical velocity ranges for these phases can vary based on factors like fluid properties, well design, and operational conditions. Crude oil velocities in pipelines typically span from 0.5 to 3 meters per second (1.6 to 9.8 feet per second), while water velocities tend to range from around 0.2 to 1.5 meters per second (0.7 to 4.9 feet per second). Natural gas, with its lower density, exhibits velocities ranging from 10 to 30 meters per second (32.8 to 98.4 feet per second). These approximations serve as general guidelines for understanding the behavior of multi-phase flow, but actual velocities can deviate due to factors unique to each production scenario [63]. However, in some scenarios, such as balanced multiphase flow in a Well-Managed Reservoir, the velocity of the oil and water can be approximately equal. In some well-managed oil reservoirs, the production rates of oil, water, and gas are carefully controlled. The reservoir has been optimized to have a stable balance between the phases, and

the production rates have been adjusted to minimize any phase separation or stratification. In this scenario, the average velocities of the individual phases might be relatively close because the flow rates are balanced. The crude oil might be flowing at an average velocity of around 1.5 meters per second, the water at 1 meter per second, and the natural gas at 15 meters per second [64].

Please note that in the case where the individual phase velocity is different, Equation 2.2 can be re-written as:

$$Q_i = \frac{V_i}{\Delta t} = \frac{S_i(z)\Delta z}{\Delta t_i} = S_i(z) \times \bar{v}_i, \tag{2.4}$$

where $\bar{v}_i$ is the average velocity of the individual phase, i.e., crude oil, water, and natural gas. However, measuring the individual phase velocity will add complexities to the proposed UWB SAR technique; it can be measured by ultrasonic techniques [65], [66]. In other words, all the following calculation for measuring individual phase flow rates is valid, i.e., Q_i; however, an additional step for measuring the $\bar{v}_i$ is required.

2.3 System Configuration

A complete experimental setup of microwave sensing and imaging system for MFM is illustrated in Fig. 2.2. It consists of N sensors arranged in a circular fashion around the pipe. Each sensor includes two antennas: one is for transmitting and the other for receiving the reflected pulse from the multi-phase fluid. The pulse generator generates a UWB pulse, and it connects to an RF switch box, which in turn, connects to the transmitter and receiver of the active sensor. In other words, $N - 1$ sensors are inactive, and only one sensor is active at a time. The received signals from the sensors are processed to reconstruct the image and estimate the flow rate. The following section provides more details about circular SAR (CSAR) microwave imaging.

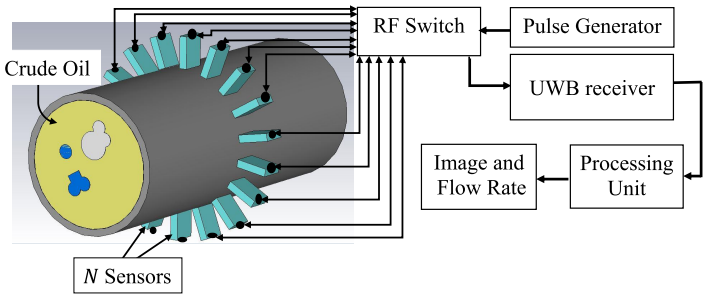

Figure 2.2: System setup.

2.3.1 Data Acquisition and Image Reconstruction

A basic schematic of CSAR is shown in Fig. 2.1(b). As can be seen, N apertures are used for collecting data. At aperture position i, the transmitted and the backscattered signal can be written as:

$$s_{T,i} = s(t) \tag{2.5}$$

$$s_{R,i} = As'(t - \Delta t), \tag{2.6}$$

where A, $s'(t)$, and Δt are the amplitude of the received signal, the time derivative of $s(t)$, and the round trip time of the pulse between the antenna and a scatterer, respectively [67]. Hence, the raw data will be in a matrix format with dimensions $N \times M$, where N and M are the number of apertures and the number of sampled points of the received pulse, respectively. In this study, the transmitted signal is a second derivative Gaussian pulse, which can be written as[68]:

$$s_{T,i} = \frac{2}{\tau^2} exp\left(-(\frac{t}{\tau})^2\right)\left(\frac{2t^2}{\tau^2} - 1\right) \tag{2.7}$$

where $s_{T,i}$ and τ are the second derivative Gaussian pulse and the time constant, respectively. The range resolution and the cross-range resolution of CSAR are the same and are estimated as [4]:

$$\Delta_R = \frac{c}{3BW\sqrt{\varepsilon_r}} \tag{2.8}$$

where c, BW, and ε_r are the speed of light in a vacuum, pulse bandwidth, and dielectric constant of the propagation medium, respectively. In order to remove the mutual coupling between the transmitter and the receiver, as well as ambient effects, a calibration process is needed. In this study, the calibrated signal is calculated as follows:

$$s_{c,i} = s_{raw,i} - s_{am,i}, \qquad i = 1, 2, ..., N \tag{2.9}$$

where $s_{c,i}$, $s_{raw,i}$, and $s_{am,i}$ are the calibrated signal, the raw signal, and the ambient signal in the presence of all other sensors for the aperture position i, respectively.

Then, the calibrated signals, medium electrical properties, along with the aperture locations are fed to the time-domain global back-projection (TD-GBP) technique [69] and 2D images are reconstructed, i.e., $f(x, y)$. It is important to highlight that image pixels are real numbers. Different image formats are proposed to evaluate different dielectric interfaces and sharpen the boundaries of the target in the image by eliminating the side lobe effects of the received pulse [70]. The positive image and absolute image are defined in [4], [70] as:

$$Absolute\ Image = \big\| f(x, y) \big\| \tag{2.10}$$

$$Positive\ Image = real\big\{ f(x, y) \big\} + \big\| f(x, y) \big\| \tag{2.11}$$

2.3.2 Imaging and Flow Metering

Different flow patterns in oil pipes have been reported, including dispersed bubble flow, stratified, slug, and annular flow [71]. In this study, the first two types of flows are considered. The following sections describe the imaging techniques for both cases.

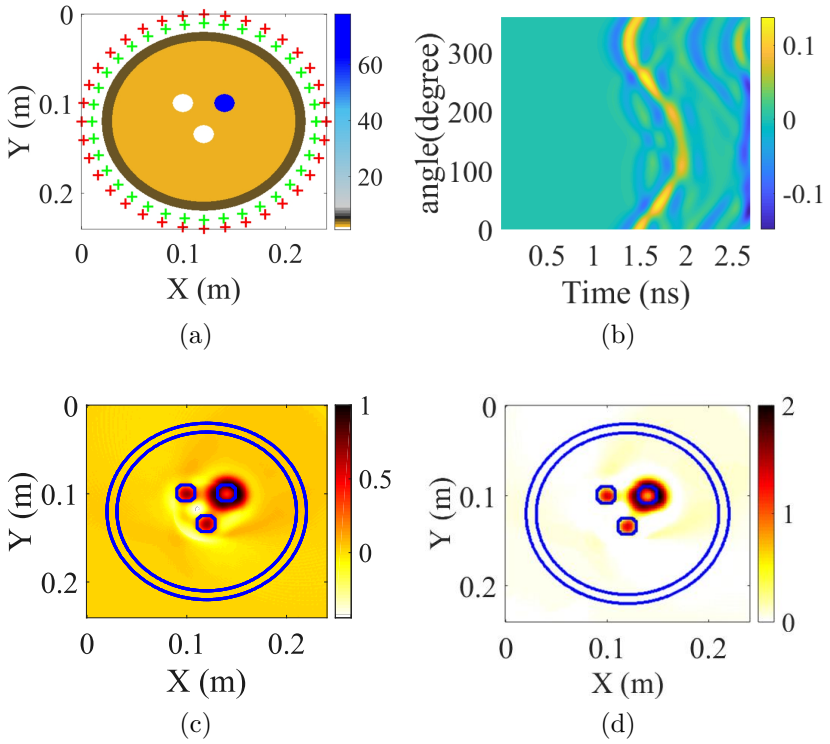

Figure 2.3: a) Simulation setup. b) Calibrated data. c) Real image. d) Positive image.

Dispersed Bubble Flow

In this section, several dispersed bubble flow scenarios are investigated. A three-phase scenario, which includes a water bubble and two air bubbles in crude oil, as shown in Fig. 2.3(a), is simulated using a 2D Finite Difference Time Domain (FDTD) solver. The dielectric constants of water, air, and crude oil are considered to be: 78, 1, and 2.1, respectively. Note that all materials are considered non-dispersive due to small dielectric constant variations within the radar frequency. Since the bubble size is in the range of 3 to 23 mm [72], all three bubbles are considered as circles with a radius of 10 mm. The most frequently used pipes are made of glass-reinforced plastic, also known as fiber-glass composites; and the diameter is reported as 10.2 cm [73]. The dielectric constant of the fiberglass composites is in the range of 3.45 to 4.42 [74]. There-

fore, the considered pipe has a dielectric constant of 4, and an inner radius of 9 cm with a thickness of 1 cm. In Fig. 2.3(a), the transmitters and receivers are shown as red and green '+' symbols, respectively. The transmitted signal is a second derivative Gaussian pulse with a full width at half maximum (FWHM) of 100 ps, which corresponds to a -10 dB bandwidth of 4.12 GHz.

The calibrated data, the reconstructed real, positive, and absolute images are shown in Fig. 2.3. Note that the solid blue lines correspond to the pipe and the air and water targets. The reconstructed images clearly show air and water bubbles. However, the final goal of MFM is an automatic measurement of the area or flow rate of each phase in the pipe. One possible solution is to detect edges in the reconstructed image, distinguish each phase boundary, and then estimate the flow rate of each phase. The next section provides more details about edge detection algorithms.

Edge Detection Algorithms for MFM

Generally, edge detector algorithms apply a first or second-order spatial derivative to the image and find the local maxima or zero-crossing points [75]. A wide range of edge detectors is presented and studied in [76]. Four of the most popular edge detectors are Canny, Sobel, Prewitt, and Roberts. Canny edge detection is based on three objectives: 1) low error rate, 2) thin edges, and 3) accurate localization [77]. The Sobel edge detector performs a second derivative of the image luminance to extract the edges [78]. Prewitt and Roberts are two other gradient-edge detectors that use Prewitt and Roberts' operators, respectively. For the case of MFM, the edge detection algorithm with the least error should be applied. To study the quality of edge detector algorithms, the four edge detectors are applied to the real image, shown in Fig. 2.3(d), and results are shown in Fig. 2.4. In all four cases, the true edges are shown in solid black lines, and the detected edges are marked with yellow lines. As can be

seen, the Sobel and Prewitt detectors perform poorly and fail to successfully detect the continuous edge of the water target. The Robert operator output provides jagged edges. The evidence suggests that the Canny edge detector might be the best candidate for this application. The local maximum in spatial domain variation is considered as edges, and the maximum variation of the pixels values in the real image and the positive image are equal; hence, the edge detection can be applied to either the real image or the positive image. The functionality of the edge detectors can be controlled by a threshold [79]. The edge detector threshold should be adjusted based on several factors, such as the noise level and number of pixels [80]. The Canny edge detection is performed with four different thresholds, and the results are shown in Fig. 2.5. The large black circles are the true pipe edges and the small black circles are the true bubbles' edges. As can be seen, a zero threshold results in the detection of unnecessary edges. On the other hand, a 0.9 threshold fails to detect one of the target edges. While thresholds 0.3 and 0.6 are both successful at detecting all three targets' edges, the 0.6 threshold is the best threshold for this case. It should be emphasized that the targets' image brightness and the reconstructed images' special gradient are structure-dependent. Hence, a fixed threshold value cannot be recommended. A suitable threshold might be considered to be one in the range of 0.3 to 0.6. In a real-case scenario, the threshold adjustment requires prior information that can be attained by properly training the operators.

The flow rate error of each phase is calculated based on Fig. 2.5(d) and presented in Table 2.2. Air bubbles and the water bubble generate more errors than crude oil in flow rate estimation. The area of the water and air bubbles is small compared to that of the crude oil; therefore, a small deviation from the true value of the area causes a large error compared to the crude oil.

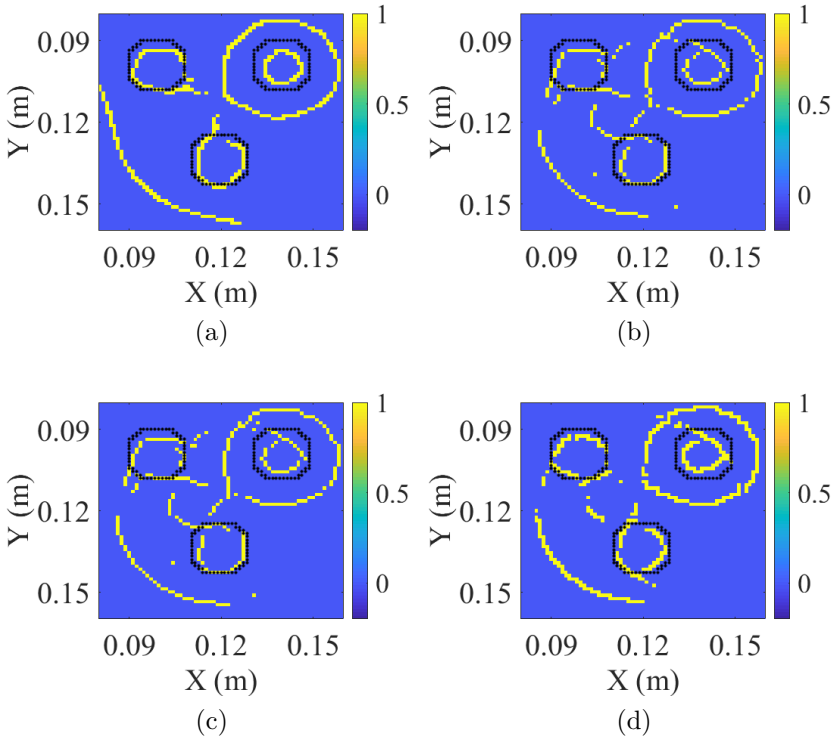

Figure 2.4: a) Canny edge detector. b) Sobel edge detector. c) Prewitt edge detector. d) Roberts edge detector.

Impulsization

The ideal pulse for MSI is a Dirac delta function since this would have infinite range resolution. The pulse generator used in this experiment generates pulses with FWHM in the range of 80 *ps* to 100 *ps*. The impulsization technique is a surrogate post-processing method to generate a definite image with sharp edges. A mathematical representation of this method [81], can be formulated

Table 2.2: Phase error of the simulated dispersed bubble flow .

Target(phase)	**Phase area error** (%)
Air 1	16.1
Air 2	19.3
Water	43.9
Crude oil	2.1

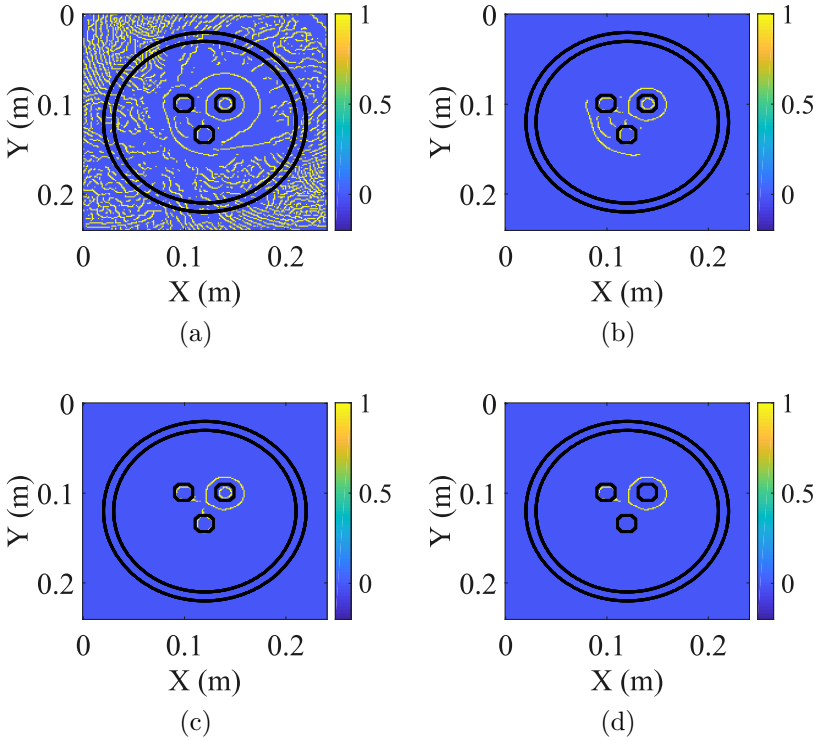

Figure 2.5: Canny edge image; a) threshold =0, b) threshold =0.3, c) threshold =0.6, d) threshold =0.9.

Table 2.3: Phase error of the simulated two-phase flow.

Target (Phase)	**Phase area error (%) (conventional technique)**	**Phae area error (%) (impulsization technique)**
Water	28.1	14.9
Oil	2.6	1.4

as:

$$\delta\Big(s_{c,i}(t)\Big)=\begin{cases} s_{c,i}(t_{peak}) & \text{if } t=t_{peak} \\ & \ \ \& \ \ s_{c,i}(t_{peak})>T \\ 0 & \text{otherwise} \end{cases} \tag{2.12}$$

where t_{peak} and T are the time at which the $s_{c,i}$ has a peak and a threshold for picking max values, respectively. The t_{peak} can be easily determined by finding the peaks of $s_{c,i}$. The idea of impulsization can be generalized by the following formula:

$$\delta_g\Big(s_{c,i}(t)\Big)=\begin{cases} s_{c,i}(t) & \text{if } |t-t_{peak}|<\Delta T \\ & \ \ \& \ \ s_{c,i}(t_{peak})>T \\ 0 & \text{otherwise} \end{cases} \tag{2.13}$$

where δ_g and ΔT are a generalized impulsized signal and the specified time window, respectively. The choice of ΔT depends on the pulse width and the level of noise. As shown in Fig. 2.4, the edge detection algorithms find two different circles which correspond to the side lobes of the received pulse. In order to enhance the accuracy of the edges, the generalized impulsization technique has been used. Fig. 2.6(a) shows a scenario with an arbitrary non-smooth water bubble. Figs. 2.6(b) and 2.6(f) show the calibrated data and the corresponding edge image, respectively. The Equation (2.13) with a $\Delta T = 29.7$ ps, which is 20 time steps, is applied to the calibrated data and the positive image is shown in Fig. 2.6(e). As ΔT decreases, the generalized impulsization method will be equivalent to transmitting a Dirac delta signal, i.e., $s(t) = \delta(t)$. However, this technique does not increase the spatial resolution and only results in a non-blurred image, which is a perfect input for the edge detection algorithm. Fig. 2.6(g) shows the edge image after applying generalized impulsization. The two inner and outer yellow lines in Fig. 2.6(f), caused by the pulse width, are merged in Fig. 2.6(g). There are some extra lines in Fig. 2.6(g). These lines are the drawback of the impulsization technique. The flow rate error of each phase is calculated and presented in Table 3.3. The water flow rate error and oil flow rate error are improved to 14.9% and 1.4%, respectively.

Weak Scaterrer Enhancement

MSI technology is based on the discontinuities in the permittivity of the materials. The magnitude of the received signal is proportional to the contrast of the target compared to the background. Hence, the reflected signal from the high-contrast targets carries far more energy than the corresponding signal from the low-contrast ones. To illustrate this phenomenon, a three-phase scenario, as shown in Fig. 2.7(a), is simulated in the FDTD solver. In Fig.

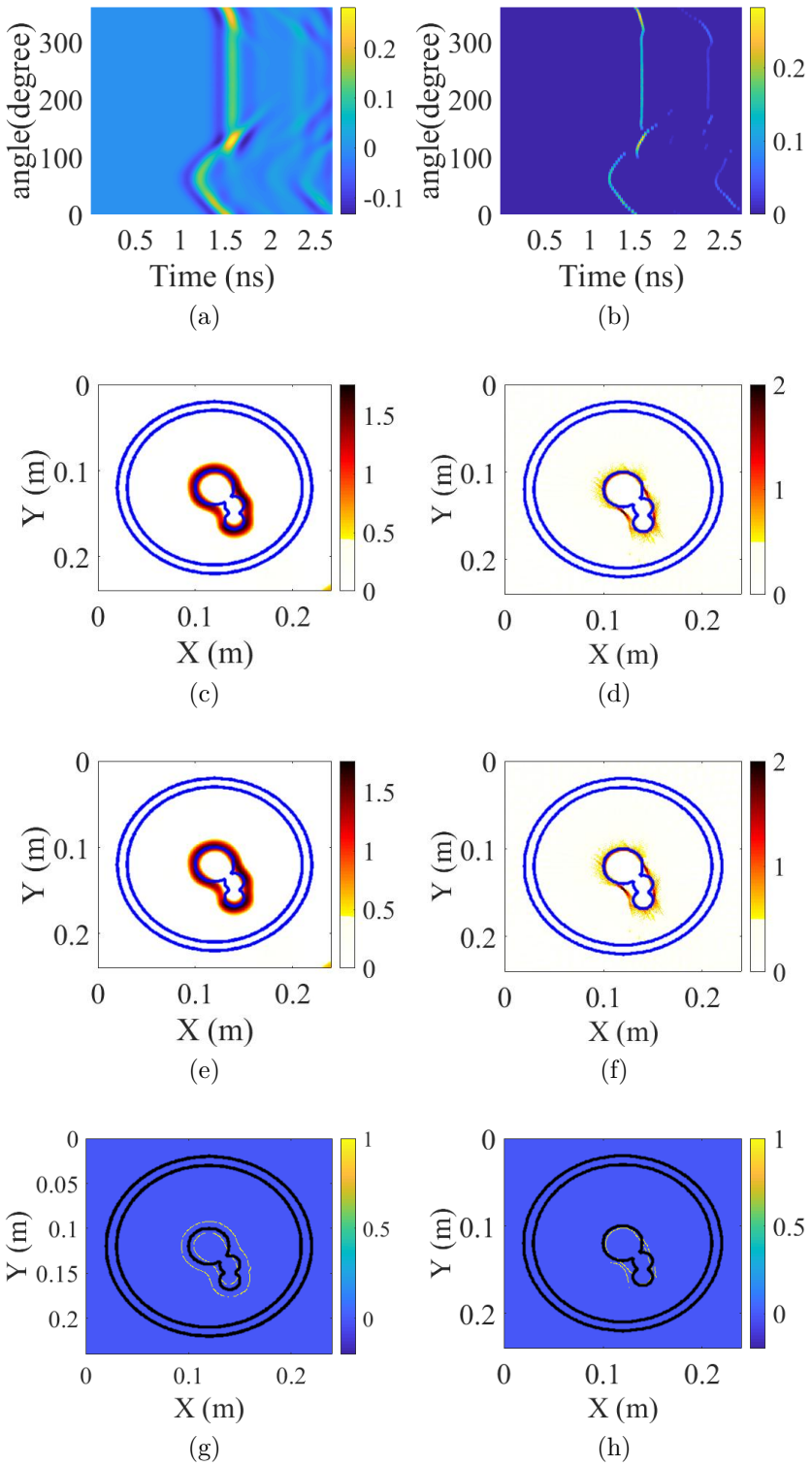

Figure 2.6: a) Simulation setup. b) Calibrated data. c) Calibrated data applying generalized impulsization. d) Positive image. e) Positive image. f) Edge image applying generalized impulsization. g) Edge image applying generalized impulsization.

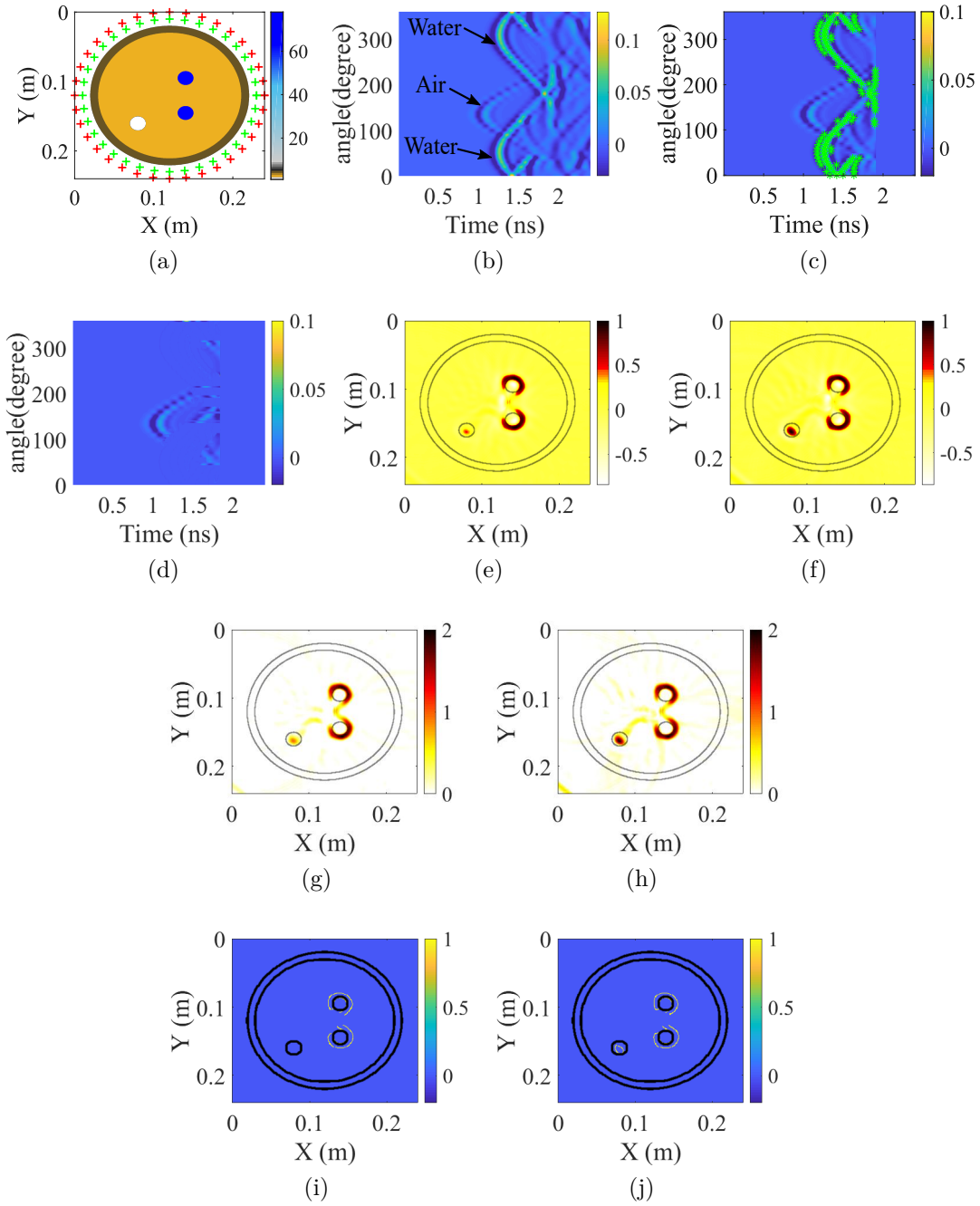

Figure 2.7: a) Simulation setup. b) Calibrated data. c) Peaks with a value greater than the threshold. d) Modified calibrated data. e) Conventional real image. f) Real image applying weak scatterer enhancement. g) Conventional positive image. h) Positive image applying weak scatterer enhancement. i) Conventional edge image. j) Edge image applying weak scatterer enhancement.

Algorithm 1 Proposed weak scatterer enhancement

s_c, W: inputs, $Total\ Image$: output W: Pulse width

$Image1 \leftarrow s_c$, Image reconstruction using TD-GBP

for $i = 1, ..., N$ do

find the peaks of the $s_{c,i}$ k: Number of peaks

for $j = 1, ..., k$ do

if $s_{c,i}(t_{peak}) > H_p$ then: H_P: Threshold

$$`s_{cm,i}(t) = \begin{cases} 0 & \text{if } |t - t_{peak}| < W/2 \\ s_{c,i}(t) & \text{otherwise,} \end{cases} \tag{2.14}$$

$s_{cm,i}$: modified calibrated signal

$Image2 \leftarrow s_{cm}$, Image reconstruction using TD-GBP

$Total\ Image = Image1 + Image2$

2.7(b), the magnitude of the air sinogram is approximately three times weaker than that of the water sinogram. This causes a pale appearance in the reconstructed image, as shown in Figs. 2.7(e) and 2.7(g). When MSI is used in a practical application, the reconstructed image will be drastically affected due to the presence of noise and clutter [82]. A flowchart of the proposed novel weak scaterrer sinogram enhancement algorithm is shown in Fig. 2.8. The algorithm takes s_c and W, the calibrated signal and the pulse width, as inputs. The peaks of the calibrated signal for the aperture position i are found, and their corresponding pulse segment is set to zero if $s_{c,i}(t_{peak})$ is greater than a threshold (H_p). This process repeats for all aperture positions, and the modified calibrated signal is then forwarded to the image reconstruction process. The steps of implementing the technique are presented in algorithm 1. 1.

Consider Fig. 2.9 for understanding steps 5-7. The blue curve is the $s_{c,i}$, i.e., $i = 10$. The red line is the threshold line, and the detected peaks are marked with a circle. The green peaks are greater than the threshold. Step (5) removes the full pulse that corresponds to the green labeled peaks. Finally, the $s_{cm,i}$ is shown with a black line. It should be noted that the threshold is constant for all the aperture positions. One possible choice of threshold is to scale it with

Table 2.4: Phase error of simulated three-phase flow.

Target (Phase)	**Phase area error (%) (conventional technique)**	**Phase area error (%) WSE technique)**
Water1	15.9	15.3
Water2	19.1	13.6
Air	100.0	60.0
Oil	0.9	0.4

respect to the maximum value of $|s_c|$. Typically, H_p should be small enough to completely eliminate the strong reflection. On the other hand, H_p should be high enough to preserve the weak reflection. The best choice of H_p for the crude oil pipes is in the range of $H_p = [0.3 \times max\{|s_c|\} - 0.45 \times max\{|s_c|\}$. The reconstructed image using s_{cm} only consists of weak scatterer targets. In order to present a complete image, which includes all of the targets, the image of the modified calibrated data is added to the original image. This novel method is applied to the time-gated calibrated data, which is shown in Fig. 2.7(b). The threshold has been chosen: $H_p = 0.31 \times max\{|s_c|\}$. The green marked labels on Fig. 2.7(c) show the peaks that are greater than H_p. It is evident that the algorithm removes the reflections corresponding to the water bubbles. The signature of water bubbles mostly vanished in the calibrated data, but the air bubbles' signature is left, as illustrated in Fig. 2.7(d). Conventional real and positive are shown in Figs. 2.7(e) and 2.7(g), respectively. The canny edge detector is applied to the positive image and the edge image is illustrated in Fig. 2.7(i). The air bubble appears as a pale target, and it has not been found by the edge detector. In Fig. 2.7(f), the air bubble is roughly as clear as water bubbles. The Canny edge detector is applied to the enhanced positive image, and the air bubble appears in the edge image, as shown in Fig. 2.7(j). The flow rate errors for all targets and crude oil are calculated and presented in Table 2.4. The flow rate error of the crude oil is improved to 0.4%.

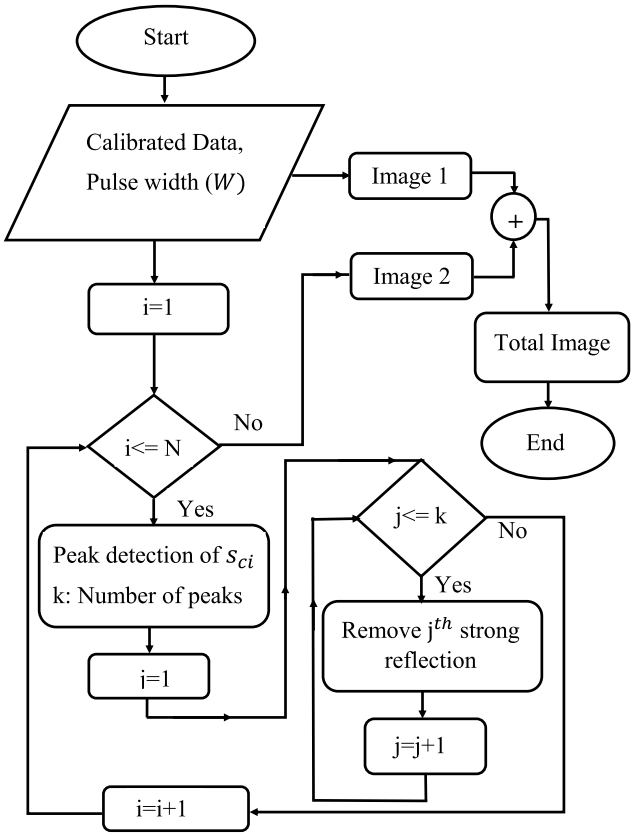

Figure 2.8: Weak scatterer enhancement flowchart.

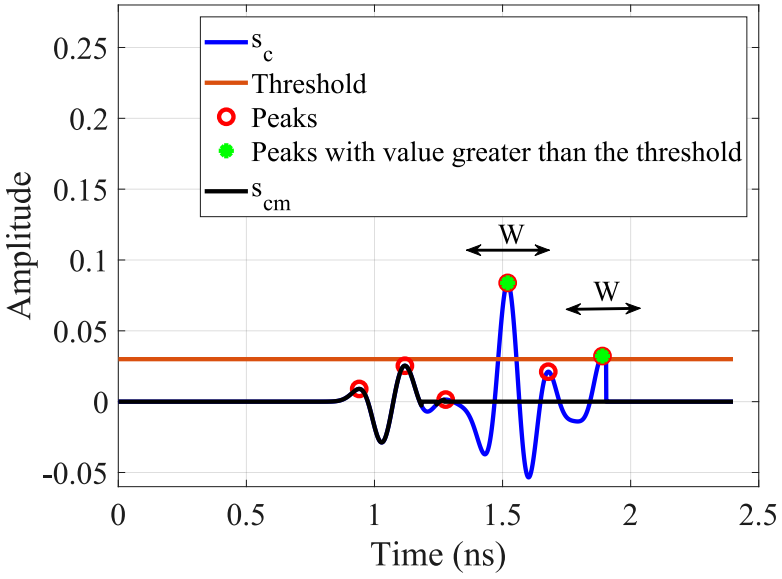

Figure 2.9: Illustration of the weak scatterer enhancement.

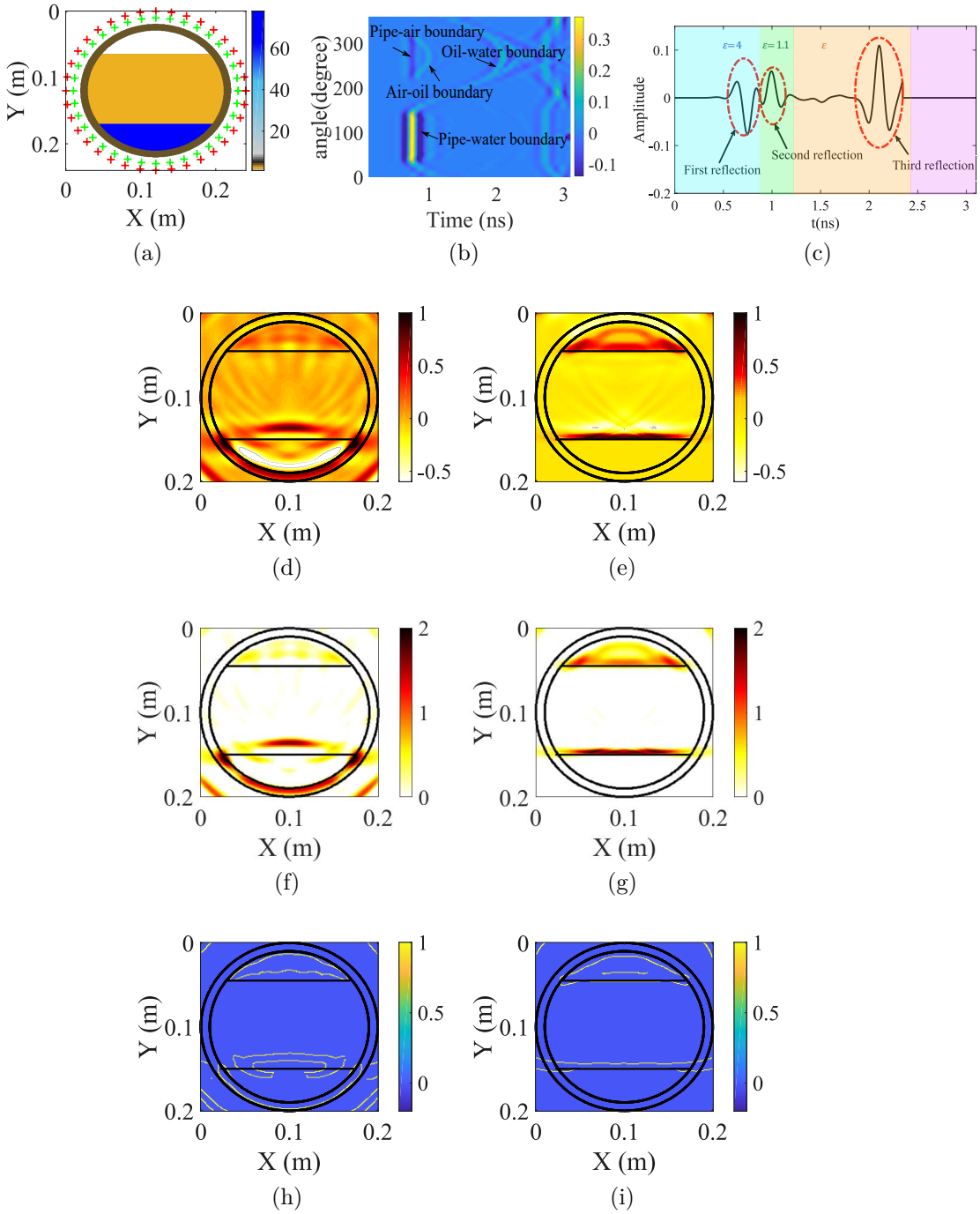

Figure 2.10: Stratified flow case. a) Simulation setup. b) Non-uniform group velocity in the sectional image reconstruction technique. c) Calibrated data. d) Conventional real image. e) Real image applying sectional image reconstruction. f) Conventional positive image. g) Positive image applying sectional image reconstruction. h) Conventional edge image. i) Edge image applying sectional image reconstruction.

2.3.3 Stratified Flow

In the stratified flow, different phases flow in a layered manner. Imaging of a stratified flow is barely addressed in multiphase flow studies. For instance, in [59], [83], two-phase stratified profiles are considered; however, the straight boundaries of the profiles are shown as curvy boundaries in the reconstructed images. MSI can provide a more accurate and reliable solution for MFM in a situation of stratified flow.

A numerical simulation setup is conducted, as shown in Fig. 2.10(a). In the layered structure, a uniform group velocity cannot be considered for the image reconstruction process. The sectional image reconstruction method, which is presented in [24], is applied to the stratified case. The principle behind the method consists of detecting different regions and then reconstructing the image using non-uniform group velocities. In a three-phase stratified flow, the first reflection from the bottom of the pipe is caused by the interface between the pipe and water. Similarly, the first reflection from the top of the pipe is caused by the interface between the pipe and air. The second and third reflections are caused by the air-oil and the oil-water interfaces, respectively. These three reflections appeared as peaks in the calibrated data and can be clearly seen in spatial-time data, as shown in Fig. 2.10(b). Hence, by finding peaks of $s_{c,i}$, the first, second, and third boundaries are identified. Then non-uniform group velocity based on the group velocity of the corresponding regions is used in the image reconstruction process, as shown in Fig. 2.10(c). The conventional real and positive images are shown in Figs. 2.10(d) and 2.10(f), respectively. The sectional real and positive images are shown in Figs. 2.10(e) and 2.10(g), respectively. As shown in Figs. 2.10(d) and 2.10(f), curved borders have appeared between layers. However, the borders in the sectional images are not curved anymore and provide a more accurate illustration of each

Table 2.5: Phase error of the simulated stratified flow.

Target (Phase)	**Phase area error (%) (conventional technique)**	**Phase area error (%) (sectional technique)**
Water	57.0	12.2
Air	41.0	10.3
Oil	4.6	3.4

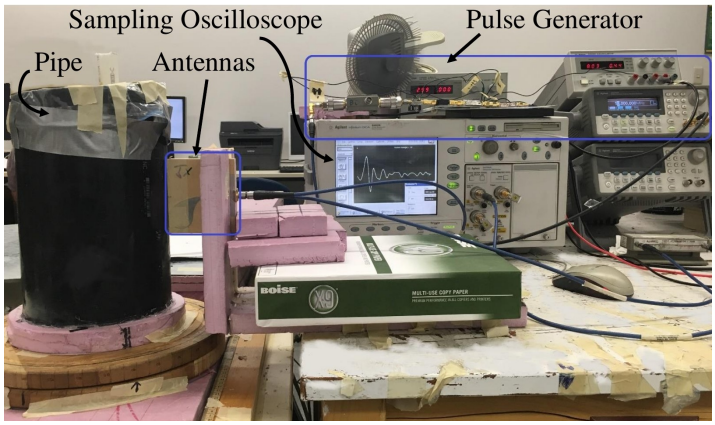

(a)

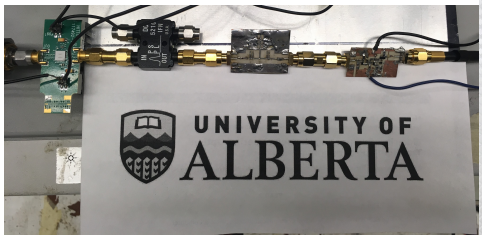

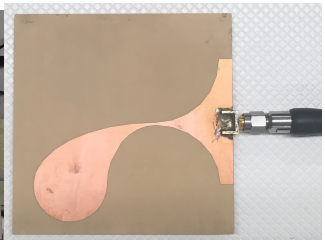

(b) (c)

Figure 2.11: a) Measurement setup. b) Pulse Generator. c) Vivaldi antenna.

phase. Table 3.4 suggests that the sectional image reconstruction improves the water, air, and oil flow rate errors to 12.2%, 10.3%, and 3.4%, respectively.

2.4 Experimental Validation

To evaluate the proposed method, several two-phase and three-phase scenarios are conducted. Fig. 2.11 illustrates the experimental setup, pulse generator, and Vivaldi antennas used as transmitter and receiver. The pulse generator feeds the sensors with a first derivative Gaussian pulse with an approximate FWHM of 82 ps, which corresponds to a -10 dB bandwidth of 5.9 GHz at 1

MHz PRF. The received signal is measured by a sampling oscilloscope and then processed to reconstruct the image and estimate the flow rate. In all the experiments, a polyvinyl chloride (PVC) pipe and diesel fuel are used to emulate the industrial setup since their dielectric constants are 4 and 2.1, respectively [62], [84]. The inner radius of the pipe is 7.7 cm with a 0.8 cm thickness. The first experiment is a two-phase flow monitoring with a water bubble, which is emulated by placing a water-filled pipe with a radius of 1.1 cm in the diesel. The calibrated signal is calculated using Equation (2.9), where s_{am} is the measured signal in the presence of the pipe containing the diesel. Hence, the reconstructed images would not include the pipe. As shown in Fig. 2.12(a), the positive image is blurry, and the edges are not fully matched to the dimension of the water bubble. This is because of transmitted pulses have an FWHM of 82 ps. By applying the impulsization technique on the calibrated data, the improved positive image is shown in Fig. 2.12(b). Although the conventional positive image of the target is smoother, the improved positive image is more precise in terms of bubble dimension. As mentioned in Table 3.5, the water and oil flow rate error improved to 15.0% and 0.3%, respectively.

In the second experiment, an additional pipe with an 11 mm radius filled with air is placed in the diesel. The distance between the two targets is 21 mm. The real and positive images are shown in Fig. 2.13. It should be noted that the dielectric constant of water is more than that of diesel, whereas the dielectric constant of air is less than that of diesel. Hence, the received signals from water and air have different polarities. Therefore, the water bubble has

Table 2.6: Experiment 1 phase error.

Target (Phase)	**Phase area error (%) (conventional technique)**	**Phase area error (%) (impulsization technique)**
Water	65.9	15.0
Oil	1.3	0.3

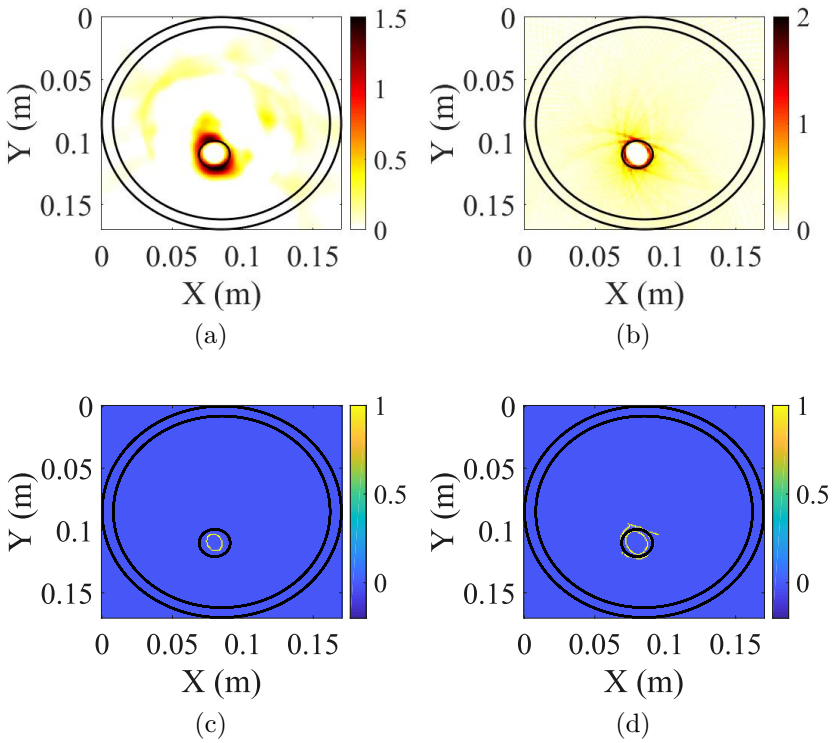

Figure 2.12: a) Experiment 1, two-phase scenario. a) Conventional positive image. b) Positive image applying impulsization. c) Conventional edge image. d) Edge image applying generalized impulsization.

a positive value, and the air bubble has a negative value in the reconstructed image. The Canny edge detector with a 0.6 threshold is applied to the real image, and only the stronger scatterer, the water bubble, is detected.

The proposed weak scatterer enhancement technique, as discussed in section 2.3.2, is applied to the calibrated data, and the results are shown in Figs. 2.13(b), 2.13(d), and 2.13(f). As it is presented in Table 3.6, the oil flow rate

Table 2.7: Experiment 2 phase error.

Target (Phase)	**Phase area error (%) (conventional technique)**	**Phase area error (%) (WSE technique)**
Water	10.0	10.8
Air	100.0	30.0
Oil	2.3	0.7

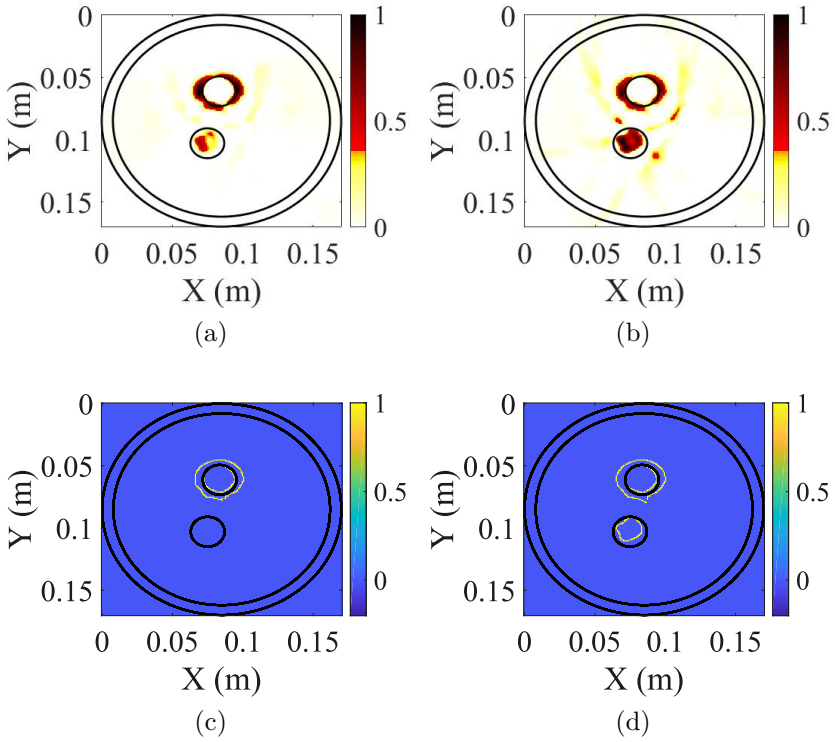

Figure 2.13: Experiment 2, three-phase scenario. a) Conventional positive image. b) Positive image applying weak scatterer enhancement. c) Conventional real image. d) Real image applying weak scatterer enhancement. e) Conventional edge image. f) Edge image applying weak scatterer enhancement.

Table 2.8: Experiment 3 phase error.

Target (Phase)	**Phase area error (%)**
Water	23.0
Air 1	18.0
Air 2	24.0
Oil	0.4

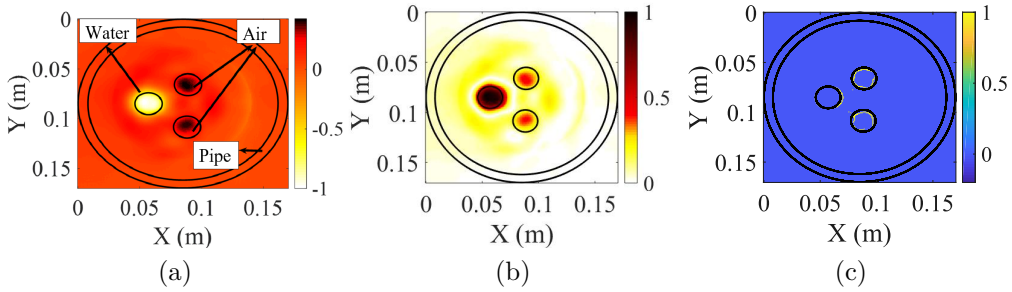

Figure 2.14: Experiment 3, three-phase scenario. a) Real image. b) Positive image. c) Edge image.

error improved to 0.7%.

The third experiment includes a water bubble and two air bubbles. The distances between the three targets are 15, 18, and 21 mm. The reconstructed real and absolute images are shown in Fig. 2.14. The Canny edge detector with a 0.3 threshold successfully identified three bubbles. The area and flow rate of each bubble are estimated and then flow rate errors are summarized in Table 2.8. It should be noted that, for the first three experiments, ε_r in the image reconstruction process is set to 2.1 based on prior knowledge.

The last experiment investigates the stratified flow situation. The setup includes a water layer, a diesel layer, and an air layer, from bottom to top. The height of each phase is 37 mm, 62.7 mm, and 55.3 mm, respectively. The sectional real, positive, and edge images are shown in Fig. 2.15, and the error of each layer is summarized in Table 2.9. These experiments, alongside the tailored signal processing techniques, may suggest that the UWB SAR technique might be a potential solution for MF monitoring and metering in industrial applications.

Table 2.9: Experiment 4 phase error.

Target (Phase)	**Phase area error (%)**
Water	16.9
Air	7.0
Oil	3.8

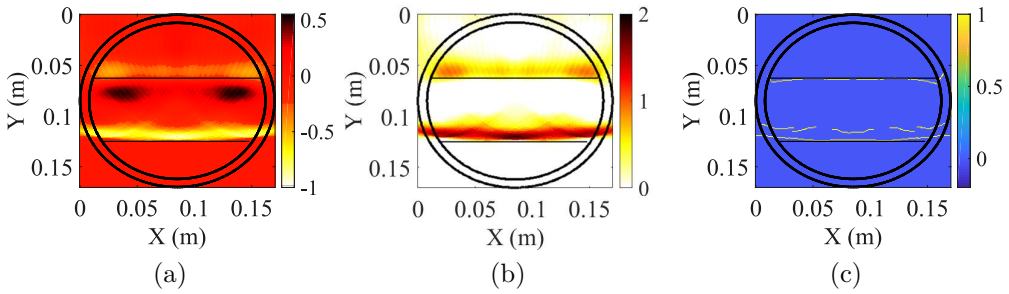

Figure 2.15: Experiment 4, three-phase stratified scenario. a) Sectional real image. b) Sectional positive image. c) Sectional edge image.

2.5 Limitations

The UWB SAR method is proposed for imaging, detection, and measurement of individual phases in multi-phase flow (MF), and exhibits notable strengths in scenarios characterized by balanced flow conditions. This technique can effectively capture and quantify the different phases—such as oil, water, and gas—when their proportions are stable and production rates are well-matched. However, its effectiveness diminishes when faced with dynamic flow situations where phase ratios fluctuate widely.

It also should be noted that MSI resolution of CSAR is limited, as per Eq. 2.8, meaning that imaging of the bubbles with a distance of smaller than expected resolution is not feasible. In the aforementioned experiments, a pulse with an FWHM of 82 ps, which corresponds to a -10 dB bandwidth of 5.9 GHz, is utilized.

$$\Delta_R = \frac{c}{3BW\sqrt{\varepsilon_r}} = \frac{3 \times 10^8}{3 \times 5.9 \times 10^9 \times \sqrt{2.1}} = 1.17\ cm \tag{2.15}$$

Hence, any two bubbles with a distance of less than 1.17 cm cannot be resolved and would appear as a single merged bubble in the images.

2.6 Conclusion

This chapter utilizes the UWB SAR technique to achieve multiphase monitoring and metering of crude oil pipelines. A range of scenarios involving two-phase and three-phase dispersed bubble flows, as well as stratified flows, are examined in the simulations and experiments. To begin, a two-phase scenario featuring a water bubble within a diesel pipe is investigated. The generalized pulse impulsization technique is employed to mitigate flow estimation errors. Subsequently, a three-phase scenario comprising a water bubble and an air bubble in diesel is studied. A method to enhance the imaging of weak scatterers is applied to improve the visualization of air bubbles in reconstructed images.

Furthermore, a more intricate situation involving two air bubbles and one water bubble is explored. Finally, a three-phase stratified flow experiment is conducted, employing the sectional image reconstruction technique to enhance image quality and flow estimation accuracy for each phase. Notably, the experiments consistently yield a crude oil flow estimation error of less than 4%. These results affirm the practical applicability of the proposed method within an industrial setting.

Chapter 3

Buried Object and Fluid Characterization

3.1 Introduction

Tunnel boring machines (TBMs) have been extensively used in the construction of transportation and utility tunnels around the world [85]. During tunnel construction, however, the TBMs are hampered by many complexities [86]. Difficulties found during the excavation due to unexpected or under-evaluated geological ground conditions are a common cause of damage. In glaciated geological conditions (e.g., Edmonton, Alberta), unexpected boulders in soil or sudden change from hard clay to unstable sand has resulted in cutter head damage, time, and cost overruns, adversarial relationships, and claims [86].

In addition, the TBM could also ram into unknown man-made obstructions, such as existing pipes or piles with inaccurate as-built information, boulders, abandoned metallic objects, or any hidden objects with archaeological or paleontological values. Tunneling engineers rely on either excavating a limited quantity of vertical boreholes during site investigation or taking core samples at the tunnel face in order to acquire geotechnical data and probe obstacles. This process is time-consuming and expensive. It also fails to provide accurate and timely information that is needed to detect the boulders or man-

Table 3.1: Comparison of the existing methods for buried object analysis.

Reference	Application	Measured parameter/parameters	Method	Computational Complexity	Thickness measurement	Limitations
[87]	Asphalt pavement	Dielectric constant and thickness of asphalt overlay (One layer)	Extended common midpoint (XCMP)	High	Yes	Minimum measured thickness: 45 mm
[88]	Soil characterization	Permittivity and conductivity of the soil (One half-space layer)	Full Inversion Wave (FIW)	Medium	No	Homogeneous half-space assumption
[89]	Pavement quality control	dielectric constant and conductivity of Five layers (Total thickness not individual thickness)	Inverse Analysis	Medium	No	Thickness of each layer should be known
[90]	Moisture content measurement for urban pavement	Moisture content measurement for urban pavement Permittivity (real part) and Thickness of pavement, (Two layers)	Ray-path Modelling Coherence (RM-C)	Medium	Yes	Thin low permittivity layer cannot be measured.
[91]	Characterization of polycaprolactone	Dielectric constant and conductivity of polycaprolactone (One layer)	Transmission line principle	Low	Yes	MUT should be placed as the substrate in a microstrip transmission line
[92]	Characterization of Concealed Body-Worn Explosive Threats	thickness, relative permittivity, and dielectric loss of explosive material (One layer)	Virtual source model	Low	Yes	Array measurement needed.
[13]	Complex Permittivity Extraction from SAR Images	Complex permittivity map	Reflection coefficient	Medium	No	Only for infinitely thick and nondispersive MUT /hl,Array measurement needed.
[93]	Characterization of two-layer absorbers	Complex permittivity and permeability (Two layers)	Reflection and transmission coefficients	High	No	MUT should be installed in a Coaxial transmission line
[94]	Characterization of reinforcing bars	Rebar diameter and cover thickness (thicknesses of two layers)	GPR-EMI Dual Sensor	Medium	Yes	Permittivity should be known
[95]	Wide-band complex permittivity and permeability measurement	Permeability and permittivity (one layer)	Transmission (CPW)	Low	No	MUT should be installed on top of CPW
[96]	Water content estimation	Dielectric constant and conductivity (two layers)	Model inversion (frequency domain)	High	No	The thicknesses should be known
This work	Analyzing the type of fluid inside a buried pipe	Complex permittivity of the sand, pipe and the fluid inside the pipe, Thickness of the sand, pipe wall (Three layers)	Transmission line method/optimization	Medium	Yes	Low loss material (tan $\delta < 0.4$)

made obstructions lying immediately ahead of the tunnel face. Other geological probing techniques that have been considered include acoustic holography and ground-penetrating radar (GPR) techniques. The development of GPR techniques that focus on detecting hidden objects has been a topic of research since the 1970s [97]. Early work in this field was motivated by applications in oil explorations [98]. Other applications of GPRs include seismic imaging, glaciology, sedimentology, hydrology, mining/tunneling, concrete/pavement evaluation, and archaeology [99]–[101]. In [102], UWB GPR is exploited for pavement profiling by time-delay estimation algorithms. However, this algorithm is limited to the pulse width. Lambot *et al.* [103] extracted subsurface material characteristics using a UWB stepped-frequency continuous-wave (SFCW) radar and the results of this research are promising. The only concern is the computational complexity of the algorithm and the frequency dependency of the real part of relative permittivity is ignored to limit the number of unknowns. The existing state-of-the-art research for material characterization and their limitations is summarized on Table 3.1. Although much research has proposed material characterization, they suffer from long acquisition data collection (number of measurements), high-computational time, being destructive, or failing to characterize multi-layer MUTs.

This chapter presents an investigation of ultra-wideband (UWB) radar techniques [11], [43], [104]–[107] that analyze the geological conditions present in the tunnel face using material characterization. The material of the buried object is determined by comparing the measured dielectric constant with the priory developed material electrical properties catalog. Also, fluid identification within the buried pipe using UWB radar is presented and experimented.

3.2 Methodology

To estimate the dielectric constant of buried objects, transmitting and receiving antennas are placed pointing at the surface of interest, as illustrated in Fig. 3.1. The transmitting antenna (Tx) radiates a sequence of short pulses toward the ground, while the receiving antenna (Rx) captures scattered signals from the ground and buried objects. In the measurement scenario, an additional layer of air (layer 5) is introduced at the bottom of the soil, see Fig. 3.1. In other words, the ground layer (i.e., layer 4 in Fig. 3.1) is terminated with a free-space layer so that the unwanted reflection from the layer4-layer5 interface can be removed with time gating. This is proposed because it is challenging to emulate an infinitely extended ground after the buried object in a lab condition. It should be noted that the introduction of the additional layer of air does not compromise the performance of the method when applied to buried objects in the ground since in-ground soil continues, and there will not be any reflections.

The transmitting antenna (Tx) is excited by a first derivative Gaussian pulse, $s(t)$, which radiates into the air in layer 1. The radiated signal propagates down to layer 2 (soil) and is scattered by layers 2, 3, 4, and 5. The scattered signal propagates back to the receiving antenna (Rx) and is received as $r(t)$. The transfer function of the antennas in transmitting and receiving modes are $g_t(t)$ and $g_r(t)$, respectively [108].

Estimating the transfer function of soil with a buried object, $y_s(t)$, from the measured signal $r(t)$ is a crucial step in estimating the dielectric constant of the buried object. Measured received signal, $r(t)$, contains different components such as source signal, antenna effect, antenna coupling and other reflections caused by nearby scatterers such as radar fixtures and mounting vehicles. Calibration measurements are carried out to decouple all the un-

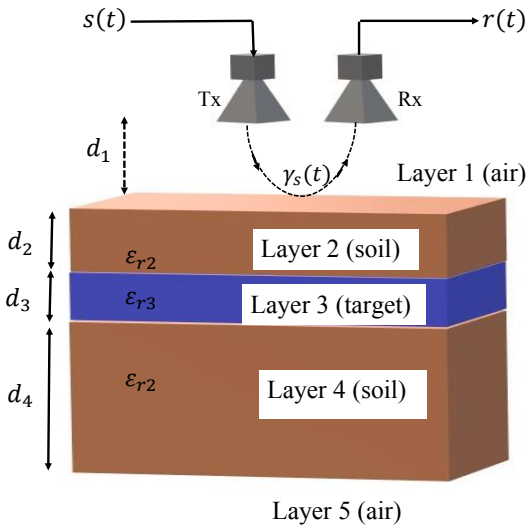

Figure 3.1: Multilayered dielectric slab that models the soil and buried object.

desired information so that $y_s(t)$ can be estimated. In the first calibration measurement, $r_a(t)$, the received signal is recorded when the antennas radiate into free space, and it contains the effect of mutual coupling between the antennas, scattering from nearby objects and measurement fixers. In the second calibration measurement, $r_m(t)$, the received signal is recorded when the antennas point at a large thin metal sheet placed on the soil surface. The analysis provided in [109] showed that $\gamma_s(t)$, which is the reflection coefficient, can be derived as

$$\gamma_s(t) = F^{-1}\{\Gamma_s(f)\} = F^{-1}\Big\{ - \frac{F[r(t) - r_a(t)]}{F[r_m(t) - r_a(t)]}\Big\} \tag{3.1}$$

where $F\{...\}$ and $F^{-1}\{...\}$ are Fourier and inverse Fourier transforms, respectively; $\Gamma_s(f)$ is the Fourier transform of $\gamma_s(t)$; $r_a(t)$ and $r_m(t)$ are the two received signals for calibration measurements; and $r(t)$ is the measured received signal from soil with the buried object.

On the other hand, $\gamma_s(t)$ can also be derived, assuming plane wave propagation, by using the analogy of impedance transition in transmission line

theory [110] as

$$\gamma_s(t) = F^{-1}\Big\{\frac{Z_{1,2} - Z_{01}}{Z_{1,2} + Z_{01}}\Big\} \tag{3.2}$$

where

$$Z_{1,2} = Z_{02}\frac{Z_{2,3} + Z_{02} \times tanh(\gamma_2 d_2)}{Z_{02} + Z_{2,3} \times tanh(\gamma_2 d_2)} \tag{3.3}$$

$$Z_{2,3} = Z_{03}\frac{Z_{3,4} + Z_{03} \times tanh(\gamma_3 d_3)}{Z_{03} + Z_{3,4} \times tanh(\gamma_3 d_3)} \tag{3.4}$$

$$Z_{3,4} = Z_{04}\frac{Z_{05} + Z_{04} \times tanh(\gamma_4 d_4)}{Z_{04} + Z_{05} \times tanh(\gamma_4 d_4)} \tag{3.5}$$

$$\gamma_i = \frac{2\pi f\sqrt{\varepsilon_{ri}}}{c} \quad i = 2, 3, 4, 5 \tag{3.6}$$

$$Z_{0i} = \frac{\eta_0}{\sqrt{\varepsilon_{ri}}} \quad i = 2, 3, 4, 5 \tag{3.7}$$

ε_{r1}, ε_{r2}, ε_{r3}, ε_{r4}, and ε_{r5} are the dielectric constants of the multilayered dielectric slab shown in Fig. 2; d_2, d_3, and d_4 are the thicknesses of the dielectric layers 2, 3 and 4; f is the frequency of interest; η_0 is the intrinsic impedance of free space (377Ω) and c is the speed of light in free space. Please note that all layers are assumed to be homogeneous in the above formulation. To satisfy the assumption of plane wave propagation that is required in the theoretical derivations of $\gamma_s(t)$, the antennas used in the measurement must be high-gain antennas, such that, the illumination area is smaller than the transverse area of buried objects. Hence, the ground and buried objects can be approximated to be horizontally layered, and the edges of the objects are not visible to the antenna.

Therefore, based on the analysis described above, $\gamma_s(t)$ can either be computed from measurements with (1) or derived with (2). If the dielectric constant of the soil (ε_{r2} and ε_{r4}) is known, theoretically, (1) and (2) can be equated, and a simple solution can be found for the depth, thickness and dielectric constant of the buried object. This assumption is valid because the dielectric constant of soil can be measured before the actual buried object measurement. However,

because of conditions such as measurement noise, inhomogeneous ground, and surface roughness, it is not feasible to reach a simple solution.

3.2.1 Minimization

To find a practical estimate of the solution, more complicated methods such as parameter estimation techniques are applied in [109]–[111]. In this research, a search algorithm has been proposed to recover the depth, thickness, and dielectric constant of the buried object. Let M_0 be the absolute difference between the measured and the theoretical reflection coefficients for all possible combinations of physical and electrical properties. The goal of minimization is

$$\begin{gathered} M_0(d_2, d_3, \varepsilon'_{r_3}, \varepsilon''_{r_3}, f_0) = \\ min\{|\Gamma_{sc}(f_0) - \Gamma_t(d_2, d_3, \varepsilon'_{r_3}, \varepsilon''_{r_3}, f_0)|\} \end{gathered} \tag{3.8}$$

$$\varepsilon_3 = \varepsilon_0(\varepsilon'_{r_3} - j * \varepsilon''_{r_3}) \tag{3.9}$$

where d_2, d_3, and ε_3, are the depth from the surface, the thickness of the buried object, and the complex permittivity of the buried object, respectively. It should be mentioned that (5) becomes

$$Z_{3,4} = Z_{04} \tag{3.10}$$

due to the time gating. The pseudo-code of the minimization algorithm is presented in algorithm 2. For each frequency, the unknown parameters (i.e., d_2, d_3, ε'_{r3}, and ε''_{r_3}) vary such that the absolute difference between the measured reflection coefficient and the theoretical reflection coefficient becomes minimal. D_{2max}, D_{3max}, ε'_{3max}, and ε''_{3max} can be set based on any prior knowledge of the experimental scenario. However, in the absence of any prior information, these values should be high enough to achieve the global minimum of the M_0 function.

Algorithm 2 Proposed minimization method(frequency dependant)

Minimization of M_0:
Γ_{sc}: input, $d_2, d_3, \varepsilon_{r3}$: output
for $f = f_0, ..., f_0 + N\Delta f$ do
  $Min \leftarrow$ large number ($i.e.$100),
  for $x_2 = 0, ..., D_{2max}$ do
    for $x_3 = 0, ..., D_{3max}$ do
      for $x_4 = 1, ..., \varepsilon'_{3max}$ do
        for $x_5 = 0, ..., \varepsilon''_{3max}$ do
          if $|\Gamma_{sc} - \Gamma_t| < Min$ then:

$$d_2(f) = x_2,$$
$$d_3(f) = x_3,$$
$$\varepsilon_{r3}(f) = x_4 - jx_5,$$
$$Min \leftarrow |\Gamma_{sc} - \Gamma_t|,$$

3.2.2 Measurement Procedure

To validate the above methodology, a measurement setup for the buried object identification is illustrated in Fig. 3.2. The soil used in the experiment is obtained from excavated tunnel projects in Edmonton. Slabs of different materials are buried in the soil, one at a time, so that the proposed identification method is tested for different materials. As shown in Fig. 3.2, the soil and buried objects are placed in an open box ($\varepsilon_r = 1.03$). The box is placed at 38 cm above the ground to provide a sufficient distance between the box and the ground. This gap provides a sufficient time interval to eliminate reflections from the ground. The radar transmitter generates a train of first derivative Gaussian pulse at 10 MHz pulse repetition frequency with a peak-to-peak voltage of 2 V. The radar receiver consists of a sampling oscilloscope (Agilent DCA 86100B) that samples the signal at 40 GS/s. Recorded signals are processed off-line. For the measurements, Vivaldi antennas [21] are placed in a monostatic configuration, 21 cm above the soil surface. The measurement procedure can be summarized into three steps: First, $r_a(t)$ is recorded in free

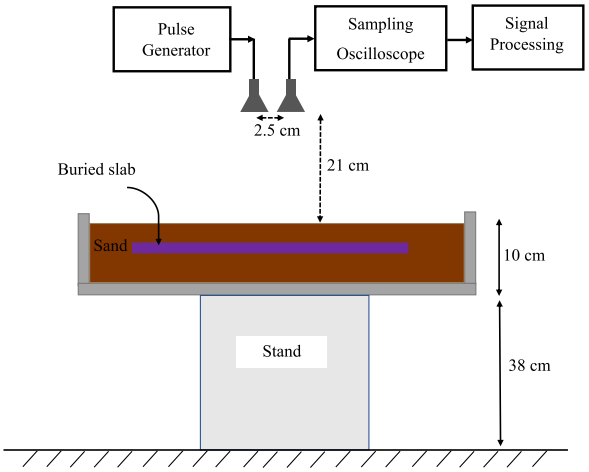

Figure 3.2: Experimental setup to estimate the dielectric properties of buried objects.

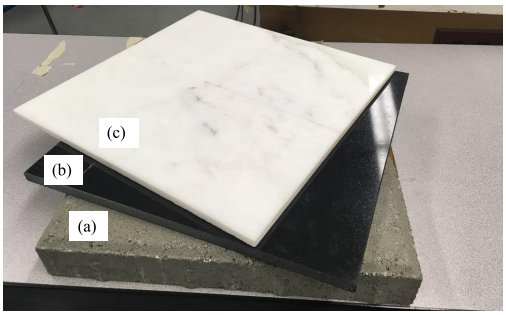

Figure 3.3: Photo of the objects used for identification while buried in tunnel soil; a) concrete slab, b) granite slab, c) marble slab.

space without the presence of the sand and the buried slab. Second, a large thin aluminum sheet ($300 \times 300mm^2$, $\sigma = 3.56 \times 10^7$ S/m) is placed on top of the sand and the $r_m(t)$ is recorded. Finally, $r_s(t)$ is measured in the presence of the sand with the buried slab. Different dielectric materials that frequently encountered in tunnel construction are shown in Fig. 3.3. Before the dielectric properties of buried objects can be estimated, the dielectric constant of soil should be measured and determined. To do that, soil is characterized by two different layer thicknesses (4 cm and 5.5 cm). Before each measurement, the soil surface is carefully re-leveled to minimize errors due to the surface tilt and surface roughness. Fig. 4.5(a) shows the measured dielectric constant and loss tangent of the soil in black and blue lines with respect to frequency. The red line indicates the measured dielectric constant with standard dielectric probe measurement. The average dielectric constant and loss tangent of the soil are found to be 3.35 and 0.02, respectively. It should be noted that for the free space measurements, ε_2 and ε_4 are set to ε_0. The only unknown parameters are d_3, ε'_{r3}, and ε''_{r_3}. The buried objects (Fig. 3.3) in the soil are: granite slab ($30 \times 30 \times 1.0\ cm^3$), marble slab ($30 \times 30 \times 1.0\ cm^3$), and concrete slab ($34 \times 34 \times 4.2\ cm^3$). The thicknesses of the objects are first measured with an vernier caliper for verification purposes. In addition, the dielectric constants of the slabs are verified by free space measurements. The $r_a(t)$, $r_s(t)$, and $r_m(t)$ are measured and the minimization problem, provided in (3.9), is performed. Figs. 4.5(b)-(d) compare the measured electrical properties of the buried objects in soil with free space measurements. In all cases, buried object characterization results agree to the free space measurement results. In order to find the value of each unknown, the values of the unknown are averaged over the number of frequencies

$$D_2 = \frac{1}{N+1} \sum_{i=1}^{N+1} d_2(f_0 + (i-1)\Delta f) \tag{3.11}$$

Table 5.1 summarizes the measured dielectric constants of the buried objects from three measurement methods – free-space measurement, buried measurement, and dielectric probe measurement. As can be seen in Table 3.3, the dielectric constant of the buried objects varies slightly from the free space and dielectric probe measurements.

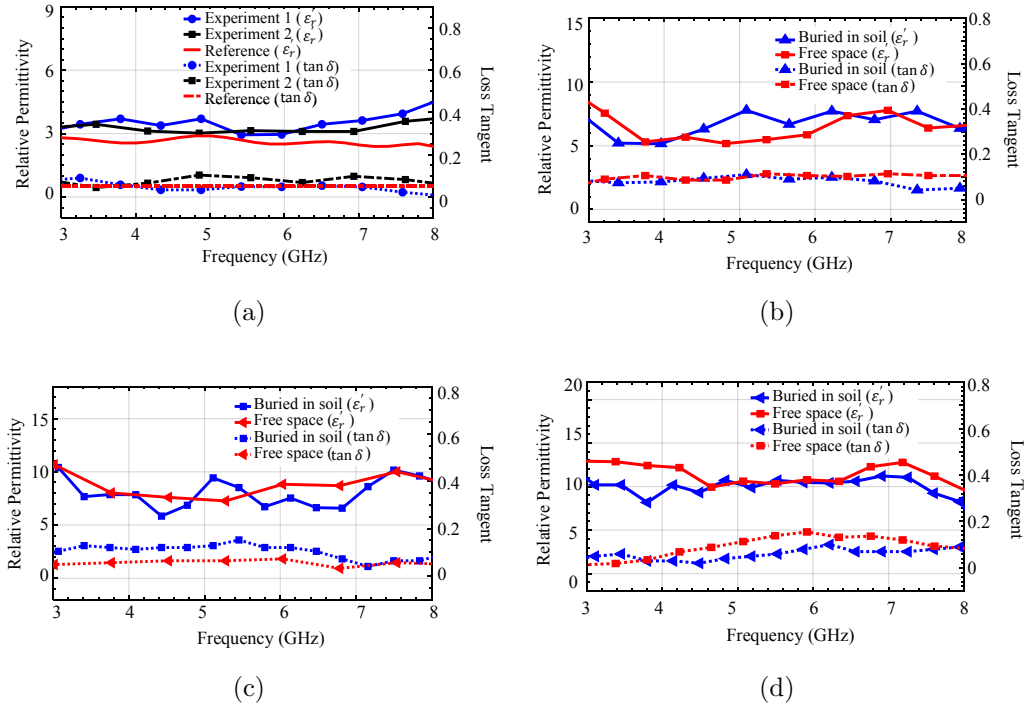

Figure 3.4: a) Measured dielectric constant and loss tangent of the sand. b) Measured dielectric constant and loss tangent of the concrete slab in free space and in soil. c) Measured dielectric constant and loss tangent of the marble slab, and d) Measured dielectric constant and loss tangent of the granite slabs in free space and in soil.

Measured thicknesses of the buried objects using the proposed technique are compared to the free space and vernier caliper measurements in Table II. Comparison shows that an average accuracy of 1.5 mm in estimating the thicknesses of the buried objects has been achieved. The measurement results demonstrate the capability of low-power UWB radar to identify buried objects through their dielectric properties.

Table 3.2: Measured dielectric constants of the buried objects.

Material	Free space measurement	Error	Buried measurement	Error	Dielectric probe
Sand	3.31	14.5%	N.A.	N.A.	2.89
Concrete	6.72	N.A.	7.01	N.A.	N.A.
Marble	8.68	0.9%	8.38	2.5%	8.6
Granite	9.65	4.7%	10.39	12.9%	9.2

3.2.3 Discussions on the Optimization Function

The minimization of M_0 is performed by Algorithm 1. In this section, by illustrating the objective function of M_0, the uniqueness and stability of the proposed minimization algorithm within the limited parameter space is studied. As it is mentioned earlier, the unknown parameters are d_2, d_3, ε'_{r3}, and ε''_{r_3}. In order to illustrate the objective function planes, two parameters are varied and the rest of the parameters are held constant at their true values and the values of M_0 is plotted [112]. Hence, these surfaces are only sampled planes of the full four-dimensional parameter space.

The investigated area is performed in large parameter space: $0.001 < d_2 < 0.04$; $0.001 < d_3 < 0.02$; $1 < \varepsilon'_r < 15$; and $0 < \varepsilon''_r < 3$. For these four parameters, there are six possible surface functions: $\varepsilon'_r - \varepsilon''_r$ plane, $\varepsilon'_r - d_2$ plane, $\varepsilon'_r - d_3$ plane, $\varepsilon''_r - d_2$ plane, $\varepsilon''_r - d_3$ plane, and $d_2 - d_3$ plane. Fig 3.5 (a)-(f) show these six planes at $f = 6.22$ GHz and the solution to the M_0 function is marked as a red circle in each case. For each plane, the M_0 function demonstrates a well-defined minimum within the bounded parameters space if the rest of the parameters are set to true values. These plots confirm the solution is partially unique. It should be noted that the response plane can be plotted for other frequencies as well.

Fig. 3.5 (b)-(f) present the response surfaces have several local minima and one global minimum within the limited range. In other words, a locally global

solution is demonstrated within the bounded range of unknowns. Note that to not trap to the local minimums, the steps for d_2 and d_3 should be selected small. The steps for d_2 and d_3 are chosen 1 mm and 0.2 mm, respectively. The step for parameter d_3 is smaller than d_2 because more accuracy is needed for the buried object thickness. It should be noted that if the step for d_2 is chosen to be 0.2 mm, the same response surface is expected, only with much more computational time. The step for both the ε_r' and ε_r'' are set to be 0.1 which leads to 141 and 31 iterations for each loop. Considering the 40 and 96 iterations for parameters d_2 and d_3, a total number of 16784640 calculations of the M_0 function is performed.

3.3 Sensitivity of the Proposed Technique

In many practical cases, the multilayered dielectric slab model (Fig. 3.1) is not thoroughly satisfied. In other words, the MUT is not a flat object, and the thickness is non-uniform. Consequently, the input impedance of the multilayered dielectric slabs does not strictly follow Eq. 3.3. As a result, some errors are introduced to the objective function, M_0. In order to study the effect of the MUT with a non-uniform thickness, the marble slab with various surface roughness is considered, and simulations are conducted using CST Microwave Studio [113]. The tabulated surface impedance exploits the Hammerstad-Jensen model [114] to describe the effect of surface roughness on the impedance, as shown in Fig. 3.6(b). This empirical model generally leads to a violation of Kramers-Kronig [115]. The causality is enforced to the simulations to construct an imaginary part of kappa (i.e., dielectric constant) by means of a Hilbert transform of the Hammerstad-Jensen-modified real part, such that Kramers-Kronig is fulfilled [113]. The marble slab ($\varepsilon_r = 8.6 - j0.1$) with a three-layer configuration is the MUT, as it is demonstrated in Fig.3.6(b),

Table 3.3: Measured thickness of the buried objects.

Object	Vernier Caliper	Free space	Buried in Soil
Sand	40-41	39.5	N.A.
Concrete slab	42.80	42.2	41.3
Marble slab	10.70	10.6	10.3
Granite slab	10.34	11.3	10.8

where Δ_1 is the RMS tooth height of Layer 1. Surface roughness (RMS) of the outer layers (layers 1 and 3) is varied from 2 mm to 10 mm, and the calibrated signals are collected. Layer 2 is considered to be 10 mm and $\Delta_2 = 0$. The recorded data is fed to the minimization algorithm 1, and the averaged retrieved real part of complex permittivity vs. surface roughness is illustrated in Fig. 3.7. This analysis shows a surface roughness of 10 mm or 1 cm results in 25% error; and it is convenient to apply the proposed technique approximately up to 9 mm surface roughness if 15% error of the estimated real part of complex permittivity can be tolerated.

3.4 Identification of Fluids in a Buried Pipe

Several man-made obstacles such as crude oil pipes and sewage pipes, can be found in the tunnel excavation and accidents while tunneling can have critical damage to the metropolitan services or/and the TBM itself. Identification of the fluid flows inside the pipe is crucial and needed for the TBM operations. UWB radar technology can be applied to estimate the material properties of the fluid inside the pipe that is buried in the sand. The methodology is similar to the one presented in the previous section. The only difference is that the dielectric constant of the third layer in Fig 3.1 is unknown. In other words, in addition to d_2, d_3, ε'_{r3}, and ε''_{r3}; ε'_{r4} and ε''_{r4} are also unknowns and need to be estimated. Hence, the new minimization problem can be formulated as

follows:

$$M_0(d_2, d_3, \varepsilon'_{r_3}, \varepsilon''_{r_3}, \varepsilon'_{r4}, \varepsilon''_{r4}, f_0) = \\ min\{|\Gamma_{sc}(f_0) - \Gamma_t(d_2, d_3, \varepsilon'_{r_3}, \varepsilon''_{r_3}, \varepsilon'_{r4}, \varepsilon''_{r4}, f_0)|\} \tag{3.12}$$

where Γ_{sc} and Γ_t are the measured reflection coefficient and the theoretical reflection coefficient, respectively. It should be noted that the radius of the typical pipes is in the range of 0.1 to 9 m [73], [116]. Hence, the dimensions of the pipe are large compared to the antennas and the flat surface model (as shown in Fig. 3.1) is valid but approximate.

The existing pipes can be categorized into three main types: crude oil pipes, sewage pipes, and water pipes. The dielectric constant of the crude oil is reported to be 2.5-3 [117]. The dielectric constant of the sewage is in the range of 20-45 [118], and the real part of water's relative permittivity is reported to be 78 [119]. For this problem, two unknowns are added and the search algorithm may not be as suitable as before since two inner loops with a relatively large number of iterations are added. To perform the minimization (3.12), genetic algorithm (GA) is applied [120]. Briefly, the GA explores the large 6D space of the unknowns and selects the solutions that minimize the objective function, which is the absolute difference between the theoretical and the measured reflection coefficients.

3.4.1 Experimental Validation

In all three experiments, a large cube plastic box ($40 \times 59 \times 40\ cm^3$) is filled with sand to emulate the practical situation. Then, a polyvinyl chloride (PVC) pipe is placed inside the sand. The minimum distance from the container wall to the pipe is in the range of 10-11.5 mm. The inner and outer diameters of the pipe are 77 mm and 85 mm, respectively. To evaluate the functionality of the UWB-radar technique for identifying the fluid inside the pipe, three experiments are conducted. First, the pipe is filled with vegetable oil, which is emulating

crude oil since the dielectric constant of both materials is 2.5, as reported in [121], [122]. The GA ran for a maximum number of generations of 4000 with 0.01 migration rate, 100% crossover rate, and 200-member population. The estimated dielectric constant and loss tangent of the vegetable oil and the measured ones with the dielectric probe are illustrated in Fig. 3.9(a).

In the second experiment, the pipe is filled with acetone to emulate the sewage pipe since the permittivity of the acetone is reported to be 20.7 according to [123]. For the last experiment, the pipe is filled with tap water and the optimization is performed to minimize (3.12). The results for the acetone pipe and the water pipe are presented in Figs. 3.9(b) and 3.9(c), respectively. In all three cases, the pipe thickness and the pipe dielectric constants are estimated as well. Fig. 3.9(d) shows the estimated dielectric constant of the pipe in three experiments. The results of the three experiments are all in agreement with each other. Table 3.4 summarizes the estimated average dielectric constants of the fluids and compares them to the average dielectric probe measurements. Also, the average dielectric constant of the pipe is presented in Table 3.4. The depths of the buried pipe and the pipe thickness are also estimated for the three experiments and presented in Table 3.5. The discrepancies are attributed to the non-uniform distribution of pebbles in the soil, the tilted container, and the tilted alumni sheet, as shown in Fig. 3.8. It should be noted that the permittivity of the vegetable oil and the PVC pipe is very close to the sand's permittivity. Thus, only a small portion of the transmitted signal is reflected from the pipe-vegetable oil interface and the $r_s(t)$ carries small information about ε_{r4}. Hence, the estimated parameters of this experiment are likely to be less accurate compared to the second and third experiments.

To compare the execution time of the MSE [108] and GA, both algorithms are analyzed for the above three fluid characterization experiments. Table VI

presents the optimization run time for three fluid identification experiments in minutes. The optimization is performed on a computer with the following specifications: Intel(R) Core (TM) i7- 8700 CPU, @ 3.2GHz, and 32.0 GB RAM. It is shown that the averaged optimization speed of GA is approximately 28 times faster than MSE.

Table 3.4: Measured dielectric constant of the fluids inside the buried pipe.

Fluid	Estimated dielectric constant	Reference	Estimated pipe dielectric constant
Vegetable oil	3.31 - 0.116i	2.82- 0.101i	3.19 - 0.139i
Acetone	21.50 - 0.013i	24.30-0.152i	4.78 - 0.034i
Water	73.09 - 0.082i	74.76- 0.261i	3.61 - 0.092i

Table 3.5: Measured depth and pipe thickness in mm.

Variable	True d_2	Estimated d_2	True pipe thickness	Estimated pipe thickness
Vegetable oil	10.7	13.8	8.0	11.4
Acetone	11.5	13.8	8.0	6.9
Water	11.0	12.8	8.0	11.0

Table 3.6: Optimization time in minutes.

Experiment	Vegetable oil	Acetone	Water	**Average**
MSE [108]	3.23	31.90	37.23	**24.12**
GA (Our work)	0.48	0.49	1.59	**0.85**

3.5 Conclusion

In this chapter, the results of our investigation on the application of radar techniques for acquiring near online geological conditions of a tunnel face is presented. The electrical properties of buried objects are used to identify different buried objects. First, the UWB radar technology is exploited to identify the buried material through the dielectric constant. The dielectric properties of the buried objects are measured to reasonable accuracy. Second,

the identification of the fluids inside a buried pipe is investigated. Based on the electrical properties of the fluid in the pipe, sewer pipes, and oil pipes can be distinguished. It is shown that the GA improves the optimization speed 28 times compared to MSE. All the mentioned experiments confirm the potential of the ultra-wideband technology in estimating the dielectric properties of buried objects and identifying the materials and geological features. Based on these investigations, it is believed that by integrating UWB sensors into TBM and having appropriate power levels and frequency bandwidths, it is possible to acquire the near real-time geological features of the tunnel face up to a meter.

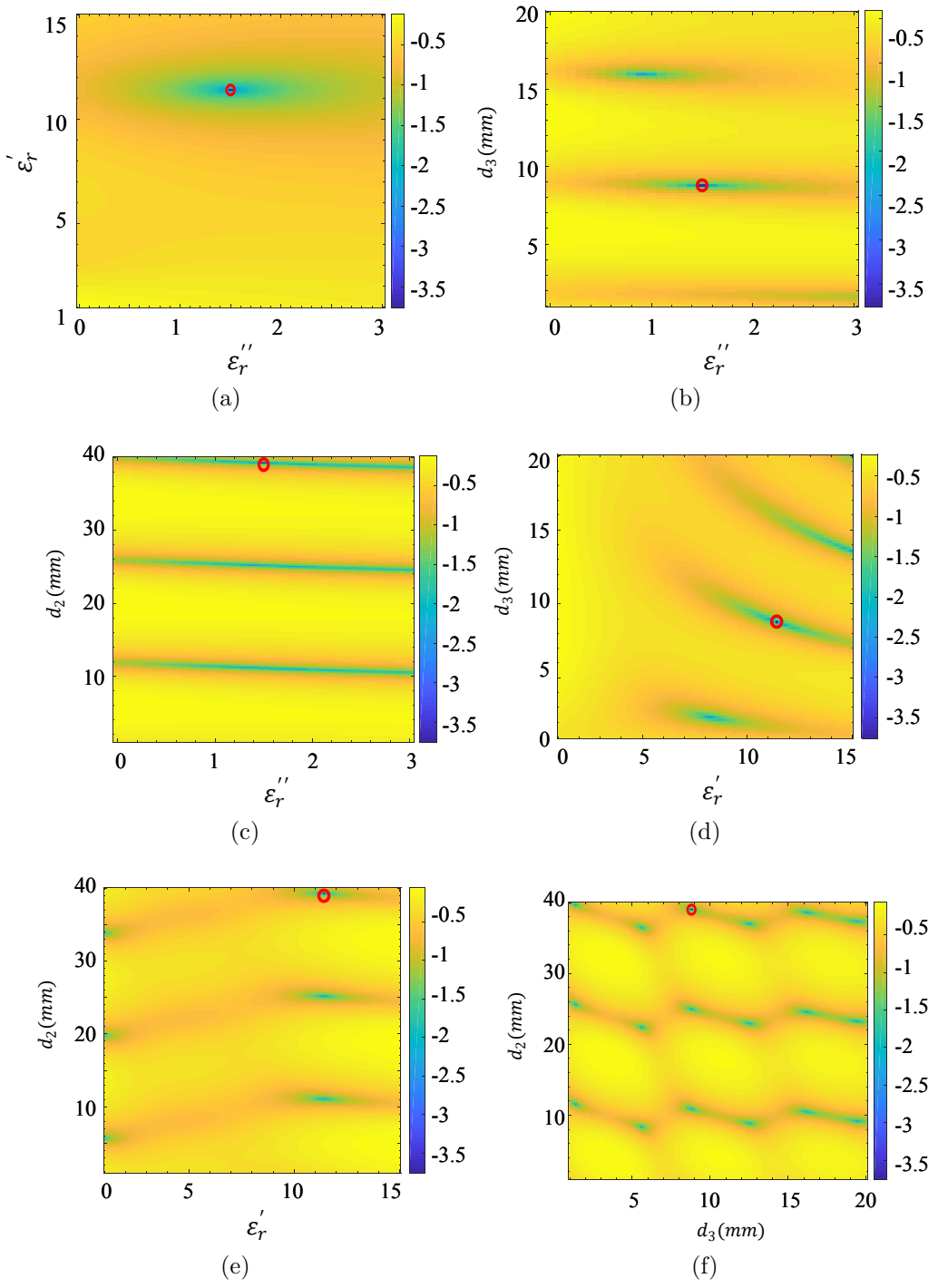

Figure 3.5: Response planes of the objective function logarithm: $log_{10}\ (M_0)$; a) $\varepsilon_r'' - \varepsilon_r'$ plane, b) $\varepsilon_r'' - d_3$ plane, c) $\varepsilon_r'' - d_2$ plane, d) $\varepsilon_r' - d_3$ plane, e) $\varepsilon_r' - d_2$ plane, f) $d_3 - d_2$ plane.

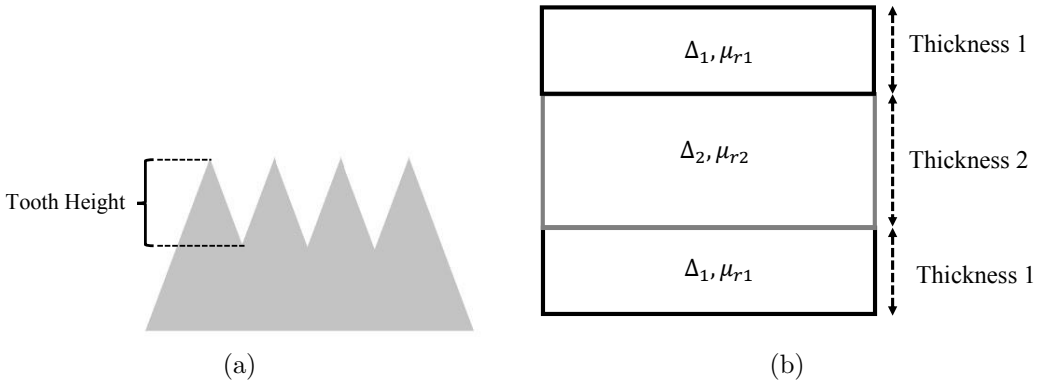

Figure 3.6: a) Hammerstad-Jensen roughness model. b) Three-layered marble structure in CST simulations.

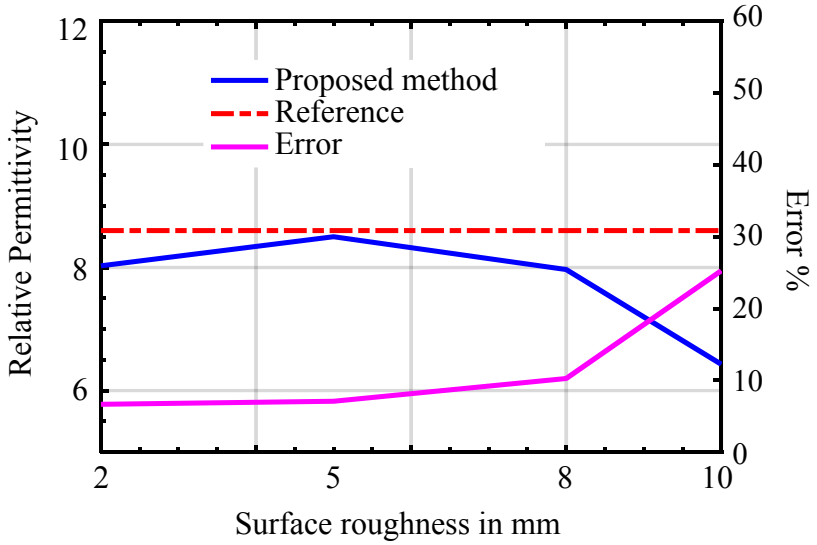

Figure 3.7: Evaluation of the proposed method as a function of surface roughness.

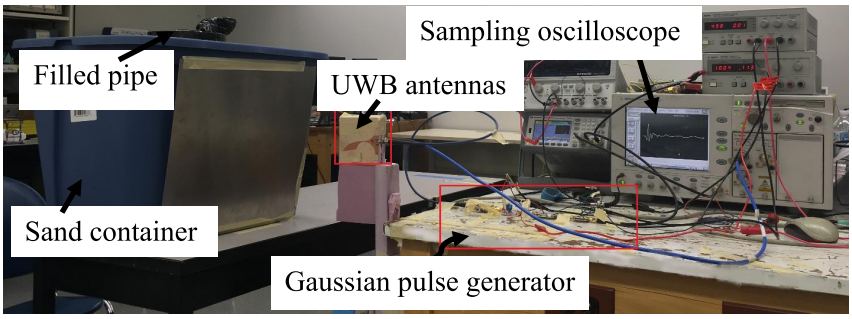

Figure 3.8: Experimental setup to estimate the dielectric properties of the fluid inside the PVC pipe that is buried in the soil.

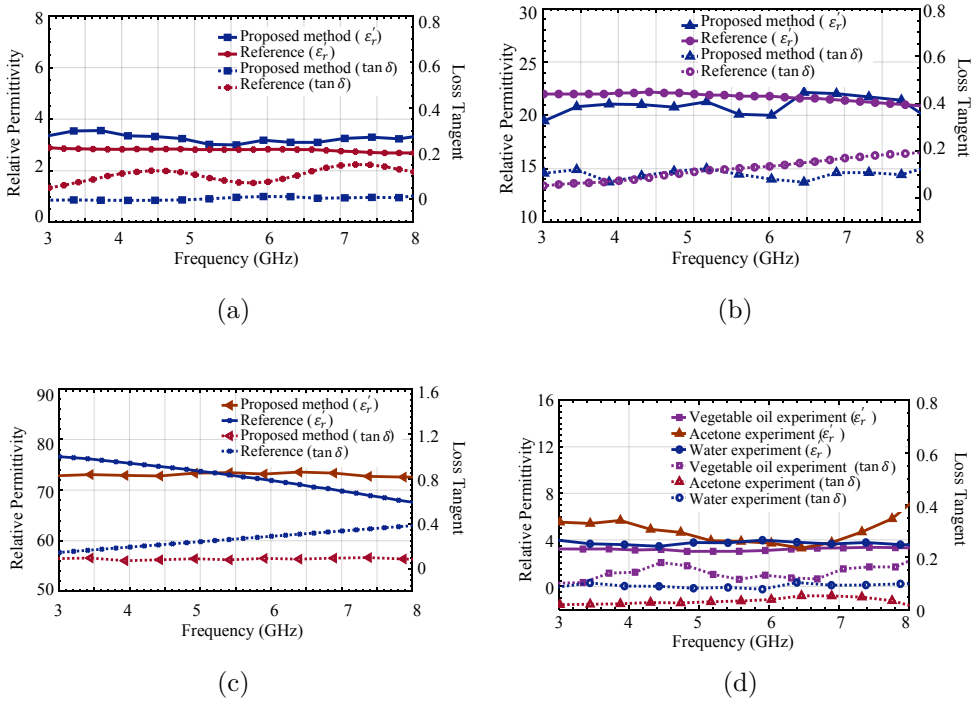

Figure 3.9: a) Measured dielectric constant and loss tangent of vegetable oil, acetone, and water inside the pipe. d) Estimated dielectric constant and loss tangent of the PVC pipe for three experiments.

Chapter 4

Feature Extraction and Object Classification from GPR Data

4.1 Introduction

Ground-penetrating radar (GPR) has been extensively used for construction, biomedical, and military applications thanks to its non-destructive, efficient, and high-resolution properties [124]. One of the most attractive benefits of the GPR is the ability to image the subsurface objects in the case of limited access to the target scene.

The data acquisition in GPR systems can be either in the time domain or frequency domain. In the case of the time domain, the GPR system transmits a sequence of impulses toward the target scene and records the backscattered signals in the time domain. In the case of the frequency domain, the GPR system collects the frequency response of the backscattered signals. The process of converting the space-time or space-frequency domain data into 2D or 3D images is called migration or focusing methods. The most popular migration methods are hyperbolic summation, Kirchhoff's migration, frequency-wavenumber migration, and back-projection method [37]. In this chapter, the focus is on time-domain global back-projection (TD-GBP).

The reflections from the buried object need to be manually marked in many

industrial GPR systems [125]. Furthermore, subsequent classification of the buried object is required for GPR data interpretation, even with a high-quality focused image. Conventional neural networks (CNN) and classification have been used for landmine detection. Deep learning models are reported to be more effective for GPR data interpretation since it can be affected enormously by experimental noise and the environment clutter [125]. Several studies have adopted machine learning models for GPR data classification [124]–[126]. In [124], the support vector machine classifiers have been suggested for material classification of the underground objects in a noisy environment. Moreover, a deep learning classifier has been proposed based on multi-channel GPRs [125]. Furthermore, a deep convolutional network has been presented to perform pixel-wise classification of quad-polarized images [126].

Although several research studies have adopted the CNN for the classification of different microwave images [126], there is a lack of research in precisely distinguishing the impacts of single and quad-polarized SAR GPR images on the feature extraction, model training speed, and accuracy level of the classifiers. In this chapter, two sets of the SAR GPR Data, i.e., single and quad-polarized SAR, are generated for three basic objects, such as boulder, cutter head tooth, and wrench [See Fig. 4.1]. The positive 2D images are formed by the TD-GBP technique (refer to Eq. 2.10) and white Gaussian noise is added to the reconstructed images. Then, a seven-layer CNN model is trained three times. Afterward, the trained models are tested with images attained by single and quad-polarized SAR systems, and the feature properties, accuracy, and speed of the model training are explored. Finally, the trained models are validated by the experimental data.

It is shown that the models whose train and test data are from the same groups learn faster than the models whose train and test data are from dif-

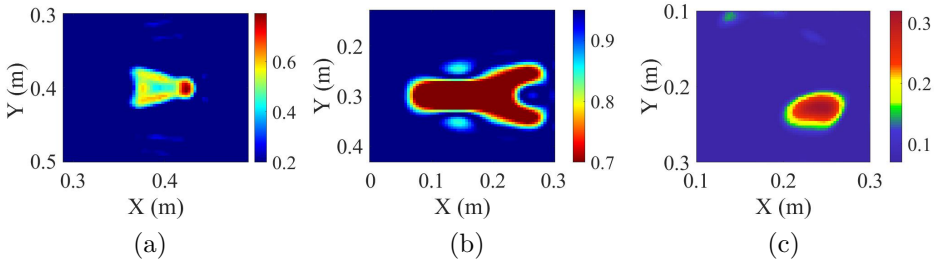

Figure 4.1: Examples of the RGB 2D positive images; a) cutter head tooth, b) wrench, and c) boulder.

ferent polarization groups. It is also observed that the images from quad-pole SAR represent some features that cannot be extracted from single-pole images. Furthermore, the classification accuracy is improved from 85.3% to 98.6% due to the feature extraction of the quad-pole images.

4.2 Methods

4.2.1 Generating Data set

To create a data set, the FDTD solver, GprMax [127], is used to generate SAR data. Three different shapes are considered for the classification. i) boulder: The boulders tend to be like a circle or oval shapes. ii) cutter head tooth: the 2D cross-section of the industrial cutter head teeth are mainly in a triangle shape. iii) wrench. Fig. 4.1 shows some examples of the boulder focused-images, cutter head teeth image, and one-headed and two-headed wrench images in gray scale.

A two-stage resampling technique is applied to create a large dataset.

- Space resampling: in this stage, the object's image is moved toward the edge of the image in the x- and/ or y-direction.
- Noise resampling: A Gaussian white noise with various means and variances is added to the reconstructed images with the mean value and variance given in 4.1-4.2.

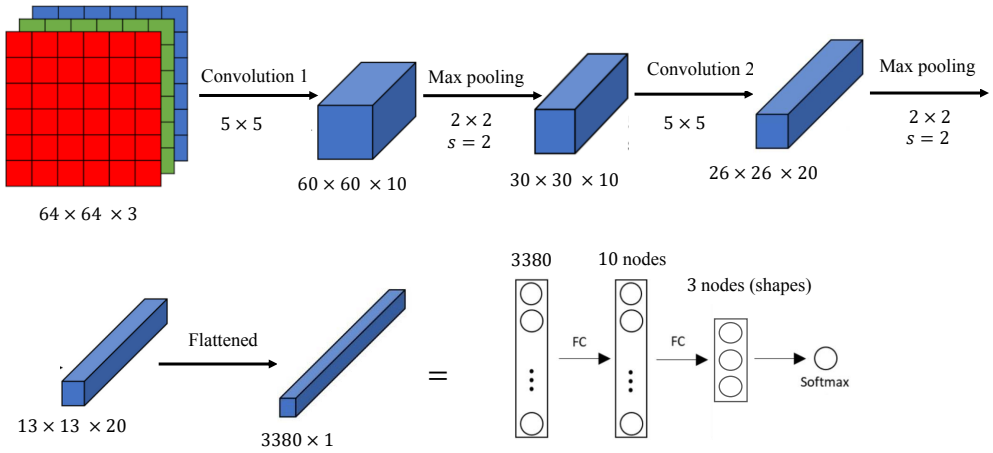

Figure 4.2: The architecture of deep convolutional neural network for GPR image classification.

$$mean = \pm 0.003, \pm 0.006 \tag{4.1}$$

$$var = 0.001, 0.0025, 0.005, 0.006 \tag{4.2}$$

The three-channel images have a dimension of 64 × 64 × 3 (i.e., RGB) with 64 pixels in both x- and y-direction. Finally, the data set is split into 70 and 30 percent for training and the validating model, respectively.

4.2.2 Neural Network Architecture

CNNs with different architectures typically consist of convolution layers, followed by pooling and fully connected layers [128], [129]. In this study, a deep neural network architecture is considered to examine the impacts of the polarization on the feature extraction and accuracy level of the classification since it has been designed for the general classification of images [125]. The proposed CNN, as shown in Fig. 4.2, includes two convolutional layers, two pooling layers, and three fully-connected layers. The filter size for the first convolutional layer is 5 and the number of filters is 10. The next layer is a max-pooling layer, which uses a 2×2 filter with a stride of 2. The next layer is a convolutional

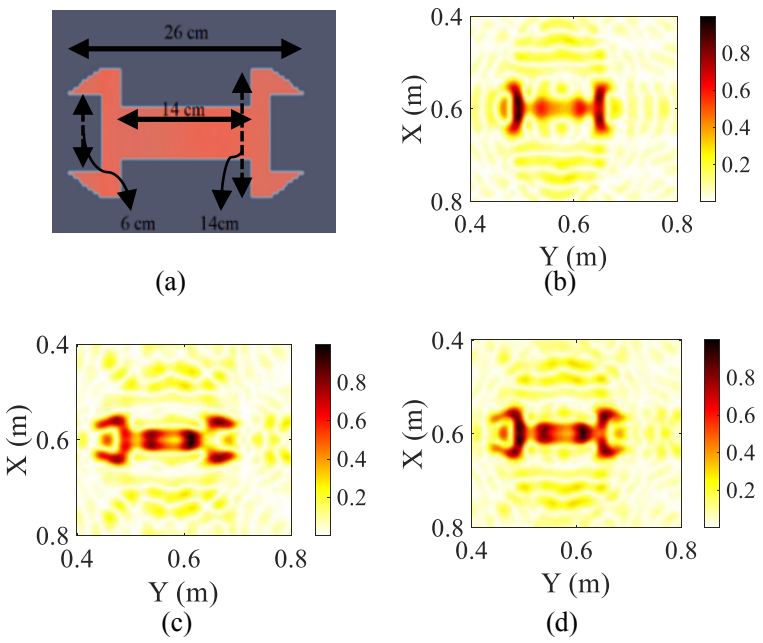

Figure 4.3: Illustration of the reconstructed image of single- and quad-pole SAR data; a) simulated asymmetric wrench, b) reconstructed image attained by horizontal polarization, c) reconstructed image attained by vertical polarization, and d) reconstructed image attained by quad-pole SAR.

layer consisting of 20 filters with a filter size of 5. Then, the same max pooling is applied to reduce the dimensions by half. A matrix flattener follows the max-pooling layer to obtain a 1-D matrix. Finally, softmax activation is used to determine the class of the object. The batch size is chosen to be 128 and the number of epochs is 20. Adam optimization is utilized to backpropagate the error for model training.

4.3 Simulation Results

4.3.1 Train and test data: single-pole SAR (Model 1)

For a non-symmetrical shape such as a wrench, a single vertical-pole SAR and a single horizontal-pole SAR data are used to attain the vertical and the horizontal features, respectively. Different one- and two-head wrenches, boulders, and cutter head teeth are simulated to train the model. For instance,

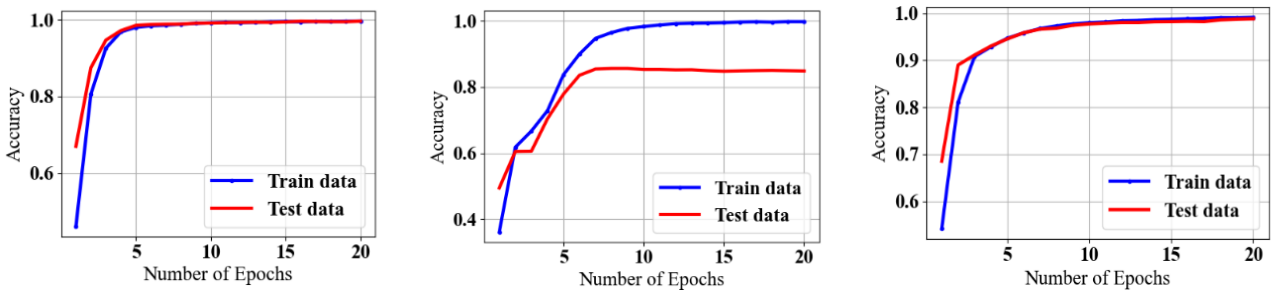

Figure 4.4: Accuracy vs. epoch; a) model 1, b) model 2, and c) model 3.

Fig. 4.3 shows the simulated two-head wrench and the reconstructed images by HH-polarization, VV-polarization, and quad polarization. For the sake of simplicity, the scattering matrix is considered as 4.3.

$$S = \begin{bmatrix} S_{hh} & 0 \\ 0 & S_{vv} \end{bmatrix} = \begin{bmatrix} 1 & 0 \\ 0 & 1 \end{bmatrix} \tag{4.3}$$

Inspecting the images in Fig. 4.3, the reconstructed images attained by the single-pole SAR fail to catch some essential parts of the object. However, the image of the quad-pole SAR depicts all features and edges of the object. The CNN model is trained by 7923 images from three classes and validated for 3396 images. The learning curve is illustrated in Fig. 4.4(a).

4.3.2 Train data: single-pole SAR, test data: quad-pole SAR (Model 2)

Inspection of the images in Fig. 4.3(b) and (d) may raise the concern that the single-pole SAR images might not depict some exclusive features compared to the quad-pole SAR images. To examine this assumption, CNN is trained only with single-pole SAR images and validated by quad-pole SAR images. The classification accuracy is shown in Fig. 4.4(b). As expected, the trained model is not successful in predicting classes since the training data (single-pole SAR images) fail to catch some of the test data features (quad-pole SAR images).

Table 4.1: Averaged accuracy of the trained models.

	Average accuracy		
Models	After 2 epochs	After 14 epochs	After 20 epochs
1	76.4%	99.4%	99.%
2	79.9%	84.8%	85.3%
3	73.3%	98.1%	98.6%

4.3.3 Train and test data: quad-pole SAR (Model 3)

In this section, the train and test data are determined to be quad-polarized SAR images. Compared to the single-pole SAR images, the quad-pole images are expected to have more features. The possibility of the training model with the same architecture, e.g., an equal number of features, an equal number of hidden layers, and neurons, is studied. The learning curve is plotted in Fig. 4.4(c).

The average accuracy after training two epochs, fourteen epochs, and all

		Predicted		
		Boulder	Tooth	Wrench
True	Boulder	864	40	0
	Tooth	0	889	0
	Wrench	0	0	902

Table 4.2: Confusion matrix of experimental data (model 1).

epochs are summarized in Table 4.1. Model 1 and 3, in which the train and data sets are from the same polarization groups, are trained much faster than model 2. Also, the final accuracy of the model 1 and 3 are close to 100%. However, model 2, trained with only reconstructed images of single-pole SAR, might not extract the whole features of the quad-pole SAR data. This is expected since the single-pole SAR data can not catch some details of the object, as discussed in III-A. This is also the reason for the significant discrepancy between the train (blue-colored) and test (red-colored) data curves in Fig. 4.4(b). By comparing row 1 and 3 of Table 1, we observe a higher accuracy of

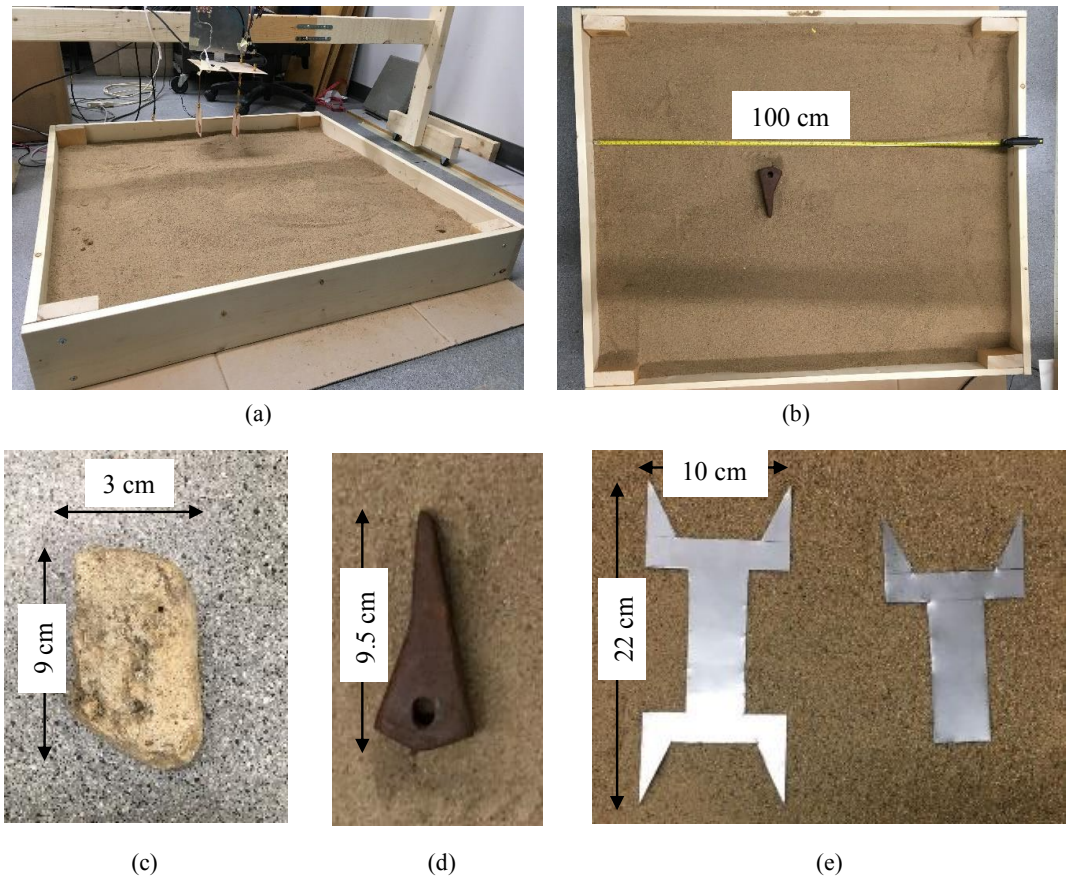

(a) (b)

(c) (d) (e)

Figure 4.5: Experiment details; a) perspective view of the setup, b) top view, c) boulder, d) cutter head tooth, and e) metal shapes representing two-headed and one-headed wrench.

model 1 compared to model 3 since the proposed architecture tends to extract all the essential features of the single-pole reconstructed images, whereas it is not picking all the features for the quad-pole reconstructed images.

4.4 Experimental Validation

Several SAR imaging experiments are conducted to verify the impacts of polarization on the feature extraction of the reconstructed images. Fig. 4.5(c)-(e) demonstrate boulder, cutter head tooth, and simplified metal shapes representing wrench used to achieve 2D images. The data were collected in xy-plane with a total aperture length of 24 cm in each direction. The transmitting

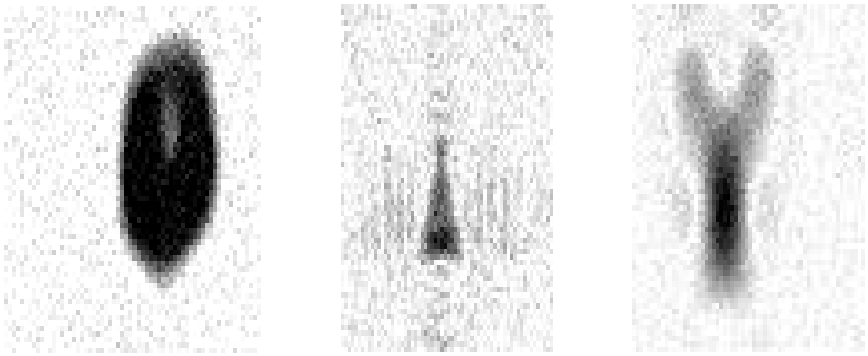

Figure 4.6: Experimental reconstructed image; a) boulder, b) cutter head tooth, and c) one-headed wrench.

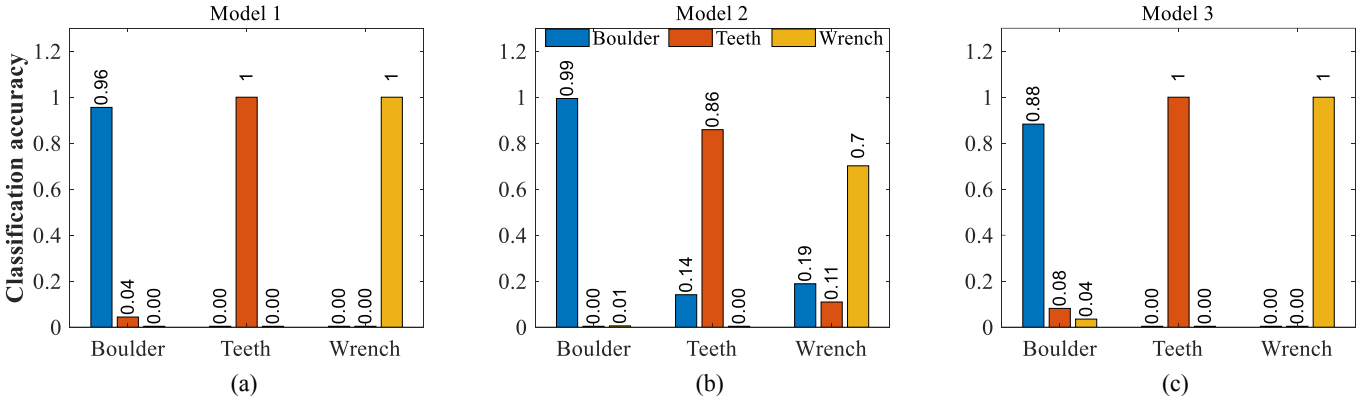

Figure 4.7: Classification accuracy vs. three types of shapes (classes); a) model 1. b) model 2, and c) model 3.

and the receiving antennas are pointed to the imaging scene in a quasi-monostatic configuration. The three aforementioned models are validated by the experimental data and classification accuracy graphs are demonstrated in Fig. 4.7. Although the accuracy of the experimental data is slightly less than the simulation data, it is in complete agreement with the simulation data. The classification of the experimental data confirms that quad-pole images represent some exclusive features compared to single-pole images. Inspecting the measured results in Fig. 4.7(b), and (c), 14% and 30% accuracy enhancements are reported for cutter head tooth and wrench classification due to providing the sufficient feature of the quad-pole images. For more insight of the dis-

cussed aforementioned models, the confusion matrix of the experimental data is presented in Tables 4.2, 4.3, and 4.4. Looking at Table 4.3 implies that wrench images are mislabeled with boulder and tooth since the test data is from quad-pole SAR images. Please note that in model 3, the classification accuracy of the cutter head tooth and wrench is much higher compared to the boulder's classification accuracy. This is due to the distinct feature of the quad-pole images of tooth and wrench, i.e., several sharp edges that have been picked up by CNN while the model is trained.

		Predicted		
		Boulder	Tooth	Wrench
True	Boulder	874	0	5
	Tooth	130	791	0
	Wrench	169	98	628

Table 4.3: Confusion matrix of experimental data (model 2).

		Predicted		
		Boulder	Tooth	Wrench
True	Boulder	778	72	31
	Tooth	0	991	0
	Wrench	0	0	895

Table 4.4: Confusion matrix of experimental data (model 3).

4.5 Conclusion

In this chapter, a deep learning neural network is presented to classify the three types of the buried object, including some asymmetrical objects. It is shown that the single- and quad-pole SAR data result in different reconstructed images accompanied by various distinct features. The impacts of single- and quad-pole SAR on the feature extraction, speed of the model training, and model accuracy is studied. Moreover, it has been shown that the model trains

faster if the train and test images are from the same polarization groups. Also, the prediction accuracy is higher when the train and test sets are from the same polarization groups. This study suggests that when a classification of quad-pole SAR images is needed, it is necessary to train the model with quad-pole SAR rather than the single-pole SAR images. In other words, the classification accuracy of the simulated data improves from 85.3% to 98.6% by reclaiming the missing features of the quad-pole images. According to the experimental data, the classification accuracy of the cutter head tooth and wrench are enhanced from 86.0% to 100% and 70.0% to 100%, respectively, by providing the suitable extracted features and classifier.

Chapter 5

Tunnel Forehead Imaging

5.1 Introduction

Numerous tunnel boring (TB) operations are currently underway globally, and in many cases, sizeable boulders or obstructive pipes are frequently encountered within the tunnel face. Thus, the availability of a predictive mechanism for the tunnel forehead would be of immense value to both operators and Tunnel Boring Machines (TBMs). Various methodologies have been explored in literature to address this challenge, including probe drilling and elastic wave reflection techniques [130]. Additional geological probing strategies considered encompass techniques like acoustic holography and ground-penetrating radar (GPR) [131]. For instance, Y. Park et al. [132] employed an impulse Ground Penetrating Radar (GPR) to visualize metal and concrete pipes within tunnel soil. However, this approach yields a limited spatial resolution due to the relatively wide pipe spacing of over 1 meter.

In another study [133], a multistatic GPR was developed to yield a three-dimensional depiction of buried objects and pipes, exhibiting promising imaging outcomes even in the presence of considerable surface clutter atop sand. Nonetheless, a significant drawback is the extensive long data acquisition time, approximately 14 hours, causing it less suited for real-time TB operations.

A comprehensive exploration of acoustic probing's capabilities for TBM

monitoring is presented in [134], where a passive seismic approach is adopted to visualize the tunnel's ahead vicinity. While this approach is sensitive to acoustic impedance variations, its typical resolution lies in the range of 10-15 meters. A distinct development, Sonic Softground Probing (SSP) [134], extends its probing reach to up to 40 meters ahead of the tunnel face. Yet, this technique suffers from extended analysis times, often spanning several days, and exhibits a limited spatial resolution of 0.5-1 meter. Consequently, these methodologies lack the appeal for widespread utilization within industrial TBMs. In the case of the passive approach, the TBM can face a large object, and the cutter head of the TBM can be damaged. The passive TBM also causes some delays in delivering the projects.

In this chapter, the possibility of the UWB SAR technique for the forehead imaging of the tunnel face is investigated through FDTD simulations. The microwave imaging system has several advantages: it is portable, cost-effective, and provides images with a satisfactory resolution.

The idea of MSI for TBM was previously presented in the literature [135], [136]; however, it was limited to physically-large object identification. Specifically, only three sensors per arm/wheel have been used and the target dimension is $4 \times 1 \times 0.5\ m^3$. In this chapter, a microwave sensor array is proposed to image small objects as well as large objects that may exist at the tunnel face. The data acquisition process in the proposed technique aligns with the rotational speed of the TBM wheel, ensuring fast and synchronized measurements. The achievable resolution is in the range of a few centimeters, significantly enhancing the precision of the reconstructed 3D images. Additionally, the subsequent data processing is efficiently completed within a timeframe of less than one minute, showcasing the method's capability for fast and streamlined analysis.

5.2 System Specification

As shown in Fig. 5.1, the sensors can be installed on the wheel, and it sends a train of the pulses toward the clay and receives the reflected signal. Then, the received signal is processed and the target scene image is reconstructed. This image can be used to set up some alarms for the operator or control center.

The excitation signal for all simulations is a second derivative Gaussian pulse with a pulsewidth of 282 ps and -10 dB-BW of $[0.36 - 1.87]$ GHz. For conducting simulations, the electrical properties of the tunnel face and possible buried objects are required to emulate the actual situation in the FDTD solver. The material of the excavated tunnel is found to be mostly clay, clay till, sandy clay, etc. [137]. The permittivity of the clay is dependent on the moisture level. For proof-of-concept, zero percent moisture clay is considered in the simulations. In [138], the dielectric constant of the clay for zero percent moisture level is:

$$\varepsilon = \varepsilon_0 \ (\varepsilon' - j\varepsilon'') = \varepsilon_0 \ (2.27 - j0.0341) \tag{5.1}$$

The dielectric constant of the water patch is in the range of 25-40. The boulder and water patch dielectric constants are considered to be 4 and 25, respectively. In addition, the calibration process is performed to remove the reflections from the air-sand interface using Eq. 2.9.

5.3 Mathematical Modality of the Image Reconstruction

Fig. 5.1(a) shows an example of the TBM face and the target area. The number of sensors per arm is considered N_s

$$P = [\rho_1, \ \rho_1, ..., \ \rho_{N_s}] \tag{5.2}$$

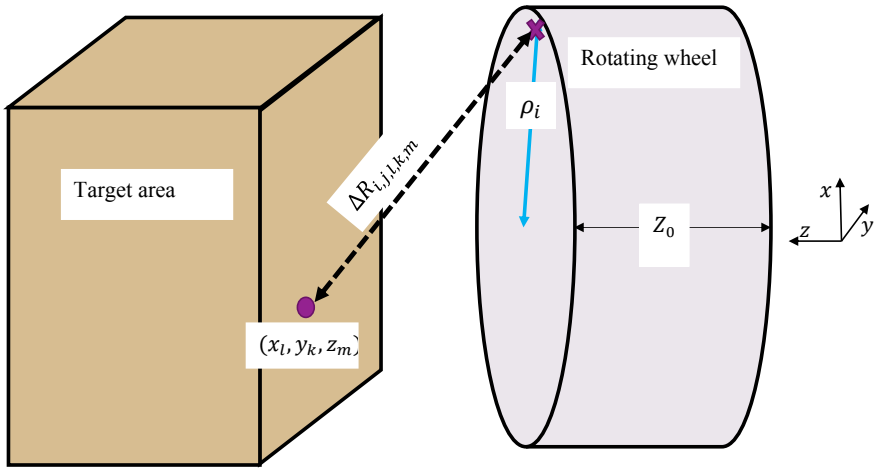

(a)

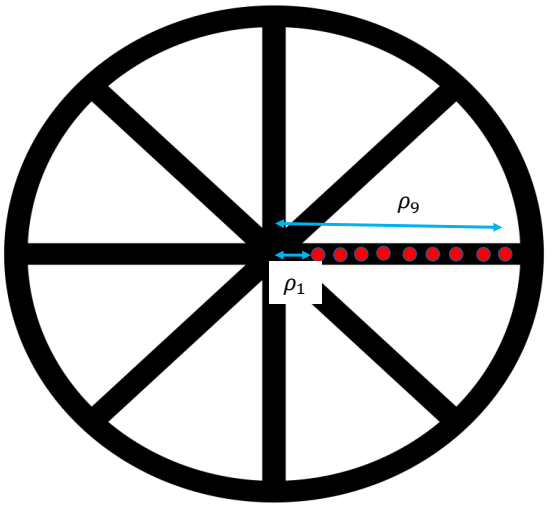

(b)

Figure 5.1: a) A schematic of the TBM wheel and the target area. b) Installed sensors on the rotating wheel.

The number of angles at which data are captured is considered to be N_{ang}

$$\Phi = [\varphi_1,\ \varphi_2, ...,\ \varphi_{N_{ang}}]. \tag{5.3}$$

Hence, the total number of apertures can be calculated as follows

$$N =\ N_{ang}\ \times N_s \tag{5.4}$$

Therefore, the captured data is a matrix with a dimension of $N \times M$, where N and M are the number of apertures and the number of sampled points of the received pulse, respectively. The target scene or the area of interest is discretized into L and K and M grids in the x, y, and z directions, respectively; hence the output image is an $L \times K \times M$ matrix. For each l, k, and m, the distance between the antenna and the target position can be calculated as:

$$\Delta R_{i,j,l,k,m} = \sqrt{(\rho_i Cos\varphi_j - x_l)^2 + (\rho_i Sin\varphi_j - y_k)^2 + (Z_0 - z_m)^2} \tag{5.5}$$

where (ρ_i, φ_j, Z_0) and (x_l, y_k, z_m) are the antenna aperture position and the corresponding position of the grid (l, k, m), respectively.

$$\Delta t_{i,j}(l,k,m) = \frac{2\Delta R_{i,j,l,k,m}\sqrt{\varepsilon_r}}{c} \tag{5.6}$$

where $\Delta t_{i,j}(l,k,m)$ is the time of flight between the grid (l,k,m) and the antenna position. Then, the image value is calculated as:

$$image(i,j,l,k,m) = s_{c,i,j}\Big(\Delta t_{i,j}(l,k,m)\Big) \tag{5.7}$$

$$Image(l,k) = \sum_{i=1}^{N_s}\sum_{j=1}^{N_{ang}} image(i,j,l,k,m) \tag{5.8}$$

where the $s_{c,i,j}$ is the calibrated data aperture that corresponds to ρ_i and φ_j.

5.4 Possible Sensors Arrangements

In this section, two different sensor arrangements are presented and corresponding simulations are conducted. First, a point target is placed in the center of the plane with a 22.5 cm distance from the rotating wheel. The sensors or antenna radii are:

$$P = [0.1, 0.19, 0.28, 0.37, 0.46, 0.55, 0.64, 0.73, 0.82] \tag{5.9}$$

The data is collected in 18 angles with a 20-degree increment to cover 360 degrees, hence: $N = \ 18 \ \times 9 = 162$. It should be noted that simulations are conducted in the space of $2 \times 2 \times 0.7 \ \ m^3$, and 10 Perfectly Matched Layers (PML) cells are set as absorbing boundaries.

Then, another simulation with the same specification is conducted with different sensors' arrangements:

$$P = [0.1, 0.25, 0.4, 0.5, 0.57, 0.64, 0.71, 0.77, 0.82] \tag{5.10}$$

These two sensor arrangements are illustrated in Figs. 5.2(a) and 5.4(a), respectively.

The target is a 5-cm diameter sphere at the location $(1, 1, 0.34)$. The reconstructed images $z = 36$ cm are shown in Figs. 5.3 and 5.5, respectively. The isosurfaces of the reconstructed images for equally distance sensors and non-equally distance sensors are illustrated in Figs. 5.2(b) and 5.4(b), respectively. As can be seen, in both cases, the sphere target images are reconstructed successfully in the correct position.

5.5 Resolution

Range and cross-range resolution is one of the most important aspects of any radar system. In this section, both resolutions with respect to the aforementioned pulse for the equally distanced sensor arrangement are investigated and

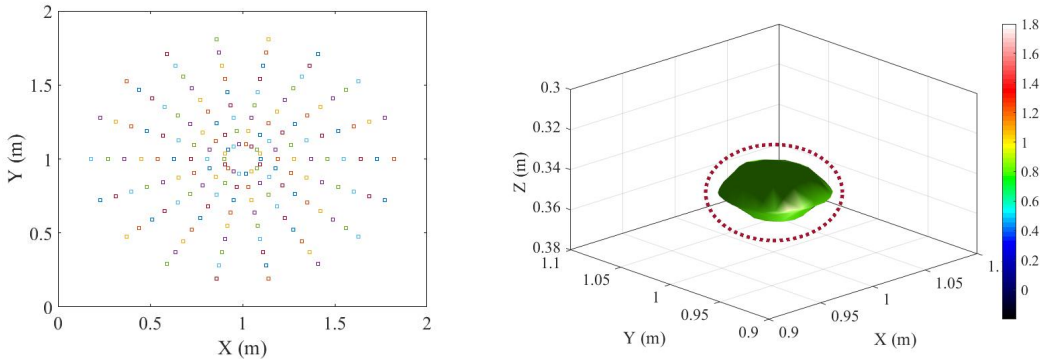

(a) (b)

Figure 5.2: a) Sensor arrangement (once one rotation of the wheel is completed). b) Isosurface of the reconstructed image.

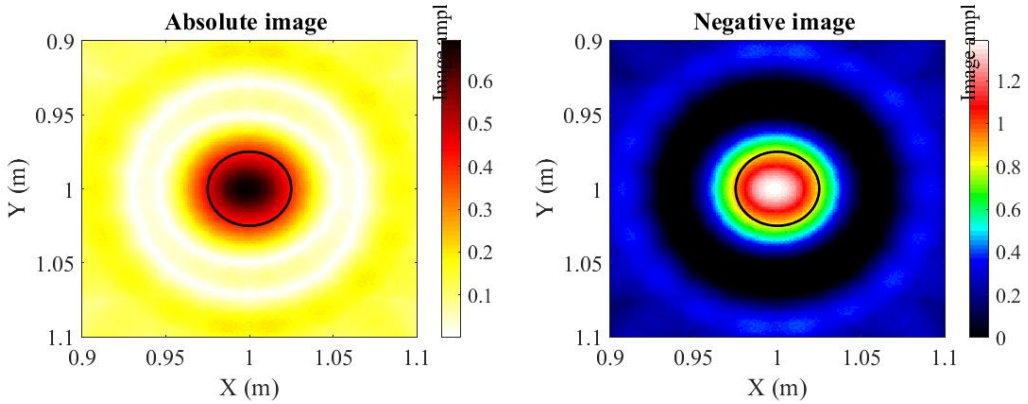

(a) (b)

Figure 5.3: Reconstructed image of the 5-cm sphere. a) Absolute image. b) Negative image.

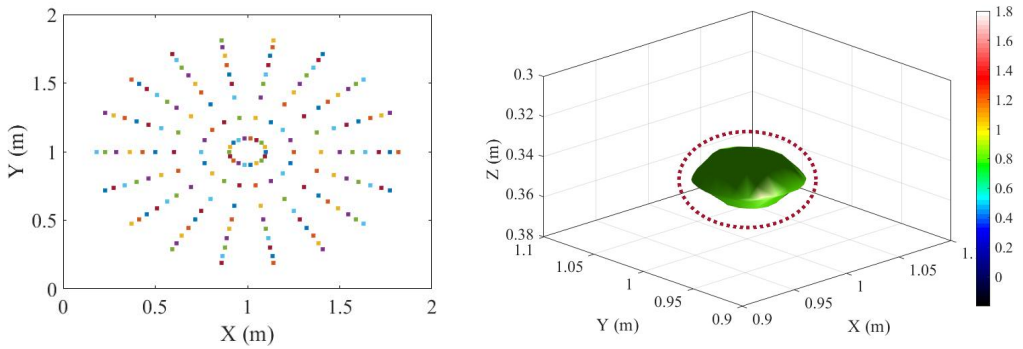

(a) (b)

Figure 5.4: a) Sensor arrangement. b) Isosurface of the reconstructed image.

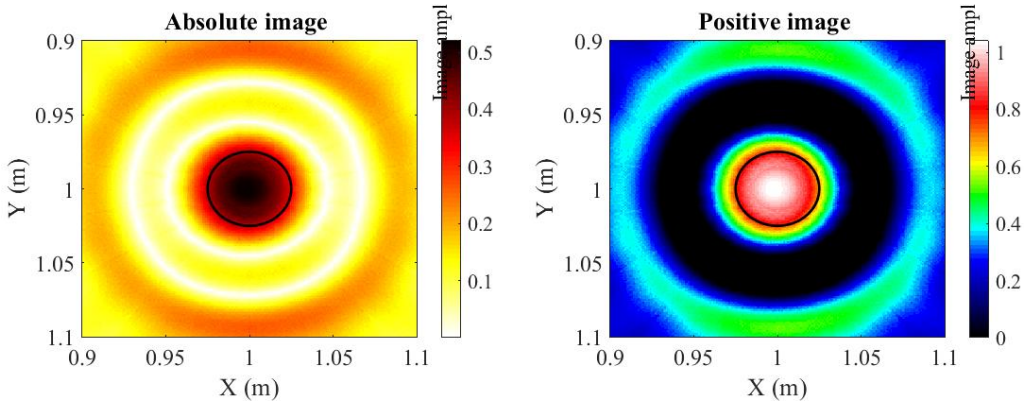

(a) (b)

Figure 5.5: Reconstructed image of the 5-cm sphere. a) Absolute image. b) Positive image.

presented. The expected range resolution is in agreement with the resolution achieved via simulations.

5.5.1 Range Resolution

The expected resolution in range direction can be calculated as follows:

$$\Delta_R = \frac{cX_{FWHM}}{2} = \frac{3 \times 10^8 \times 282 \times 10^{-12}}{2 \times \sqrt{(2.27)}} = 1.74\ cm \tag{5.11}$$

The targets are 5-mm radius spheres at locations $(1, 1, 0.34)$ and $(1, 1, 0.37)$, 2 cm distance. The reconstructed images at $z = 34\ cm$ and $z = 37\ cm$ are shown in Figs. 5.6(a) and 5.6(b), respectively. The isosurface image, which is

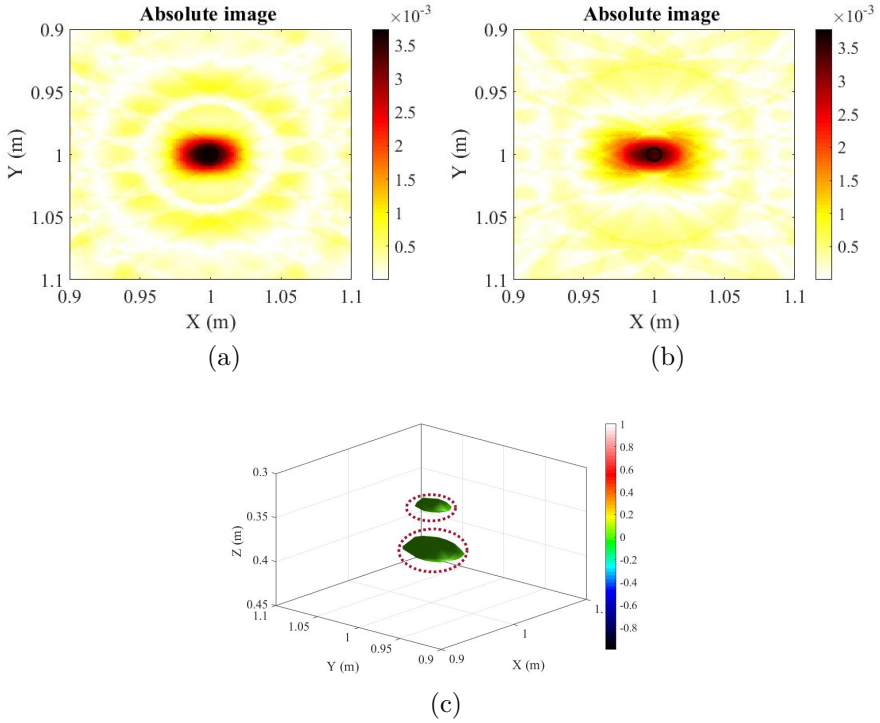

Figure 5.6: Range resolution. a) Absolute image $z = 34cm$. b) Absolute image $z = 37cm$. c) Isosurface image.

shown in 5.6(c), shows that the two targets are clearly resolved in the range direction.

5.5.2 Cross-range Resolution

The cross-range resolution is found to be 4.6 cm. The targets are a 5-mm radius spheres at locations $(1, 1, 0.34)$ and $(1.04, 1.04, 0.34)$, 4.6 cm distance. The reconstructed absolute and negative images $z = 34\ cm$ are shown in Fig. 5.7(a) and 5.7(b), respectively. The isosurface image, shown in 5.7(c), demonstrates the two targets are clearly resolved in the cross-range direction.

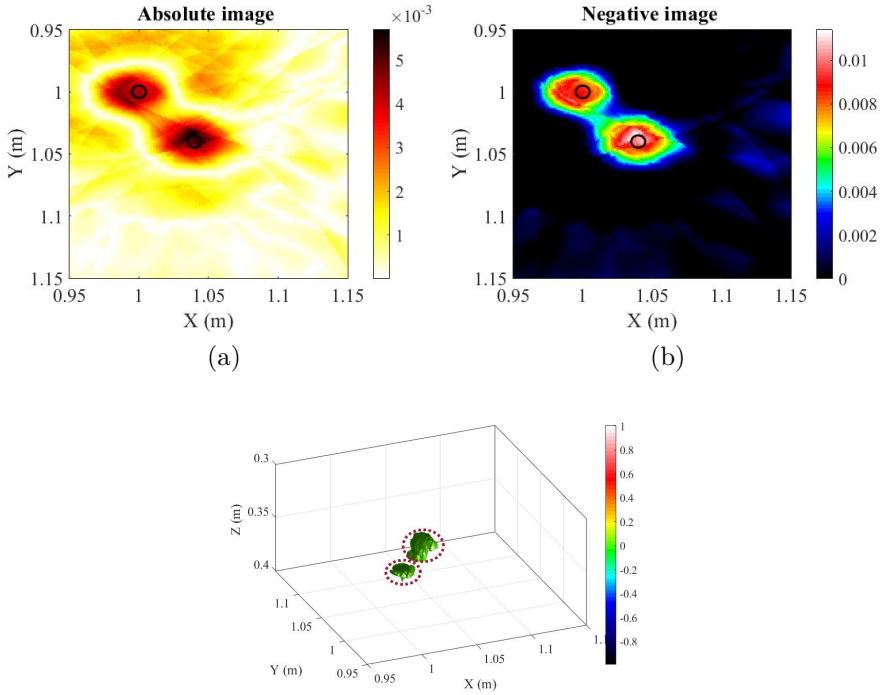

Figure 5.7: Cross-range resolution. a) Absolute image $z = 34cm$. b) Negative image $z = 34cm$. c) Isosurface image.

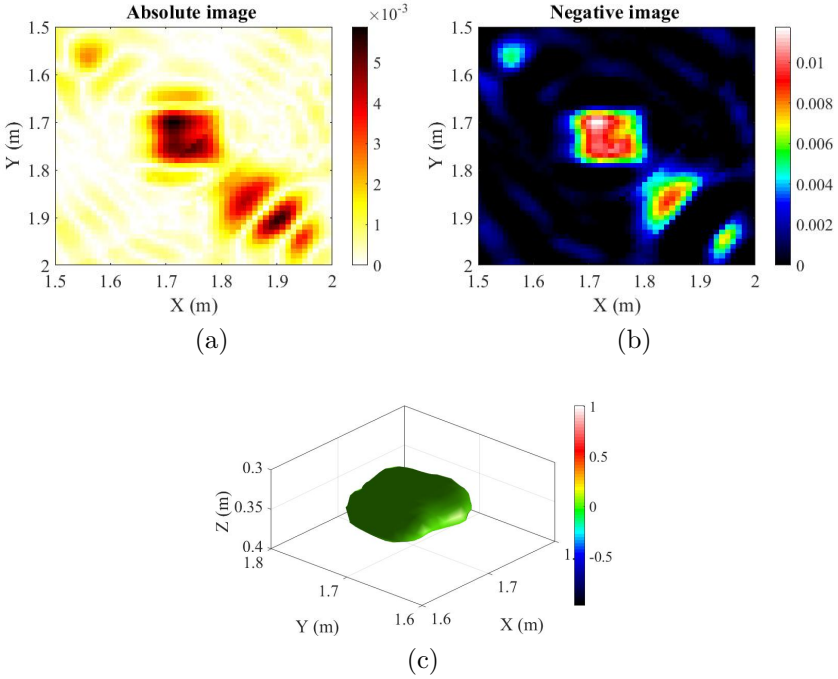

Figure 5.8: Marginal imaging scenario (equally spaced sensors). a) Absolute image $z = 36cm$. b) Negative image $z = 36cm$. c) Isosurface image.

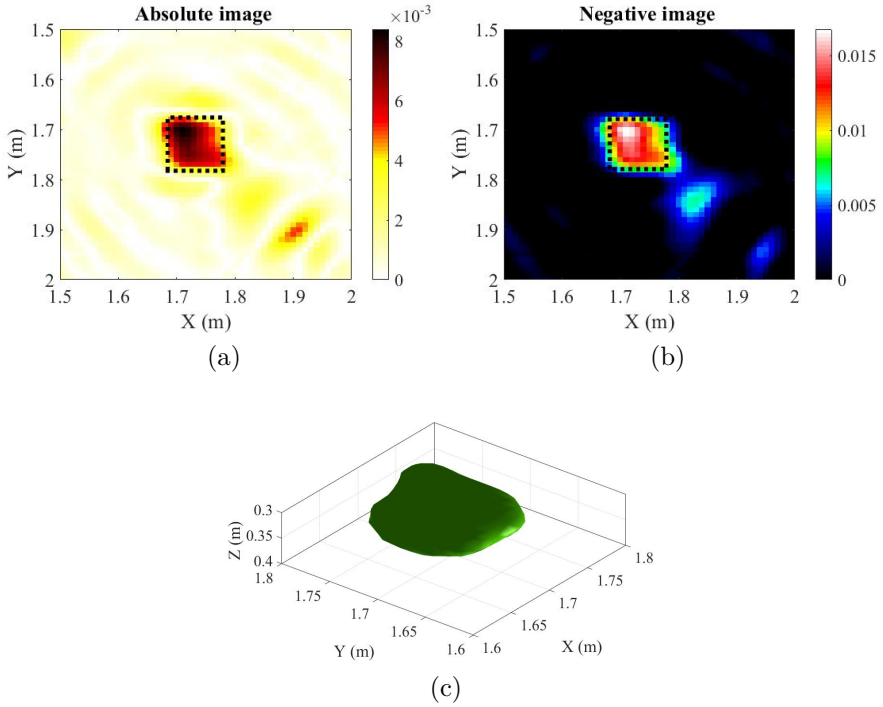

Figure 5.9: Marginal imaging scenario (non-equally spaced sensor). a) Absolute image $z = 36cm$. b) Negative image $z = 36cm$. c) Isosurface image.

5.6 Marginal Imaging

One of the major concerns is the greatest radius at which a target can be imaged. To examine the greatest radius for successful imaging, a boulder with a dimension of $10 \times 10 \times 4$ cm is placed in the location $(1.68, 1.68, 0.34)$. The data is collected in 72 angles with a 5-degree increment to cover 360 degrees ($N = 72 \times 9 = 648$). Two different aforementioned sensor arrangements are tested. Figs. 5.8(a) and 5.8(b) show the absolute and negative images for equal distance sensors, respectively. Figs. 5.9(a) and 5.9(b) show the absolute and negative images for non-equal distance sensors, respectively. The isosurface of the cubic boulder is also illustrated in Fig. 5.8(c) and 5.9(c). All reconstructed images and isosurface images show that the UWB-SAR technique can image the object at any radius up to the greatest radius of the sensors.

5.7 Realistic Scenario

In an actual TBM face, different types of objects, such as metal nails, boulders, and water patches may exist. Hence, a simulation including all these objects is conducted.

Four objects, including one metal nail, two boulders, and one water patch, are placed inside the clay. The metal nail is a cylinder with a 4 cm diameter and a height of 10 cm. The water patch shape is a sphere with a 6 cm diameter placed at $(0.6, 0.6, 0.5)$. The cubic boulders are $10 \times 10 \times 10$ cm and they are placed in location $(0.6, 1.4, 0.34)$ and $(1.4, 0.55, 0.34)$. The reconstructed negative images at $z = 36$ cm, $z = 45$ cm, $z = 49$ cm, and $z = 56$ cm are illustrated in Figs. 5.10(a), (b), (c), and (d), respectively. The isosurface of the reconstructed image is illustrated in Fig. 5.10(e). The processing time that includes calibration, image reconstruction, and image display is presented in Table 5.1.

Table 5.1: Processing time in seconds.

Number of Reconstructed Image's Grid	**Processing Time (s)**
$201 \times 201 \times 31 = 1252431$	14.99

5.8 Limitations

What are the limitations of this proposed forehead imaging?

1) The depth of investigation: As the pulse goes or penetrates toward the depth, it is attenuated. Hence, as the illumination depth increases, higher transmitted power is required. If there is enough transmitted power and no risk to human health, the investigated depth can be increased.

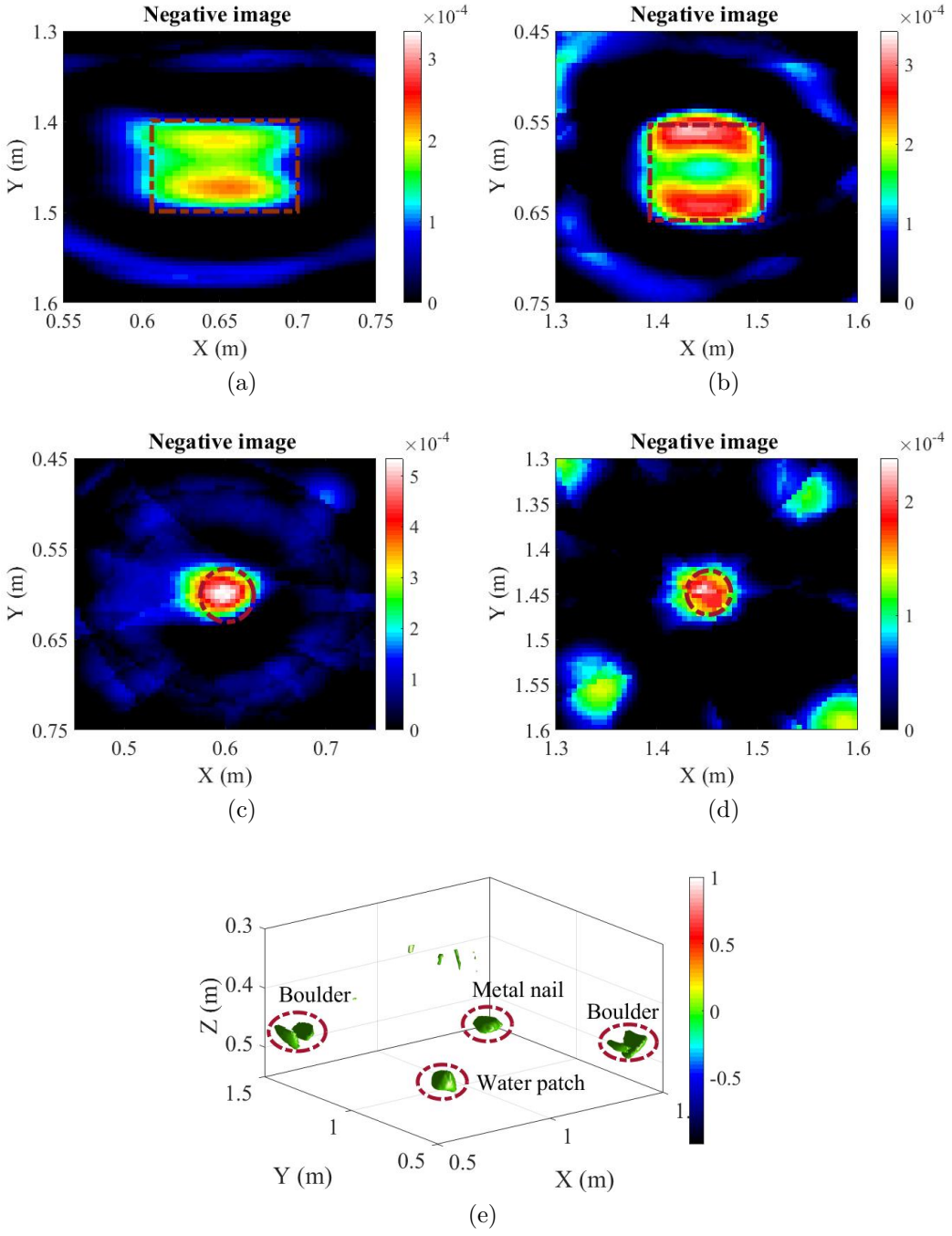

Figure 5.10: Realistic tunnel face scenario. a) Negative image $z = 36cm$. b) Negative image $z = 45cm$. c) Negative image $z = 49cm$. d) Negative image $z = 56cm$. e) Isosurface image.

2) Moisture level: As the level of water increases, the attenuation of the signal increases. Hence, this technique is limited to a low level of water or moisture content of the clay or sand.

3) Sensor installation: The average pressure on the TBM face is estimated to be 6000 psi [139]. In such harsh conditions, the specific antenna or sensor needs to designed that bear this pressure without breaking or erosion.

5.9 Analysis of TBM Rotation in GPR SAR Data Collection

In this section, an in-depth exploration of the GPR SAR data collection time is presented. The fastest rotational speed of the TBM cutter head is 10 revolutions per minute (RPM) [140]. In other words, the maximum cutter head rotational speed is $\frac{1}{6}$ revolutions per second or 60 degree per second. The time of flight for a depth of 0.5 meters can be computed as follows:

$$\Delta T = \frac{2d}{c} = \frac{2d}{c_0/\sqrt{\varepsilon'}} = \frac{2 \times 0.5}{(3 \times 10^8)/\sqrt{2.27}} = 5.02\ ns \tag{5.12}$$

where d is the depth of the probe, c is the propagation speed in the Tunnel face, and c_0 is the speed of light in a vacuum. The GPR can use expansion factor architecture to reduce the cost of the GPR [141]. If an expansion factor of 100000 is considered, the total data acquisition time can be computed as:

$$T_{total} = 100000 \times 5.02n = 0.502\ ms = 5.02 \times 10^{-4} \tag{5.13}$$

Hence, the maximum angular rotation of the cutter head within this 0.502 ms timeframe is derived as:

$$\Delta\phi = 5.02 \times 10^{-4} \times 60^\circ \approx 0.03^\circ \tag{5.14}$$

Evidently, the maximum cutter head's rotation is found to be 0.03 degrees during GPR-SAR data collection, effectively characterizing the scenario as static.

5.10 Conclusion

This chapter primarily discusses the application of UWB GPR to detect and investigate small practical objects situated at the forefront of a tunnel. The exploration encompasses various sensor arrangements, including equally distanced and non-equal distanced sensors. The investigation also studies attainable range and cross-range resolutions, revealing the feasibility of achieving a range resolution of 1.74 cm and a cross-range resolution of 4.6 cm using a pulse width of 282 ps.

Additionally, the study extends to a more complex scenario involving four distinct small objects: two boulders, a metal nail, and a water patch. Through FDTD simulation and SAR processing, 3D images are successfully reconstructed, capturing these objects within their correct position and dimensions.

Originally, the intention was to physically implement the UWB radar onto an actual Tunnel Boring Machine (TBM) to examine the tunnel face in real-world conditions. Regrettably, practical constraints emerged, blocking the feasibility of securing an authentic tunnel construction site and relocating a high-frequency sampling oscilloscope. Consequently, the chapter concludes with simulation-based evidence as a satisfactory outcome.

Chapter 6

A Modified Kirchhoff Migration in Superluminal Propagation Region

Microwave imaging is a nondestructive technique to acquire information on inaccessible objects in the ground, behind the wall, etc [106]. The data acquisition can be performed either in the time-domain or the frequency-domain [43]. The raw data is then post-processed and converted to the spatial domain to form a focused image of the Region of Interest (ROI). The process of converting the raw time-space or frequency-space data to a 2D or 3D image is called migration [37].

In the literature, various migration techniques are available, which can be classified into i) Diffraction summation, (ii) Phase-shift migration, iii) Kirchhoff's migration, vi) Frequency-wavenumber (w-k) migration, and v) Back-projection based migration [37], [41], [142]. Diffraction summation is the most popular algorithm thanks to their easy implementation. However, it is not well-suited for high-quality imaging applications. This inaccuracy originates from the fact that these methods are not developed based on rigorous wave equations [41]. Kirchhoff's and frequency-wavenumber migration techniques are rooted in wave equations. The goal of Kirchhoff's migration is to find a solution to the scalar wave equation, and it exploits Kirchhoff's integral theorem [143].

Kirchhoff's migration technique can provide higher-quality images compared to diffraction summation. The frequency wave number is also derived from the scalar wave equation, and the image reconstruction is done in the spatial Fourier domain. Frequency wave number migration is a more computationally efficient method than other time-domain integral techniques, i.e., Kirchhoff's migration. However, the data acquisition must be in uniformly spaced transceiver positions, which may limit the usage of this technique [41]. The back-projection based migration techniques are developed on the tomographic principles. Unlike the frequency-wave number migration, the back-projection algorithm does not need an evenly-spaced data acquisition. Another advantage of this migration is that the image reconstruction can be started before the data capture is entirely completed, making this technique suitable for real-time applications. However, back-projection techniques migrate a single spike to an arc that causes the undesired sidelobe in the reconstructed image [144]. In ultra wideband (UWB) microwave imaging, the ROI is illuminated by a series of short pulses and the transient response is recorded. Then the space-time domain data are transformed into a 2D or 3D image by one of the aforementioned migration techniques. Kirchhoff's migration provides a focused image with significantly higher quality and is more computationally efficient. For these reasons, Kirchhoff's migration is one of the most popular focusing technique for UWB radar SAR imaging [39], [41].

In many practical applications, the target is in the antenna's near-field. Many researchers developed near-field migration techniques [145]–[149]. However, none of them has addressed the time-domain Kirchhoff's migration in the near region of the antenna. In [150], the propagation speed of the signal in the medium is considered to be constant. This approximation is not valid in the near-field and Fresnel region of the antenna [151], [152] and deteriorates the

reconstructed image created by Kirchhoff's migration.

In this chapter, a modified Kirchhoff's migration technique for the near-field region is proposed, and the non-uniformity of the pulse propagation speed is compensated. Then, the modified technique is validated through several simulations and experimental scenarios. The proposed modified Kirchhoff's migration is applied to Circular SAR (C-SAR) and Linear SAR (L-SAR) techniques, and the reconstructed images are compared to the conventional Kirchhoff's technique

6.1 Modified Kirchhoff's Migration Formulation

The scalar wave equation in a lossless medium can be written as

$$\Delta^2\Psi(\vec{r},t) - \frac{1}{{v_m}^2}\frac{\partial^2\Psi(\vec{r},t)}{\partial t^2} = -f(\vec{r},t) \tag{6.1}$$

where Ψ is the wave amplitude, v_m is the propagation velocity, and f is the source function of the wave evaluated at position $\vec{r}$ and time t. In a source-free ROI, i.e., $f(\vec{r},t) = 0$, Green's theorem can be applied to solve the Eq. 6.1.

$$\Psi(\vec{r},t) = -\frac{1}{4\pi}\int_0^\infty \int \left(\Psi\frac{\partial G}{\partial n'} - G\frac{\partial \Psi}{\partial n'}\right) dA'\, dt' \tag{6.2}$$

Eq. 6.2 is known as Kirchhoff's integral theorem, where n' and G are the unit normal vector to the surface and Green's function, respectively. In an isotropic medium

$$\frac{\partial G}{\partial n'} = 0 \tag{6.3}$$

It should be noted that the wave amplitude or Ψ can be acquired from the measurements. The solution to the above equation is [39]

$$\Psi(\vec{r},t) = \iint_V \Big(\frac{Cos\theta}{v_m\, r}\ \frac{\partial}{\partial t}\Psi(\vec{r},t\ -\frac{r}{v_m})\Big)\, d\phi\, d\rho \tag{6.4}$$

where θ is the angle of the incident wave to the propagation axis. i.e., z . $Cos\theta$ can be calculated as follows

$$Cos\theta = \frac{z - z_t}{r} \tag{6.5}$$

where (x_t, y_t, z_t) is the coordinates of the observation point. The above integral equation with N number of receiver positions can be approximated with the following

$$\Psi(\vec{r}, t) = \sum_{i=1}^{N} \Big(\frac{Cos\theta_i}{v_m \; r_i} \; \frac{\partial}{\partial t} \Psi(\vec{r}, t \; - \frac{r_i}{v_m}) \Big) \tag{6.6}$$

where r_i is the euclidean distance between the observation point and the receiver position.

To reconstruct the image of ROI, each point of the imaging area can be considered as a point scatterer and the goal is to retrieve the wave amplitude at the time the wavefront intersects that point. For all the receiver apertures, the above procedure is carried out and an image value is calculated for each observation point by aggregating the wave amplitudes.

As mentioned in Eq. 6.4, the propagation velocity of the wavefront is needed for the reconstruction. The group velocity is defined as

$$v_m = \frac{dw}{d\beta} \tag{6.7}$$

where w and β are the angular frequency and the wavenumber, respectively. In the far-field region of the antenna, the group velocity is equal to phase velocity and can be acquired as follows

$$v_m = v_{ph} = C = \frac{c_0}{\sqrt{\varepsilon_r}} \tag{6.8}$$

where C, c_0, and ε_r are the speed of the light in the medium, the speed of the light in the vacuum and the dielectric constant of the propagation medium, respectively. However, in the near-field region of the antenna, the group velocity

is not equal to C. In [145], [152], is shown that the pulse propagation speed is a function of the distance and angle in superluminal propagation region. To compensate for the variable propagation speed for Kirchhoff's Migration, the modified Kirchhoff's is proposed as

$$\Psi(\vec{r},t) = \iint_V \Big(\frac{Cos\theta}{v_m(\phi,\rho)\ r}\ \frac{\partial}{\partial t}\Psi(\vec{r}, t\ - \frac{r}{v_m(\phi,\rho)}) \Big)\, d\phi\, d\rho \tag{6.9}$$

where the propagation velocity i.e., v_m is a function of the observation point. This is extra essential for any near-field microwave imaging since the pulse propagation speed can escalate up to 6 times for a 6-GHz dipole antenna as we move from the far-field region to a few centimeters [145]. In order to verify the proposed modified Kirchhoff's migration, the discrete version of the Eq. 6.9 is presented as follows

$$\Psi(\vec{r},t) = \sum_{i=1}^{N} \Big(\frac{Cos\theta_i}{v_m(\phi,\rho)\ r_i}\ \frac{\partial}{\partial t}\Psi(\vec{r}, t\ - \frac{r_i}{v_m(\phi,\rho)}) \Big) \tag{6.10}$$

Note that v_m should be measured beforehand and it varies for different antenna. In this work, miniaturized Vivaldi antennas are used as transceiver and the pulse propagation velocity as a function of distance and angle i.e., $v_m(\phi,\rho)$ are employed to reconstruct the image. Fig. 6.1 illustrated the measured velocity (i.e., v_m) profile of the miniaturized Vivaldi antennas transceiver.

6.2 Simulation Validation

In order to verify to proposed modified Kirchhoff migration, several imaging scenarios are conducted in near-filed region of the antenna. In all cases, the reconstructed images by conventional and modified Kirchhoff migration technique are presented side by side. The SAR technique is exploited to sample the wave amplitudes in spatial domain. To mitigate the effect of surrounding

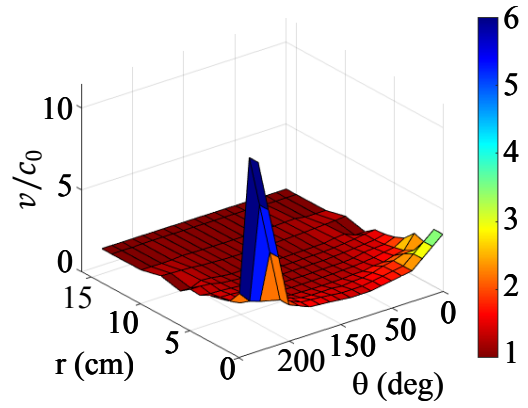

Figure 6.1: Propagation velocity in the near-field region.

objects, the calibration procedure is done as follows

$$s_{cal,i} = s_{raw,i} - s_{am,i}, \qquad i = 1, 2, ..., N \tag{6.11}$$

where $s_{cal,i}$, $s_{raw,i}$, and $s_{am,i}$ are the calibrated signal, the raw signal, and the ambient signal of aperture i, respectively. Two sets of experiments are conducted, including C-SAR and L-SAR configurations. Note that all the images are presented in a log scale to improve illustration and highlight the distinction of the targets with respect to the background.

6.2.1 Modified Kirchhoff Migration for the C-SAR Near-Field Imaging

The simulation setup is a three-point target scenario as shown in Fig. 6.2(a). The maximum distances between the three targets are 2.83, 2.83, and 4 cm. The data are collected in a circular fashion in 18 different apertures, as it it is marked with green plus markers on Fig. 6.2(a). The calibrated signal along the apertures is illustrated in Fig. 6.2(b). The focused images using conventional and modified Kirchhoff algorithm are shown in Fig. 6.2(c), and Fig. 6.2(d), respectively. Both images are normalized and the same color map is used for the comparison purpose. As seen, the conventional Kirchhoff migration is not

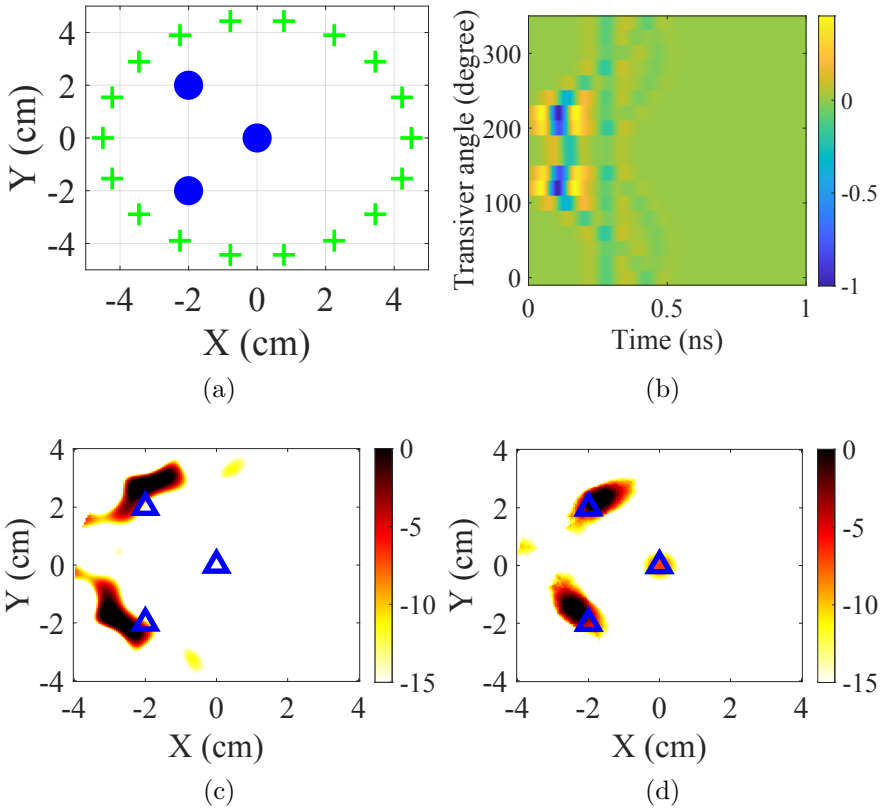

Figure 6.2: C-SAR simulation scenario; a) b) reconstructed image by conventional Kirchhoff's migration, c) reconstructed image by the proposed Kirchhoff's technique.

successful to focus the image of left targets due to non-uniform speed velocity of the propagation. However, the proposed modified Kirchhoff's is able to focus the left point targets since the variable speed profile compensates for the near-field region non-linearity.

6.3 Experimental Validation

In all conducted experiments, miniaturized Vivaldi antennas were employed as the radar transmitter and receiver, exhibiting a gain of 5-8 dBi across the frequency range of 3.2-15 GHz. This antenna is characterized and the propagation velocity as a function of distance and angle is illustrated in Fig.

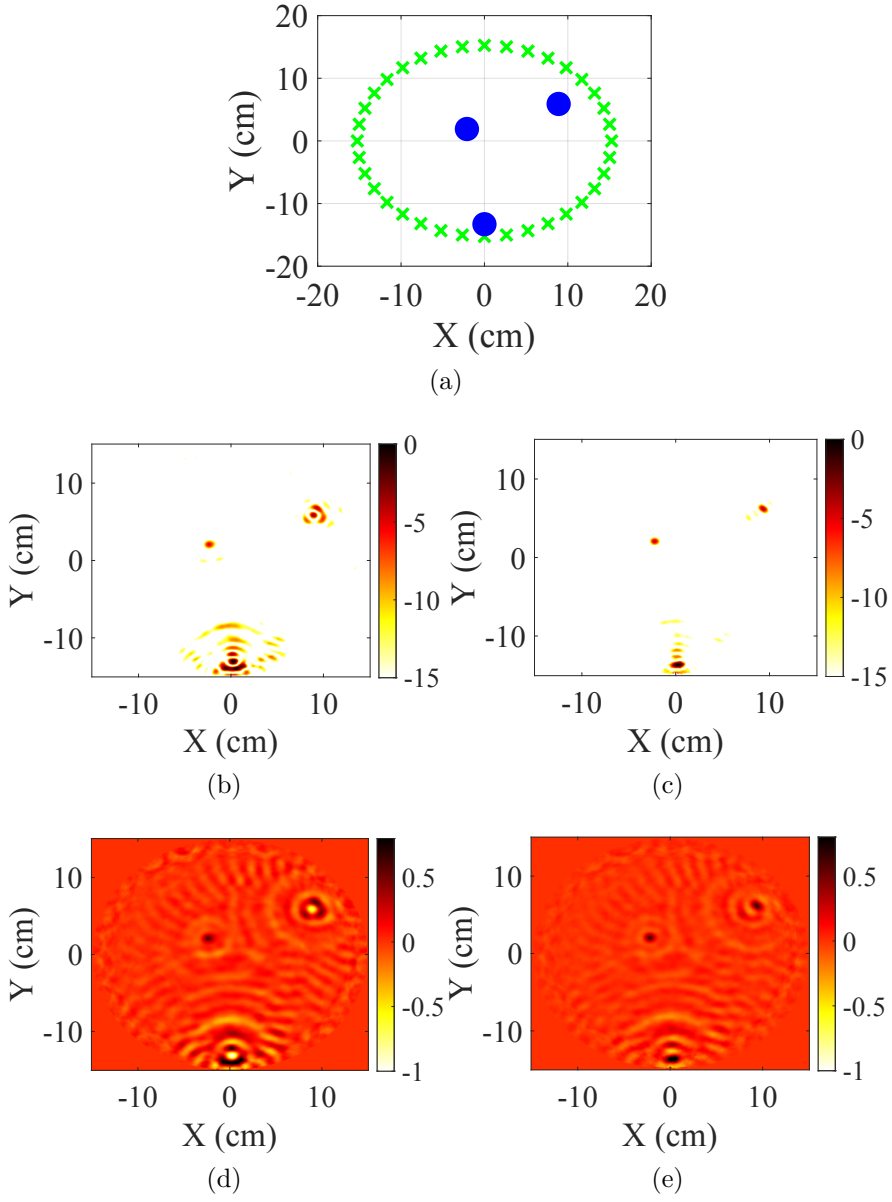

Figure 6.3: a) C-SAR experiment setup. Reconstructed positive image by b) conventional Kirchhoff's migration, c) proposed Kirchhoff's technique. d) Reconstructed real image by conventional Kirchhoff's migration, and e) proposed Kirchhoff's technique.

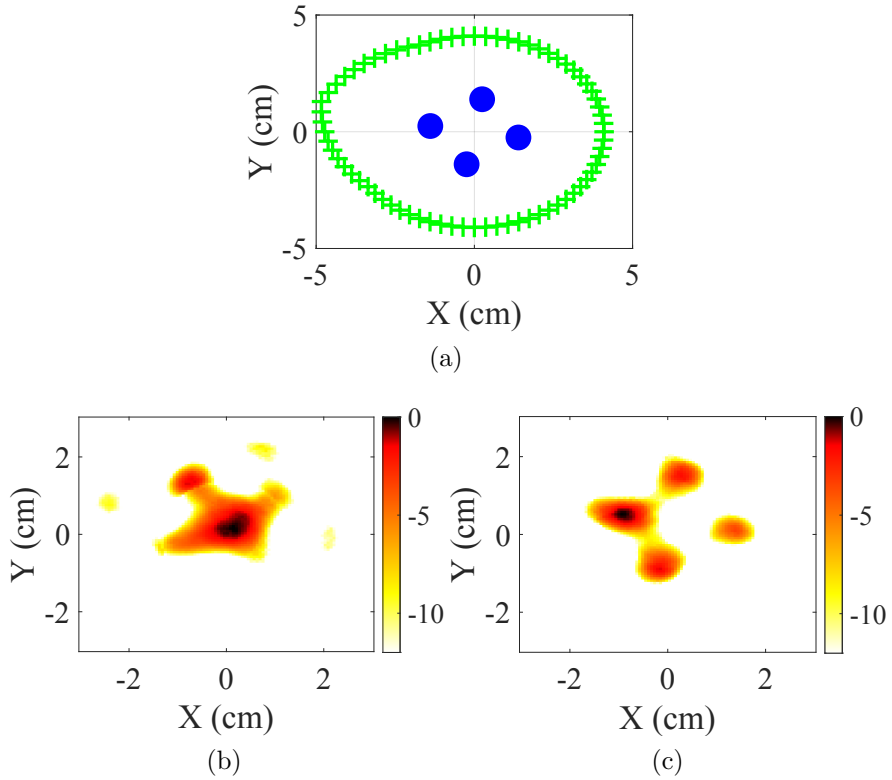

Figure 6.4: C-SAR Experiment with four nails. a) Experiment setup. b) Reconstructed image by conventional Kirchhoff's migration. c) Reconstructed image by the proposed Kirchhoff's technique.

6.1, as it was mentioned earlier. The distance between the transmitter and receiver is 1 cm. The excitation signal is a first derivative Gaussian pulse with a full width at half maximum (FWHM) of 48 ps. This pulse is generated by AVTECH AVP-3SA-C with a chain of 10-V steps and a pulse repetition frequency (PRF) of 1 MHz. The receiver antenna is connected to the high frequency sampling oscilloscope. To increase the the received signal SNR, a 64-time averaging is performed in the sampling oscilloscope. The number of data points is 4050. The recorded data are then interpolated to 10000 data point. In addition, a moving average filter is applied to reduce the measurement noise.

6.3.1 Experiment 1, Circular SAR Near-Field Imaging

First, a three-target C-SAR scenario experiment is conducted. Three metal nails with a height of 15 cm and radius of 3.75 mm are adhered to a rotating wooden board. The transceiver radius is 2 cm and the data is collected in 36 positions with an increment of 10^0. The reconstructed positive and real images by the conventional Kirchhoff migration and the modified Kirchhoff migration are illustrated in Fig. 6.3 (b)-(e). All the images are normalized and shown into a same scale for the purpose of comparison. By comparing Fig. 6.3(b) and 6.3(a), it is observed that the conventional Kirchhoff's algorithm represent each point target as multiple point targets, particularly the middle bottom target. While the proposed modified Kirchhoff's technique successfully maps the spatial-time data into one single focused point targets with true positions.

6.3.2 Experiment 2, Circular SAR Near-Field Imaging

The second experiment is a four-target scenario which is emulated by gluing four metal nails in a tilted square shape, as shown in Fig. 6.4(a). The square side is 2 cm and the transceiver radius is 5 cm. The total number of aperture is 36 with a 10^0 increment to cover 360^0.

The spatial-time domain collected data is exploited to focus 2D image by conventional and proposed modified Kirchhoff's migration technique. The reconstructed conventional image using c_0 is shown in Fig. 6.4(b), and the reconstructed image using the pulse-peak velocity is shown in Fig. 6.4(c). The reconstructed image using the characteristic speeds clearly focuses four targets; whereas, in the conventional Kirchhoff image, the four targets are completely merged together.

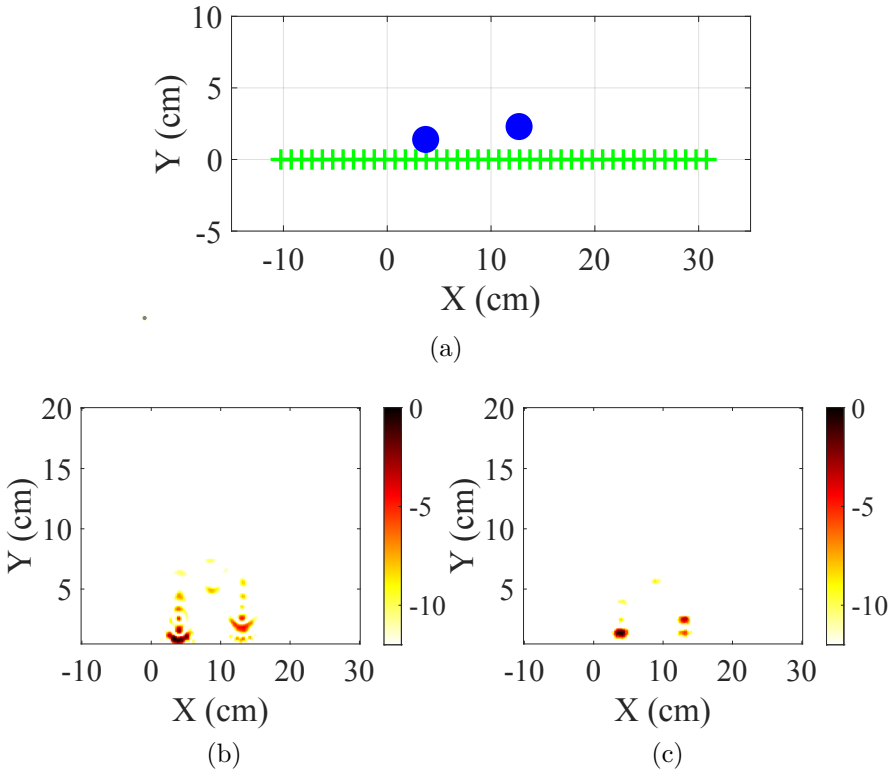

Figure 6.5: Linear SAR Experiment. a) Experimental setup. b) Reconstructed image by conventional Kirchhoff's migration, c) reconstructed image by the proposed Kirchhoff's technique.

6.3.3 Experiment 3, Linear SAR Near-Field Imaging

In this subsection, the L-SAR configuration are used to collect data, where the antenna apertures are aligned in a line. The total aperture length is 41 cm with a spacing of 1 cm, as illustrated in Fig. 6.5(a). The targets are two metal pins which are glued to a wooden board with the Cartesian coordinates of $(3.7, 1.4)$ cm and $(12.7, 2.3)$ cm , as shown with blue dots in Fig. 6.5(a). The reconstructed image using conventional Kirchhoff and the one using proposed modified Kirchhoff are shown in Fig. 6.5(b) and 6.5(c), respectively. As can be seen, the conventional Kirchhoff's migration image fails to focus the target, particularly the left nail which is very close to the antenna transceiver and the propagation speed is more deviated from c_0. The modified Kirchhoff's technique, which takes into account the variable propagation speed, focuses

the targets with correct positions.

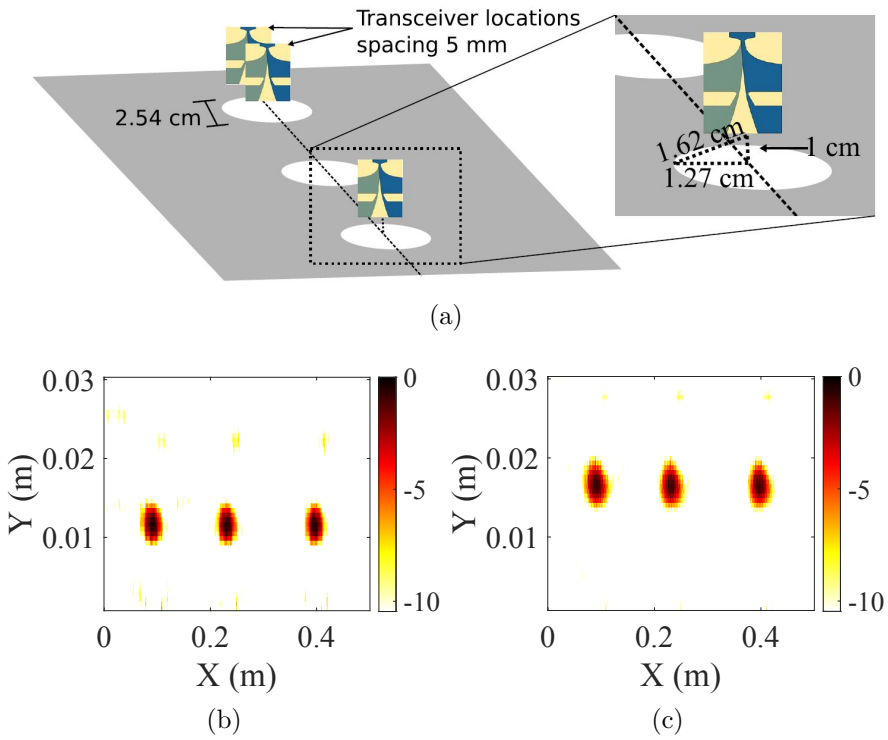

Figure 6.6: Linear SAR Experiment. a) Experimental setup. b) Reconstructed image by conventional Kirchhoff's migration, c) reconstructed image by the proposed Kirchhoff's technique.

6.3.4 Experiment 4, Linear SAR Near-Field Imaging

The last experiment is conducted to emulate UWB SAR technology for oil well perforation [106]. The transceiver configuration is monostatic, with a spacing of 0.5 *cm* between the Tx and Rx antenna. Three holes with radius of 1.27 *cm* are cut from a metal sheet. Then, the metal sheet is placed in a distance of 1 *cm* below the transceiver. The total antenna aperture length is 50 *cm*, with 1 *cm* distance between each aperture. The experiment setup detail is illustrated in Fig. 6.6(a). The target is in the near-field of the miniaturized Vivaldi antenna. The conventional modified Kirchhoff's migration is applied to reconstruct the ROI. Then a threshold of 0.6 is applied and the image is shown

in Fig 6.6(b). Then the space-time domain data is the fed to the proposed modified Kirchhoff's and the same threshold is applied. The final image is illustrated in Fig. 6.6(c). The modified Kirchhoff's migration technique focuses the three holes in the true position, however, the conventional Kirchhoff's technique focuses the targets in wrong positions.

6.4 Conclusion

This chapter presents a novel focusing algorithm based on Kirchhoff's migration technique to compensate for the superluminal group velocity in the near-field region of the antenna. The proposed modified Kirchhoff migration is applied to various scenarios, including C-SAR and L-SAR. First, a C-SAR data acquisition is generated in the simulator, and the image is reconstructed using different target scenarios, and the image of the ROI is reconstructed using the conventional Kirchhoff and the proposed modified Kirchhoff's migration. It is shown that the conventional Kirchhoff's migration fails to focus the energy on at least one target among all the experiments. In L-SAR experiments, the modified Kirchhoff algorithm generates the image with the correct position and dimension, whereas in the image reconstructed by conventional Kirchhoff, the position of the targets is not matched to the true location. The proposed algorithm can be effectively used for near-field radar imaging.

Chapter 7

Conclusions and Further Direction

7.1 Conclusion

This thesis explores the versatility of Ultra-Wideband (UWB) radar technology in solving industry challenges. Firstly, it addresses issues in the oil sector by proposing microwave imaging and signal processing techniques for multiphase flow monitoring in pipes, achieving high-resolution cross-sectional images for flow rate estimation. It also introduces methods to enhance target detectability and improve stratified flow imaging. Secondly, it investigates the applicability of UWB radar in probing tunnel faces for buried objects or obstacles, characterizing buried objects' electrical properties and demonstrating UWB radar's capability for online geological condition assessment during tunnel construction. Furthermore, it delves into automating ground-penetrating radar (GPR) and tunnel boring machines (TBM) by classifying reconstructed images of buried objects using deep learning. Lastly, a modified Kirchhoff's migration technique is presented to address non-uniform pulse propagation in the near-field region of UWB radar transceivers. This research broadens the potential applications of UWB SAR technology and signal processing methods, particularly in tunnel construction and multiphase flow monitoring.

7.2 Future Direction

7.2.1 UWB radar sensor for unbalanced multiphase flow metering

The UWB radar can provide a high-resolution image of the crude oil pipe; however, in the process of individual phase calculation, the velocity of each phase is assumed to be known. The next step of the proposed technique involves integrating a Doppler meter into the UWB radar and installing it on an actual crude oil pipe to evaluate the flow rates of crude oil, water, and natural gas.

7.2.2 UWB radar for industrial tunnel boring machines

The UWB radar has demonstrated its capability to generate images of the tunnel face and extract dielectric properties of tunnel face materials in a laboratory environment. However, for practical application, it is essential to mount the UWB radar system onto an actual Tunnel Boring Machine (TBM) and transmit short pulses toward the real tunnel face. Subsequently, by processing the back-scattered signals from real-world cases, material characterization and high-resolution imaging can be achieved. The author emphasizes that additional post-processing steps, including clutter reduction and noise filtering, will be necessary as the real tunnel face is not a homogeneous medium.

7.2.3 Modified Kirchhoff's technique in superluminal region for multi-layered medium

The proposed Kirchhoff algorithm is based on the assumption that the pulse propagates through a single medium with a constant ε'. However, in numerous practical Ground-Penetrating Radar (GPR) scenarios, the pulse travels through both air and sand, creating a multi-layered near-field region. In such instances, it is essential to assess the UWB antenna and derive the pulse's

propagation speed profile, considering both distance and angle as variables. Consequently, it becomes necessary to develop a modified Kirchhoff algorithm, complete with mathematical formulation, to effectively focus the GPR image in this complex multi-layered near-field environment.

References

[1] G. Breed, "A summary of fcc rules for ultra wideband communications," *High Frequency Electronics*, vol. 4, no. 1, pp. 42–44, 2005.

[2] Z. Sahinoglu, S. Gezici, and I. Güvenc, *Ultra-wideband positioning systems: theoretical limits, ranging algorithms, and protocols*. Cambridge university press, 2008.

[3] K. Tomiyasu, "Tutorial review of synthetic-aperture radar (sar) with applications to imaging of the ocean surface," *Proceedings of the IEEE*, vol. 66, no. 5, pp. 563–583, 1978.

[4] D. Oloumi, "Ultra-wideband synthetic aperture radar imaging : Theory and applications," PhD thesis, Unversity of Alberta, 2016.

[5] Y. Wang and A. E. Fathy, "Advanced system level simulation platform for three-dimensional uwb through-wall imaging sar using time-domain approach," *IEEE Trans. Geosci. Remote Sens.*, vol. 50, no. 5, pp. 1986–2000, May 2012.

[6] L. Sakkila, A. Rivenq, C. Tatkeu, Y. El Hillali, J.-P. Ghys, and J.-M. Rouvaen, "Methods of target recognition for uwb radar," in *2010 IEEE Intelligent Vehicles Symposium*, IEEE, 2010, pp. 949–954.

[7] M. I. Skolnik, "Introduction to radar systems," *New York*, 1980.

[8] W. Shao, A. Edalati, T. R. McCollough, and W. J. McCollough, "A time-domain measurement system for uwb microwave imaging," *IEEE Transactions on Microwave Theory and Techniques*, vol. 66, no. 5, pp. 2265–2275, 2018.

[9] Z. Li, J. Wang, and Q. H. Liu, "Frequency-domain backprojection algorithm for synthetic aperture radar imaging," *IEEE Geoscience and Remote Sensing Letters*, vol. 12, no. 4, pp. 905–909, 2015.

[10] D. Oloumi, P. Boulanger, A. Kordzadeh, and K. Rambabu, "Breast tumor detection using uwb circular-sar tomographic microwave imaging," in *Proc. 37th Annu. Int. Conf. IEEE Eng. Med. Biol. Soc. (EMBC)*, Aug. 2015, pp. 7063–7066.

[11] D. Oloumi, K. K. Chan, P. Boulanger, and K. Rambabu, "SADG Process Monitoring in Heavy Oil Reservoir Using UWB Radar Techniques," *IEEE Trans. Microw. Theory Techn.*, vol. 64, no. 6, pp. 1884–1895, Jun. 2016.

[12] S. Gogineni, J. B. Yan, D. Gomez, F. Rodriguez-Morales, J. Paden, and C. Leuschen, "Ultra-wideband radars for remote sensing of snow and ice," in *IEEE MTT-S Int. Microw. RF Conf.*, Dec. 2013, pp. 1–4.

[13] Y. Gao, M. T. Al Qaseer, and R. Zoughi, "Complex permittivity extraction from synthetic aperture radar (sar) images," *IEEE Transactions on Instrumentation and Measurement*, 2019.

[14] B. Wu, Y. Gao, J. Laviada, M. T. Ghasr, and R. Zoughi, "Time-reversal sar imaging for nondestructive testing of circular and cylindrical multilayered dielectric structures," *IEEE Transactions on Instrumentation and Measurement*, vol. 69, no. 5, pp. 2057–2066, 2020.

[15] C. Liu, M. T. A. Qaseer, and R. Zoughi, "Influence of antenna pattern on synthetic aperture radar resolution for nde applications," *IEEE Transactions on Instrumentation and Measurement*, vol. 70, pp. 1–11, 2021.

[16] S. Wu, T. Sakamoto, K. Oishi, T. Sato, K. Inoue, T. Fukuda, K. Mizutani, and H. Sakai, "Person-specific heart rate estimation with ultra-wideband radar using convolutional neural networks," *IEEE Access*, vol. 7, pp. 168 484–168 494, 2019.

[17] T. M. Grzegorczyk, P. M. Meaney, P. A. Kaufman, R. M. diFlorio-Alexander, and K. D. Paulsen, "Fast 3-d tomographic microwave imaging for breast cancer detection," *IEEE Trans. Med. Imag.*, vol. 31, no. 8, pp. 1584–1592, Aug. 2012.

[18] D. Oloumi, K. Rambabu, and P. Boulanger, "Tracking a biopsy needle inside a breast using uwb circular-sar," in *2015 IEEE Int. Symp. on Antennas Propag. USNC/URSI Nat. Radio Sci. Meeting*, Jul. 2015, pp. 534–535.

[19] J. C. Adams, W. Gregorwich, L. Capots, and D. Liccardo, "Ultra-wideband for navigation and communications," in *2001 IEEE Aero. Conf. Proc. (Cat. No.01TH8542)*, vol. 2, Mar. 2001, 2/785–2/792 vol.2.

[20] S. Lim, S. Lee, J. Jung, and S. Kim, "Detection and localization of people inside vehicle using impulse radio ultra-wideband radar sensor," *IEEE Sensors Journal*, vol. 20, no. 7, pp. 3892–3901, 2020.

[21] D. Kocur, J. Fortes, and M. Švecová, "Multiple moving person tracking by uwb sensors: The effect of mutual shielding persons and methods reducing its impacts," *EURASIP J. Wireless Commun. Netw.*, vol. 2017, no. 1, p. 68, Apr. 2017.

[22] W. B. Muller, "Semi-automatic determination of layer depth, permittivity and moisture content for unbound granular pavements using multi-offset 3-d gpr," *International Journal of Pavement Engineering*, vol. 21, no. 10, pp. 1281–1296, 2020.

[23] A. S. M. Alqadami, K. S. Bialkowski, A. T. Mobashsher, and A. M. Abbosh, "Wearable electromagnetic head imaging system using flexible wideband antenna array based on polymer technology for brain stroke diagnosis," *IEEE Transactions on Biomedical Circuits and Systems*, vol. 13, no. 1, pp. 124–134, 2019.

[24] D. Oloumi, R. S. C. Winter, A. Kordzadeh, P. Boulanger, and K. Rambabu, "Microwave imaging of breast tumor using time-domain UWB circular-sar technique," *IEEE Transactions on Medical Imaging*, vol. 39, no. 4, pp. 934–943, 2020.

[25] D. Ireland, K. Bialkowski, and A. Abbosh, "Microwave imaging for brain stroke detection using born iterative method," *IET Microwaves, Antennas & Propagation*, vol. 7, no. 11, pp. 909–915, 2013.

[26] W. Ameer, D. Awan, S. Bashir, and A. Waheed, "Use of directional uwb antenna for lung tumour detection," in *2019 2nd International Conference on Advancements in Computational Sciences (ICACS)*, 2019, pp. 1–5.

[27] F. M. Sabzevari, A. E.-C. Tan, and K. Rambabu, "Real-time permittivity extraction based on ultra-wideband impulse radar and genetic algorithm for tunnel construction operations," *IEEE Sensors Journal*, pp. 1–1, 2023.

[28] R. Cicchetti, E. Miozzi, O. Testa, *et al.*, "Wideband and uwb antennas for wireless applications: A comprehensive review," *International Journal of Antennas and Propagation*, vol. 2017, 2017.

[29] A. Bhattacharjee, A. Bhawal, A. Karmakar, A. Saha, and D. Bhattacharya, "Vivaldi antennas: A historical review and current state of art," *International Journal of Microwave and Wireless Technologies*, vol. 13, no. 8, pp. 833–850, 2021.

[30] R. Feghhi, D. Oloumi, and K. Rambabu, "Tunable subnanosecond gaussian pulse radar transmitter: Theory and analysis," *IEEE Transactions on Microwave Theory and Techniques*, vol. 68, no. 9, pp. 3823–3833, 2020.

[31] M. G. Amin and F. Ahmad, "Through-the-wall radar imaging: Theory and applications," in *Academic Press Library in Signal Processing*, vol. 2, Elsevier, 2014, pp. 857–909.

[32] L. Li, A. E.-C. Tan, K. Jhamb, and K. Rambabu, "Buried object characterization using ultra-wideband ground penetrating radar," *IEEE Transactions on Microwave Theory and Techniques*, vol. 60, no. 8, pp. 2654–2664, 2012.

[33] K. S. Sultan, B. Mohammed, M. Manoufali, and A. M. Abbosh, "Portable electromagnetic knee imaging system," *IEEE Transactions on Antennas and Propagation*, vol. 69, no. 10, pp. 6824–6837, 2021.

[34] Y.-Y. Chen, S.-P. Huang, T.-W. Wu, W.-T. Tsai, C.-Y. Liou, and S.-G. Mao, "Uwb system for indoor positioning and tracking with arbitrary target orientation, optimal anchor location, and adaptive nlos mitigation," *IEEE Transactions on Vehicular Technology*, vol. 69, no. 9, pp. 9304–9314, 2020.

[35] C. Waldschmidt, J. Hasch, and W. Menzel, "Automotive radar — from first efforts to future systems," *IEEE Journal of Microwaves*, vol. 1, no. 1, pp. 135–148, 2021.

[36] C. Oliver and S. Quegan, *Understanding synthetic aperture radar images*. SciTech Publishing, 2004.

[37] C. Özdemir, Ş. Demirci, E. Yiğit, and B. Yilmaz, "A review on migration methods in b-scan ground penetrating radar imaging," *Mathematical Problems in Engineering*, vol. 2014, 2014.

[38] J. M. Lopez-Sanchez and J. Fortuny-Guasch, "3-d radar imaging using range migration techniques," *IEEE Transactions on antennas and propagation*, vol. 48, no. 5, pp. 728–737, 2000.

[39] T. Sakamoto, T. Sato, P. J. Aubry, and A. G. Yarovoy, "Ultra-wideband radar imaging using a hybrid of kirchhoff migration and stolt fk migration with an inverse boundary scattering transform," *IEEE Transactions on Antennas and Propagation*, vol. 63, no. 8, pp. 3502–3512, 2015.

[40] ——, "Ultra-wideband radar imaging using a hybrid of kirchhoff migration and stolt f-k migration with an inverse boundary scattering transform," *IEEE Transactions on Antennas and Propagation*, vol. 63, no. 8, pp. 3502–3512, 2015.

[41] X. Zhuge, T. Savelyev, A. Yarovoy, L. Ligthart, and B. Levitas, "Comparison of different migration techniques for uwb short-range imaging," in *2009 European Radar Conference (EuRAD)*, 2009, pp. 184–187.

[42] E. Yigit, S. Demirci, C. Özdemir, and M. Tekbaş, "Short-range ground-based synthetic aperture radar imaging: Performance comparison between frequency-wavenumber migration and back-projection algorithms,"

Journal of Applied Remote Sensing, vol. 7, no. 1, pp. 073 483–073 483, 2013.

[43] F. M. Sabzevari, R. S. C. Winter, D. Oloumi, and K. Rambabu, "A microwave sensing and imaging method for multiphase flow metering of crude oil pipes," *IEEE Journal of Selected Topics in Applied Earth Observations and Remote Sensing*, vol. 13, pp. 1286–1297, 2020.

[44] E. N. dos Santos, R. L. de Paiva Rodrigues, D. R. Pipa, R. E. M. Morales, and M. J. da Silva, "Three-dimensional bubble shape estimation in two-phase gas-liquid slug flow," *IEEE Sensors Journal*, vol. 18, no. 3, pp. 1122–1130, 2017.

[45] Q. Su, C. Tan, and F. Dong, "Measurement of oil–water two-phase flow phase fraction with ultrasound attenuation," *IEEE Sensors J.*, vol. 18, no. 3, pp. 1150–1159, Feb. 2018.

[46] F. R. M. da Mota, D. J. Pagano, and M. E. Stasiak, "Water volume fraction estimation in two-phase flow based on electrical capacitance tomometry," *IEEE Sensors J.*, vol. 18, no. 16, pp. 6822–6835, Aug. 2018.

[47] G. Falcone, G. Hewitt, and C. Alimonti, *Multiphase Flow Metering: Principles and Applications*, ser. Developments in Petroleum Science. Elsevier Science, 2009.

[48] Z. Wu, "Developing a microwave tomographic system for multiphase flow imaging: Advances and challenges," *Trans. Inst. Meas. Control*, vol. 37, no. 6, pp. 760–768, 2015.

[49] F. R. M. da Mota, D. J. Pagano, and M. E. Stasiak, "Water volume fraction estimation in two-phase flow based on electrical capacitance tomometry," *IEEE Sensors J.*, vol. 18, no. 16, pp. 6822–6835, 2018.

[50] M. Tayyab, M. S. Sharawi, and A. Al-Sarkhi, "A radio frequency sensor array for dielectric constant estimation of multiphase oil flow in pipelines," *IEEE Sensors J.*, vol. 17, no. 18, pp. 5900–5907, Sep. 2017.

[51] H. E. de Lima Ávila, D. J. Pagano, and F. R. de Sousa, "Water fraction measurement using a rf resonant cavity sensor," in *Proc. 19th Symp. IMEKO TC Symp., 17th IWADC Workshop Adv. Instrum. Sensors Interoperability*, 2013, pp. 281–285.

[52] H. E. de Lima Avila, D. J. Pagano, and F. R. de Sousa, "Improving the performance of an rf resonant cavity water-cut meter using an impedance matching network," *Flow Meas. Instrum.*, vol. 43, pp. 14–22, 2015.

[53] B. K. Arvoh, R. Hoffmann, and M. Halstensen, "Estimation of volume fractions and flow regime identification in multiphase flow based on gamma measurements and multivariate calibration," *Flow Measurement and Instrumentation*, vol. 23, no. 1, pp. 56–65, 2012.

[54] V. R. Bom, M. C. Clarijs, C. W. van Eijk, Z. I. Kolar, J. Frieling, L. Scheers, and G. J. Miller, "Accuracy aspects in multiphase flow metering using x-ray transmission," *IEEE Trans. Nucl. Sci.*, vol. 48, no. 6, pp. 2335–2339, 2001.

[55] P. Mehdizadeh, D. Farchy, J. Suarez, *et al.*, "Multiphase meter production well testing applied to low-gor mature fields," in *SPE Production and Operations Symp.*, Society of Petroleum Engineers, 2009.

[56] I. M. Saied, M. Meribout, E. Kato, and X. H. Zhao, "Terahertz spectroscopy for measuring multiphase fractions," *IEEE Trans. THz Sci. Technol.*, vol. 7, no. 3, pp. 250–259, May 2017.

[57] Yi Li and W. Yang, "Measurement of multi-phase distribution using an integrated dual-modality sensor," in *2009 IEEE Int. Workshop Imag. Syst. Techn.*, May 2009, pp. 335–339.

[58] S. R. Wylie, A. Shaw, and A. I. Al-Shamma'a, "RF sensor for multiphase flow measurement through an oil pipeline," *Meas. Sci. Tech.*, vol. 17, no. 8, pp. 2141–2149, Jul. 2006.

[59] Q. Wang, H. Wang, K. Hao, and P. Dai, "Two-phase flow regime identification based on cross-entropy and information extension methods for computerized tomography," *IEEE Trans. Instrum. Meas.*, vol. 60, no. 2, pp. 488–495, Feb. 2011.

[60] V. R. Bom, M. C. Clarijs, C. W. E. van Eijk, Z. I. Kolar, J. Frieling, L. A. Scheers, and G. J. Miller, "Accuracy aspects in multiphase flow metering using x-ray transmission," *IEEE Trans. Nucl. Sci.*, vol. 48, no. 6, pp. 2335–2339, Dec. 2001.

[61] D. Kouame, J.-M. Girault, and F. Patat, "High resolution processing techniques for ultrasound doppler velocimetry in the presence of colored noise. i. nonstationary methods," *IEEE transactions on ultrasonics, ferroelectrics, and frequency control*, vol. 50, no. 3, pp. 257–266, 2003.

[62] Omnexus, *Dielectric constant values of several plastics*, *https://passive-components.eu/what-is-dielectric-constant-of-plastic-materials/*, accessed 26.06.2019.

[63] C. T. Crowe, *Multiphase flow handbook*. CRC press, 2005, vol. 59.

[64] B. Sun, *Multiphase Flow in Oil and Gas Well Drilling*. John Wiley & Sons, 2016.

[65] R. Thorn, G. A. Johansen, and B. T. Hjertaker, "Three-phase flow measurement in the petroleum industry," *Measurement Science and Technology*, vol. 24, no. 1, p. 012 003, 2012.

[66] M. d. M. F. Figueiredo, F. d. C. T. Carvalho, A. M. F. Fileti, and A. L. Serpa, "Dispersed-phase velocities for gas-liquid vertical slug and dispersed-bubbles flows using an ultrasonic cross-correlation technique," *Flow Measurement and Instrumentation*, vol. 79, p. 101 949, 2021.

[67] L. Li, A. E. Tan, K. Jhamb, and K. Rambabu, "Characteristics of ultra-wideband pulse scattered from metal planar objects," *IEEE Trans. Antennas Propag.*, vol. 61, no. 6, pp. 3197–3206, Jun. 2013.

[68] D. Oloumi, J. Ting, and K. Rambabu, "Design of pulse characteristics for near-field uwb-sar imaging," *IEEE Trans. Microw. Theory Techn.*, vol. 64, no. 8, pp. 2684–2693, Aug. 2016.

[69] P. R. Foster, J. D. Halsey, and M. G. M. Hussain, "Introduction to ultra-wideband radar systems," in *Ultra-Wideband Antenna Tech.*, 1995.

[70] D. Oloumi, M. I. Pettersson, P. Mousavi, and K. Rambabu, "Imaging of oil-well perforations using uwb synthetic aperture radar," *IEEE Transactions on Geoscience and Remote Sensing*, vol. 53, no. 8, pp. 4510–4520, Aug. 2015.

[71] H. Ahmed, "Capacitance sensors for void-fraction measurements and flow-pattern identification in air–oil two-phase flow," *IEEE Sensors J.*, vol. 6, no. 5, pp. 1153–1163, Oct. 2006.

[72] S. A. Sulaiman and N. A. Z. Kamarudin, "Bubbles size estimation in liquid flow through a vertical pipe," *J. Appl. Sci.*, vol. 12, pp. 2464–2468, 2012.

[73] P. Trifunović, "Use of composite materials in oil industry," *Podzemni radovi*, no. 19, pp. 157–164, 2011.

[74] V. Sokolov, S. Shalgunov, I. Gurtovnik, L. Mikheeva, and I. Simonov-Emel'yanov, "Dielectric characteristics of glass fibre reinforced plastics and their components," *Int. Polym. Sci. Tech.*, vol. 32, no. 7, pp. 62–67, 2005.

[75] P. Bao, L. Zhang, and X. Wu, "Canny edge detection enhancement by scale multiplication," *IEEE Trans. Pattern Anal. Mach. Intell.*, vol. 27, no. 9, pp. 1485–1490, Sep. 2005.

[76] Y. Zheng, J. Rao, and L. Wu, "Edge detection methods in digital image processing," in *2010 5th Int. Conf. on Computer Science Education*, Aug. 2010, pp. 471–473.

[77] M. Başţan, S. S. Bukhari, and T. Breuel, "Active canny: Edge detection and recovery with open active contour models," *IET Image Process.*, vol. 11, no. 12, pp. 1325–1332, 2017.

[78] S. Jin, W. Kim, and J. Jeong, "Fine directional de-interlacing algorithm using modified sobel operation," *IEEE Transactions on Consumer Electronics*, vol. 54, no. 2, pp. 587–862, May 2008.

[79] G. N. Chaple, R. D. Daruwala, and M. S. Gofane, "Comparisions of robert, prewitt, sobel operator based edge detection methods for real time uses on fpga," in *2015 International Conference on Technologies for Sustainable Development (ICTSD)*, Feb. 2015, pp. 1–4.

[80] M. B. Ahmad and Tae-Sun Choi, "Local threshold and boolean function based edge detection," *IEEE Trans. Consum. Electron.*, vol. 45, no. 3, pp. 674–679, Aug. 1999.

[81] J. Ting, D. Oloumi, and K. Rambabu, "Fmcw sar system for near-distance imaging applications—practical considerations and calibrations," *IEEE Trans. Microw. Theory Techn.*, vol. 66, no. 1, pp. 450–461, Jan. 2018.

[82] Q. Dou, L. Wei, D. R. Magee, and A. G. Cohn, "Real-time hyperbola recognition and fitting in gpr data," *IEEE Trans. Geosci. Remote Sens.*, vol. 55, no. 1, pp. 51–62, Jan. 2017.

[83] M. H. Fazalul Rahiman, R. Abdul Rahim, M. H. Fazalul Rahiman, and M. Tajjudin, "Ultrasonic transmission-mode tomography imaging for liquid/gas two-phase flow," *IEEE Sensors J.*, vol. 6, no. 6, pp. 1706–1715, Dec. 2006.

[84] N. Ahmadian, S. Hasan, and O. P. N. Calla, "Permittivity and backscattering coefficient of diesel oil-contaminated soil at c band (5.3 ghz)," *Int. J. of Microw. Sci. Tech.*, vol. 2013, 2013.

[85] D. N. Chapman, N. Metje, and A. Stark, *Introduction to tunnel construction*. CRC Press, 2017.

[86] C. Laughton, "Geotechnical problems encountered by tunnel boring machines mining in sedimentary rocks," *Water and Energy Abstracts*, vol. 15, no. 4, 2005.

[87] S. Zhao and I. L. Al-Qadi, "Super-resolution of 3-d gpr signals to estimate thin asphalt overlay thickness using the xcmp method," *IEEE Transactions on Geoscience and Remote sensing*, vol. 57, no. 2, pp. 893–901, 2018.

[88] S. Busch, J. Van der Kruk, and H. Vereecken, "Improved characterization of fine-texture soils using on-ground gpr full-waveform inversion,"

IEEE Transactions on Geoscience and Remote Sensing, vol. 52, no. 7, pp. 3947–3958, 2013.

[89] X. H. Tao, J. Q. Huang, and Y. C. Cai, "Inverse analysis for inhomogeneous dielectric coefficient of pavement material based on genetic algorithm," in *Applied Mechanics and Materials*, Trans Tech Publ, vol. 438, 2013, pp. 430–435.

[90] W. B. Muller, "Semi-automatic determination of layer depth, permittivity and moisture content for unbound granular pavements using multi-offset 3-d gpr," *International Journal of Pavement Engineering*, pp. 1–16, 2018.

[91] S. M. Aguilar, J. D. Shea, M. A. Al-Joumayly, B. D. Van Veen, N. Behdad, and S. C. Hagness, "Dielectric characterization of pcl-based thermoplastic materials for microwave diagnostic and therapeutic applications," *IEEE transactions on biomedical engineering*, vol. 59, no. 3, pp. 627–633, 2011.

[92] M. Sadeghi, M. M. Tajdini, E. Wig, and C. M. Rappaport, "Single frequency fast dielectric characterization of concealed body-worn explosive threats," *IEEE Transactions on Antennas and Propagation*, 2020.

[93] M. H. Hosseini, H. Heidar, and M. H. Shams, "Nondestructive em characterization of two-layer absorbers using coupled coaxial probes," *IEEE Transactions on Electromagnetic Compatibility*, 2019.

[94] F. Zhou, Z. Chen, H. Liu, J. Cui, B. F. Spencer, and G. Fang, "Simultaneous estimation of rebar diameter and cover thickness by a gpr-emi dual sensor," *Sensors*, vol. 18, no. 9, p. 2969, 2018.

[95] L. Bronckers and A. Smolders, "Broadband material characterization method using a cpw with a novel calibration technique," *IEEE Antennas and Wireless Propagation Letters*, vol. 15, pp. 1763–1766, 2016.

[96] S. Lambot, E. C. Slob, I. van den Bosch, B. Stockbroeckx, and M. Vanclooster, "Modeling of ground-penetrating radar for accurate characterization of subsurface electric properties," *IEEE transactions on geoscience and remote sensing*, vol. 42, no. 11, pp. 2555–2568, 2004.

[97] G. T. Herman, "Image reconstruction from projections," *The fundamental of computerized tomography*, pp. 260–276, 1980.

[98] J. Justice and A. Vassiliou, "Diffraction tomography for geophysical monitoring of hydrocarbon reservoirs," *Proceedings of the IEEE*, vol. 78, no. 4, pp. 711–722, 1990.

[99] T. Takayama and M. Sato, "A novel direction-finding algorithm for directional borehole radar," *IEEE Trans. Geosci. Remote Sens.*, vol. 45, no. 8, pp. 2520–2528, 2007.

[100] U. Spagnolini, "Permittivity measurements of multilayered media with monostatic pulse radar," *IEEE Trans. Geosci. Remote Sens.*, vol. 35, no. 2, pp. 454–463, 1997.

[101] C. Chen, J. Johnson, M. Sato, and A. Yarovoy, "Special issue on subsurface sensing using ground-penetrating radar," *IEEE Trans. Geosci. Remote Sens*, vol. 45, no. 8, pp. 2419–2421, 2007.

[102] R. Wu, X. Li, and J. Li, "Continuous pavement profiling with ground-penetrating radar," *IEE Proceedings-Radar, Sonar and Navigation*, vol. 149, no. 4, pp. 183–193, 2002.

[103] S. Lambot, E. C. Slob, I. van den Bosch, B. Stockbroeckx, and M. Vanclooster, "Modeling of ground-penetrating radar for accurate characterization of subsurface electric properties," *IEEE Transactions on Geoscience and Remote Sensing*, vol. 42, no. 11, pp. 2555–2568, 2004.

[104] J. D. Taylor, "Ultra-wideband radar overview," in *Introduction to ultra-wideband radar systems*, 1, CRC Press, 1995.

[105] D. Oloumi, M. I. Pettersson, P. Mousavi, and K. Rambabu, "Imaging of oil-well perforations using UWB synthetic aperture radar," *IEEE Trans. Geosci. Remote Sens.*, vol. 53, no. 8, pp. 4510–4520, 2015.

[106] D. Oloumi and K. Rambabu, "Metal-cased oil well inspection using near-field UWB radar imaging," *IEEE Trans. Geosci. Remote Sens.*, vol. 56, no. 10, pp. 5884–5892, 2018.

[107] R. S. Winter, D. Oloumi, and K. Rambabu, "Virtually developed synthetic aperture radar: Theory, simulation, and measurements," *IEEE Trans. Geosci. Remote Sens.*, vol. 57, no. 5, pp. 2855–2863, 2018.

[108] L. Li, A. E.-C. Tan, K. Jhamb, and K. Rambabu, "Buried object characterization using ultra-wideband ground penetrating radar," *IEEE Trans. Microw. Theory Techn.*, vol. 60, no. 8, pp. 2654–2664, 2012.

[109] A. Tan and M. Chia, "Measuring human body impulse response using UWB radar," *Electron. Lett.*, vol. 41, no. 21, pp. 1193–1194, 2005.

[110] S. Ramo, J. R. Whinnery, and T. Van Duzer, *Fields and waves in communication electronics*. John Wiley & Sons, 1994.

[111] W. I. Linlor and G. R. Jiracek, "Electromagnetic reflection from multilayered snow models," *J. of Glaciology*, vol. 14, no. 72, pp. 501–515, 1975.

[112] S. Lambot, E. Slob, I. Van Den Bosch, B. Stockbroeckx, B. Scheers, and M. Vanclooster, "Estimating soil electric properties from monostatic ground-penetrating radar signal inversion in the frequency domain," *Water Resources Research*, vol. 40, no. 4, 2004.

[113] CST AG, *CST Microwave Studio Suite, Electromagnetic Field Simulation Software, Version 2018*, Darmstadt, Germany, 2018.

[114] E. Hammerstad and O. Jensen, "Accurate models for microstrip computer-aided design," in *1980 IEEE MTT-S International Microwave Symposium Digest*, IEEE, 1980, pp. 407–409.

[115] T. Gruner and D.-G. Welsch, "Green-function approach to the radiation-field quantization for homogeneous and inhomogeneous kramers-kronig dielectrics," *Physical Review A*, vol. 53, no. 3, p. 1818, 1996.

[116] *Sanitary sewer*, *https://en.wikipedia.org/wiki/Sanitary sewer/*, accessed 03.12.2019.

[117] L. Erdogan, C. Akyel, and F. M. Ghannouchi, "Dielectric properties of oil sands at 2.45 GHz with $TE1,0,11$ mode determined by a rectangular cavity resonator," *Journal of Microwave Power and Electromagnetic Energy*, vol. 45, no. 1, pp. 15–23, 2011.

[118] G. Brodie, R. Destefani, P. A. Schneider, L. Airey, and M. V. Jacob, "Dielectric properties of sewage biosolids: Measurement and modeling," *Journal of Microwave Power and Electromagnetic Energy*, vol. 48, no. 3, pp. 147–157, 2014.

[119] T. Meissner and F. J. Wentz, "The complex dielectric constant of pure and sea water from microwave satellite observations," *IEEE Trans. Geosci. Remote Sens.*, vol. 42, no. 9, pp. 1836–1849, 2004.

[120] T. Zwick, J. Haala, and W. Wiesbeck, "A genetic algorithm for the evaluation of material parameters of compound multilayered structures," *IEEE Trans. Microw. Theory Techn.*, vol. 50, no. 4, pp. 1180–1187, 2002.

[121] W. E. Pace, W. B. Westphal, and S. A. Goldblith, "Dielectric properties of commercial cooking oils," *J. of Food Sci.*, vol. 33, no. 1, pp. 30–36, 1968.

[122] M. A. Sairin, N. N. A. Nizar, S. A. Aziz, and F. Z. Rokhani, "Study of dielectric permittivity and fatty acid composition for fats and oil in wide frequency spectroscopy measurement at 0.5–50 GHz," in *2016 10th Int. Conf. on Sens. Tech. (ICST)*, IEEE, 2016, pp. 1–5.

[123] E. ToolBox, *Dielectric constants of liquids*, *Available at: https://www. engineeringtoolbox.com/ liquid-dielectric-constants-d*1263.*html*, *accessed* 05.12.2019.

[124] Q. Lu, J. Pu, and Z. Liu, "Feature extraction and automatic material classification of underground objects from ground penetrating radar data," *Journal of Electrical and Computer Engineering*, vol. 2014, 2014.

[125] N. Kim, S. Kim, Y.-K. An, and J.-J. Lee, "Triplanar imaging of 3-d gpr data for deep-learning-based underground object detection," *IEEE Journal of Selected Topics in Applied Earth Observations and Remote Sensing*, vol. 12, no. 11, pp. 4446–4456, 2019.

[126] A. G. Mullissa, C. Persello, and A. Stein, "Polsarnet: A deep fully convolutional network for polarimetric sar image classification," *IEEE Journal of selected topics in applied earth observations and remote sensing*, vol. 12, no. 12, pp. 5300–5309, 2019.

[127] C. Warren, A. Giannopoulos, and I. Giannakis, "Gprmax: Open source software to simulate electromagnetic wave propagation for ground penetrating radar," *Computer Physics Communications*, vol. 209, pp. 163–170, 2016.

[128] M.-T. Pham and S. Lefèvre, "Buried object detection from b-scan ground penetrating radar data using faster-rcnn," in *IGARSS 2018-2018 IEEE International Geoscience and Remote Sensing Symposium*, IEEE, 2018, pp. 6804–6807.

[129] X. Yang, W. Yan, W. Ni, X. Pu, H. Zhang, and M. Zhang, "Object-guided remote sensing image scene classification based on joint use of deep-learning classifier and detector," *IEEE Journal of Selected Topics in Applied Earth Observations and Remote Sensing*, vol. 13, pp. 2673–2684, 2020.

[130] Y. Yue, T. Jiang, J. Wang, Y. Chao, Q. Zhou, J. Zheng, and X. Wang, "The theory and application of the random dislocation directional seismic wave technique in a tunnel environment," *Journal of Geophysics and Engineering*, vol. 16, no. 5, pp. 939–949, Aug. 2019.

[131] R. M. Mersereau and A. V. Oppenheim, "Digital reconstruction of multidimensional signals from their projections," *Proceedings of the IEEE*, vol. 62, no. 10, pp. 1319–1338, 1974.

[132] Y.-J. Park, S.-B. Cho, K.-H. Kim, and D.-G. Youn, "Development of an ultra wideband ground penetrating radar (uwb gpr) for nondestructive testing of underground objects," in *IEEE Antennas and Propagation Society Symposium, 2004.*, IEEE, vol. 2, 2004, pp. 1279–1282.

[133] T. Counts, A. C. Gurbuz, W. R. Scott, J. H. McClellan, and K. Kim, "Multistatic ground-penetrating radar experiments," *IEEE transactions on geoscience and remote sensing*, vol. 45, no. 8, pp. 2544–2553, 2007.

[134] M. A. Mooney, B. Walter, and C. Frenzel, "Real-time tunnel boring machine monitoring: A state of the art review," *North American Tunnelling, 2012 proceedings*, pp. 73–81, 2012.

[135] X. Wang, S. Sun, J. Wang, A. Yarovoy, B. Neducza, and G. Manacorda, "Real gpr signal processing for target recognition with circular array antennas," in *2016 URSI International Symposium on Electromagnetic Theory (EMTS)*, IEEE, 2016, pp. 818–821.

[136] L. Wei, D. R. Magee, and A. G. Cohn, "An anomalous event detection and tracking method for a tunnel look-ahead ground prediction system," *Automation in Construction*, vol. 91, pp. 216–225, 2018.

[137] S.-L. Shen, Q.-L. Cui, C.-E. Ho, and Y.-S. Xu, "Ground response to multiple parallel microtunneling operations in cemented silty clay and sand," *Journal of Geotechnical and Geoenvironmental Engineering*, vol. 142, no. 5, p. 04 016 001, 2016.

[138] A. R. Von Hippel, *Dielectric materials and applications: papers by 22 contributors*. Technology Press of MIT and Wiley, 1954.

[139] S. Dubnewych, S. Klein, and P. Guptill, "Geotechnical and design challenges for tbm selection on the ice tunnel," *North American Tunneling 2010 Proceedings*, p. 147, 2010.

[140] H. Yang, H. He, and C. Chen, "Effect of cutterhead rotational speed on mudstone argillization during the tunneling process," *Bulletin of Engineering Geology and the Environment*, vol. 82, no. 2, p. 45, 2023.

[141] A. Karimov, R. Feghhi, F. M. Sabzevari, R. S. C. Winter, R. Fedosejevs, and K. Rambabu, "Design and development of a high-power pulse transmitter for underground environmental perception," *IEEE Transactions on Microwave Theory and Techniques*, vol. 70, no. 5, pp. 2891–2903, 2022.

[142] Y. Yue, Y. Liu, Y. Ye, Y. Wo, and Z. Qian, "Least-squares kirchhoff depth migration with fast point-spread-function computation," *IEEE Transactions on Geoscience and Remote Sensing*, vol. 61, pp. 1–10, 2023.

[143] Ö. Yilmaz, *Seismic data analysis: Processing, inversion, and interpretation of seismic data*. Society of exploration geophysicists, 2001.

[144] X. Zhuge, T. Savelyev, A. G. Yarovoy, and L. Ligthart, "Uwb array-based radar imaging using modified kirchhoff migration," in *2008 IEEE International Conference on Ultra-Wideband*, IEEE, vol. 3, 2008, pp. 175–178.

[145] R. S. C. Winter, D. Oloumi, and K. Rambabu, "Uwb sensor characterization for radar sensing and imaging in superluminal propagation regions," *IEEE Transactions on Microwave Theory and Techniques*, vol. 69, no. 1, pp. 297–307, 2021.

[146] S. Li, S. Wang, M. G. Amin, and G. Zhao, "Efficient near-field imaging using cylindrical mimo arrays," *IEEE Transactions on Aerospace and Electronic Systems*, vol. 57, no. 6, pp. 3648–3660, 2021.

[147] B. Liang, X. Shang, X. Zhuge, and J. Miao, "Accurate near-field millimeter-wave imaging of concave objects—a case study of dihedral structures under monostatic array configurations," *IEEE Transactions on Geoscience and Remote Sensing*, vol. 58, no. 5, pp. 3469–3483, 2020.

[148] A. M. Molaei, T. Fromenteze, V. Skouroliakou, T. V. Hoang, R. Kumar, V. Fusco, and O. Yurduseven, "Development of fast fourier-compatible image reconstruction for 3d near-field bistatic microwave imaging with dynamic metasurface antennas," *IEEE Transactions on Vehicular Technology*, vol. 71, no. 12, pp. 13 077–13 090, 2022.

[149] H. Hu, D. Zhu, and F. Hu, "A novel imaging method using fractional fourier transform for near-field synthetic aperture radiometer systems," *IEEE Geoscience and Remote Sensing Letters*, vol. 19, pp. 1–5, 2022.

[150] X. Zhuge, A. G. Yarovoy, T. Savelyev, and L. Ligthart, "Modified kirchhoff migration for uwb mimo array-based radar imaging," *IEEE Transactions on Geoscience and Remote Sensing*, vol. 48, no. 6, pp. 2692–2703, 2010.

[151] Z.-Y. Wang, Y. Guo, H. Yang, and Q. Qiu, "A heuristic explanation for the superluminal behaviors of evanescent waves," in *2012 Symposium on Photonics and Optoelectronics*, IEEE, 2012, pp. 1–4.

[152] D. Oloumi and K. Rambabu, "Studying the superluminal behavior of uwb antennas and its effect on near-field imaging," *IEEE Transactions on Antennas and Propagation*, vol. 64, no. 12, pp. 5084–5093, 2016.